The investigation of phonon lifetime and thermal transport mechanisms from Molecular Dynamics

Max Lau

MSc-R Physics

University of York
Physics
Condensed Matter Dynamics Group

Abstract

Phonon-phonon interactions give many materials extended properties that they otherwise would not have had without them. Phonons are quasiparticles of discrete, quantised vibrations. They are carriers of momentum, which makes them relevant to the transport of energy, particularly heat. For example, many thermoelectric and superconducting properties are due to electron-phonon and phonon-phonon scattering. Understanding these interactions requires complex theoretical frameworks, which are computationally expensive.

The aim of this thesis is to test Python-based tools for direct analysis of phonon lifetimes in a range of materials from Molecular Dynamics simulations, and to improve the efficiency by using Machine Learning (GAP) to accelerate the Molecular Dynamics to directly calculate phonon lifetimes.

In this thesis, current *ab initio* methods establish the theoretical framework behind the calculation of phonon lifetimes, which are traditionally performed through perturbative methods. New implemented methods for extracting phonon lifetimes and phonons at finite temperatures through Molecular Dynamics using several pre-existing methodologies have been used to extract phonon lifetimes. However, at high or low T they become disadvantageous and have been circumvented by combining some of these methodologies.

Through the combined use of Hybrid-MD and GAP, this thesis explores various methodologies and establishes a workflow for developing GAP potentials tailored for phonon calculations in MD. We also demonstrate that the GAP potential framework inherently misses crucial physics such as LO/TO splitting when applied to strongly ionic systems at finite T. Having extracted the phonon band structure at a range of finite T we have shown it is possible to get the lifetime.

Contents

List of Figures

List of Tables

List of Listings

Acknowledgements

I want to thank two of the best supervisors in the School of Physics, Engineering and Technology, Professor Matt Probert and Dr Phil Hasnip. It would not have been possible without the guidance and patience you have shown me. Despite not being an experienced programmer, I humbly acknowledge my failings. You both provided me with invaluable knowledge throughout my MSc-R. I want to give a big thanks to Scott for your advice on coding and programming. I would like to thank Rob for your helpful suggestions and help with CASTEP and Friday night Pub, and in general conversation, in which you all helped me settle into the group. I would like to thank Malcolm next door for Python suggestions, would like to thank Hossein for your help with TROM and developing the code needed for this work and additional post-processing tools. My thanks to Kit and Indigo for QFT notes and endless lecture notes, and good banter in the office.

As a final note, my faith in science has been somewhat lost by a previous institution, which, quite frankly, falls short of expectations, highlighting little care about teaching and research. Only recently that my faith been restored in science and its people, and it is refreshing to meet like-minded people for once who are willing to help and do science that actually matters. Therefore, I leave York knowing this is true.

It is thus fitting to submit this thesis in celebration and how far I have developed personally, having moved on from those awful times as a chemist.

Quote

A lecturer once told me, as an undergraduate, that life would be very boring if we were to describe all of chemistry through quantum mechanics. This is not true at all; in fact, it would mean I would never have to go through the torture that is experimental chemistry.

Declarations

I declare that this thesis is a presentation of original work and I am the sole author. This work has not previously been presented for a degree or other qualification at this University or elsewhere. All sources are acknowledged as references.

Signed Max Lau

Chapter 1

Introduction

1.1 First principles of Transport modelling

The vast majority of today's energy is lost as waste heat during the transformation of primary energy sources into usable power. In reality, most fuel-based engines are yet to be very efficient; even modern-day engines lose a large fraction of the energy they produce as waste heat during various transformation processes. Recent developments in Materials Science aim to capture this waste and convert it into useful energy, such as electricity generated from thermal gradients.

Most materials don't make good thermoelectrics because an effective thermoelectric material requires high Seebeck coefficient, high electrical conductivity, and low thermal conductivity which few materials possess all three ideal properties. For the application of thermoelectric materials, a useful metric is used to evaluate and compare the performance and efficiency of heat conversion, known as the thermoelectric figure of merit ZT which is a dimensionless value that tells us the ratio between the useful electrical power factor σ^2 and the thermal energy dissipated through heat conduction.

Most thermoelectric applications require a large figure of merit, ZT; however, the majority of materials have poor thermoelectric performance and therefore have limited conversion rates. One way to improve the conversion efficiency is to introduce pre-existing features in a material that enhance the conversion of thermal gradients into electrical power [4]. This can be achieved, for example, by doping a material with elements that modify its thermal or electrical conductivity. As a result, the development of energy-efficient materials has become a major focus in thermoelectric research.

The ZT of a material is calculated through different material properties

$$ZT = \frac{\sigma S^2 T}{\kappa_e + \kappa_L} \tag{1.1}$$

Here, the Temperature T, electric conductivity (σ), Seebeck coefficient (S) are defined as $S = -\frac{\Delta V}{\Delta T}$ where ΔV is the voltage difference and ΔT is the temperature difference. The electronic thermal conductivity κ_e and the lattice thermal conductivity κ_L. The total thermal conductivity is therefore composed of an electronic contribution, κ_e, and a lattice contribution, κ_L, which arises from lattice vibrations (phonons).

To achieve a high Seebeck coefficient S, an asymmetric Density of states (DOS) near the Fermi level E_F is required. It describes how electrons and holes flow from different temperature gradients, generating a potential energy difference.

The lattice thermal conductivity κ_L can be calculated by solving the Boltzmann Transport Equation (BTE) of particle-particle collisions. It is a quasi-classical description of transport phenomena that has an accurate level of theory for both the transport of charge carriers (electrons) and phonons. thermal lattice thermal conductivity is defined as κ_L

$$\kappa_L = \sum_{\nu,\mathbf{q}} C_\nu(\mathbf{q}) v^2_{\nu,x}(\mathbf{q}) \tau_\nu(\mathbf{q}), \tag{1.2}$$

where C_ν is the heat capacity and $v_{\nu,x}$ is the group velocity in the x direction $\tau_\nu(\mathbf{q})$ is the lifetime. The electronic thermal conductivity κ_e, defined as the heat current produced per unit of temperature gradient when the electrical current is zero, can be calculated via a set of transport coefficients from the Boltzmann transport equation [5] as

$$\kappa_\mathrm{e} = \kappa_0 - S^2 \sigma T \tag{1.3}$$

where κ_0 is the electronic thermal conductivity at zero electric field , S is the Seebeck coefficient and σ is the electrical conductivity.

In order to calculate thermal conductivity κ the lifetime $\tau_\nu(\mathbf{q})$ is needed which is calculated via the scattering matrix elements of the phonon-phonon scattering. In a fully interacting system, for a given number of phonon scattering lifetimes are summed up by Matthiessen's rule:

$$\frac{1}{\tau} = \sum_i \frac{1}{\tau_i} \tag{1.4}$$

This is summed up by electron-phonon and phonon-impurity scattering, phonon-phonon scattering lifetime. In this thesis, we look at the impact of the

phonon-phonon scattering process and its lifetime.

There are many methods for calculating thermal conductivity that have been developed over the years, for example:

(1) Perturbation theory via Boltzmann Transport Equation (ShengBTE)

(2) Non-equilibrium Molecular Dynamics (Müller-Plathe Method)

(3) Equilibrium Molecular Dynamics (Green-Kubo, Einstein Relation)

(4) Approach to Equilibrium Molecular Dynamics

These represent alternative methods for calculating the phonon scattering lifetime and, consequently, the thermal conductivity. Method 1 [5] relies on the Boltzmann Transport Equation (BTE) formalism, treating the phonon-phonon scattering lifetime perturbatively. Method 2 [6], known as the direct method, calculates the thermal conductivity directly from heat gradients imposed by creating boundary conditions consisting by separating the simulation box into 2N slabs. By swapping the lowest velocity (coolest) atom with the highest velocity (hottest) it creates a thermal gradient from which the lattice thermal conductivity κ can be calculated. This is the non-equilibrium molecular dynamics (NEMD) Müller-Plathe Method which is a direct method to calculate thermal conductivity along a specified direction. To maintain finite thermal motion, the Müller-Plathe NEMD method establishes a steady heat flux between a hot boundary at T_{hot} and a cold boundary at T_{cold} across a slab of material, allowing thermal conductivity to be calculated from a temperature gradient ∇T via Fourier's law of heat,

$$\boldsymbol{J} = -\lambda \nabla \tag{1.5}$$

Finally, methods 3 and 4 [7] also employ molecular dynamics, however in method 3 the fluctuation-dissipation theorem, based on linear-response theory, provides a link between the energy dissipated and the thermal fluctuations, where the thermal conductivity tensor κ is given by the Green-Kubo relation [8]: where $\mathbf{J}$ is the heat current. This is calculated through the autocorrelation of heat flux moving from one boundary to the other,

$$\kappa = \frac{V}{k_B T^2} \int_0^\infty \langle \mathbf{J}(0) \otimes \mathbf{J}(t) \rangle \, dt \tag{1.6}$$

Method 4 is the particular focus of this thesis. Both Mode Decomposition and Spectral Energy Density methods (SED) are used to calculate lifetimes τ from

equilibrium molecular dynamics (EMD) simulations. These methods have been shown to predict accurately the phonons in perfect bulk systems.

Both Green-Kubo and Non-Equilibrium Molecular Dynamics NEMD methods can predict the overall thermal conductivity successfully, however they only give limited insight to understanding the individual Phonon mode contributions.

From a computational cost perspective, both incorporation of MD and Green functions based methods scale as $\mathcal{O}(N^2)$ while using explicit DFT phonons with Boltzmann Transport Equation (BTE) of 4th order finite displacements are extremely costly to evaluate with scaling of $\mathcal{O}(N^3)$ or worse. The combination of AIMD and classical MD is very useful to calculate phonon lifetimes on larger systems without the hindrance of cost from doing finite-displacement phonons.

In this thesis, we also explore the use of two methods for calculating force constant matrix via the direct sampling method of MD trajectories by Kong and the best-fitted force constant matrix, originally developed by Maradudin[9][10]. By making use of symmetry, the force constants are directly fitted from MD trajectories.

An important contribution to lattice dynamics in this thesis is the phonon anharmonicity, which describes deviations from the ideal harmonicity. High temperature enhances anharmonic contribution leading to strong phonon–phonon scattering interaction which $T = 0$ FCM is no longer valid to capture suitable interactions between atoms.

Phonon anharmonicity strongly influences the phonon scattering lifetimes; in particular stronger anharmonic contributions lead to phonon-phonon scattering having shorter scattering rates which reduces the ability of phonons to transport heat as result of shorter mean free path of phonon-phonon scattering having shorter lifetime.

Third order lattice dynamics via perturbation theory are required to capture anharmonic contributions to Phonon modes as well as third and fourth order FCM to fully calculate lifetime for phonon scattering processes which are computationally expensive to compute for large bulk systems which are limited to relatively simple cases. Both SED and mode decomposition method considers anharmonic interactions.

The choice of lithium fluoride (LiF) to calculate the lifetime presents a challenge for molecular dynamics because it is extremely ionic in nature and requires a long range Coulomb term. Similarly LiF this is a particular challenge for machine learned interatomic potentials (MLIP) as these are short-ranged and often do not account for long-range electrostatics. Whilst some information about

long-range electrostatics is retained from learning DFT forces and energies, it lacks the proper long-range decay of $\frac{1}{r}$.

For non-DFT-based calculations, these long-range Coulombic effects must therefore be reintroduced, e.g. with Born effective charges supplemented from DFT based calculation being used for the non-analytical term of the dynamical matrix. Long-range interactions can also be added back using LAMMPS' Coulombic solver via an Ewald summation and used as an alternative, if proper care is taken to remove double counting of the long range Coulombic energy solver and residual GAP interactions. As no non-analytical term was developed in time for the submission of this thesis, the long-range effects are not included here.

The initial search for a suitable LiF potential begins with Gaussian approximation potential (GAP) training, providing a much-needed convergence test for the optimisation of our GAP model. The tests consist of independently changing the descriptor cutoff, number of sparse points and the order of the radial basis set expansion.

1.2 Thesis outline

Chapter 1 will outline the basis of this work, explaining why we care about quasiparticle interactions and their important role in developing thermoelectrics, as well as the key role they play in thermal transport.

Chapter 2 will introduce the fundamental framework on which all the density functional theory simulations work, as well as develop an understanding of how many-body interactions with phonons are needed to understand their fundamental behaviour in transport.

Chapter 3 The whys and don'ts of running simulations in CASTEP and how CASTEP works with different types of functionality, including how to train a GAP MLIP and the different approaches of data generation.

Chapter 4 The results of density functional theory simulations for PbTe and LiF, running LAMMPS Molecular dynamics simulations on LiF in and CASTEP to extract phonon dispersions from MD methods. It will also develop key principles needed to get phonons from molecular dynamics. This chapter motivates the theory section by explaining the choices and workflow for carrying out computational simulations with TROM, a code used for the phonon lifetime from MD.

Chapter 5 This section summarises potential directions for future work and

discusses the challenges encountered during this project, offering constructive insights on how to build upon the ideas developed throughout this thesis.

Chapter 2

Theory

2.1 Many-Body Problem

Properties of elements and subsequent materials are controlled by interactions of electrons and nuclei, the electrons from point point of view are orbitals which are in turn mathematical functions which combined create bonding. In order to understand the electronic structure of materials the use of quantum mechanics in theory and simulation is a necessity. Studying interacting electron systems consisting of electrons and nuclei for larger systems than a few atoms is very difficult despite knowing the exact equations for solving their behaviour.

For a system consisting of N_e electrons and N_N nuclei, we denote the electronic coordinates by $\mathbf{r}_1, \ldots, \mathbf{r}_{N_e}$ and the nuclear coordinates by $\mathbf{R}_1, \ldots, \mathbf{R}_{N_N}$. The many-body Schrödinger equation then reads

$$\hat{H}\Psi(\mathbf{R}_1, \ldots, \mathbf{R}_{N_N}, \mathbf{r}_1, \ldots, \mathbf{r}_{N_e}) = E\Psi(\mathbf{R}_1, \ldots, \mathbf{R}_{N_N}, \mathbf{r}_1, \ldots, \mathbf{r}_{N_e}). \tag{2.1}$$

where the full electronic structure Hamiltonian is written out as

$$\begin{aligned}\hat{H} = &\sum_{I=1}^{N_N} \frac{\vec{p}_I^{\,2}}{2M_I} + \sum_{i=1}^{N_e} \frac{\vec{p}_i^{\,2}}{2m} \\ &+ \frac{1}{4\pi\varepsilon_0}\left(\sum_{i>j} \frac{e^2}{|\vec{r}_i - \vec{r}_j|} + \sum_{I>J} \frac{Z_I Z_J e^2}{|\vec{R}_I - \vec{R}_J|} - \sum_{i,I} \frac{Z_I e^2}{|\vec{R}_I - \vec{r}_i|}\right) \\ &= T_N + T_e + V_{ee}(\vec{r}) + V_{NN}(\vec{R}) + V_{Ne}(\vec{r}, \vec{R}).\end{aligned} \tag{2.2}$$

Here T_N and T_e are the kinetic energies of the nuclei and electrons, and $V_{ee}(\vec{r}) + V_{NN}(\vec{R}) + V_{Ne}(\vec{r}, \vec{R})$ describe the electron-electron, nuclei-nuclei, and electron-nuclei potential terms. Both nuclei and electrons are treated quantum mechanically. Solving the exact Hamiltonian is formidable due to the exponential

scaling of the many-body wavefunction. For example, on a given grid, the computational cost scales as $\mathcal{O}\left(N_{\text{grid}}^{3N_{\text{nuc}}+3N_{\text{elec}}}\right)$. This exponential scaling rapidly makes solving this problem intractable.

2.2 The Born-Oppenheimer approximation

The electronic wavefunction is parametrically dependent on the position of the nuclei. We cannot separate the initial wavefunction into electron-dependent and nuclei-dependent wavefunctions to solve the electronic eigenstates of the electronic Hamiltonian without invoking a scheme to separate the two wavefunctions. here the total wavefunction of its electronic and nuclei parts.

$$\psi(\mathbf{R}_N, \mathbf{N}_e) \approx v(\mathbf{R}_N)_{nuc}\psi(\mathbf{N}_e)_{elec} \tag{2.3}$$

Further simplification is required to reduce the problem. Through the Born-Oppenheimer approximation[11], which decouples the nuclei from the electrons The mass of nuclei is far larger than that of electrons. When nuclei move, the electrons respond instantaneously around them to remain in the same ground state. The electrons can be approximated as moving in a potential energy surface created from the instantaneous positions of the nuclei. Under the BO approximation (2.3) is thus separable and holds.

$$\hat{H}_e = -\sum_i^N \frac{\nabla^2}{2} + \hat{V}_{ext} + \frac{1}{2}\sum_i^N \sum_{i\neq j} \frac{1}{|\mathbf{r}_i - \mathbf{r}_j|} \tag{2.4}$$

in atomic units, with the external potential being

$$\hat{V}_{ext} = -\sum_i^M \frac{Z_i}{|\mathbf{R}_N - \mathbf{r}_i|} \tag{2.5}$$

The Hamiltonian in Eq.(2.4) can be solved for any nuclear configuration to obtain the electron eigenvalue equation.

The Born Oppenheimer approximation (BO) is justified since the nuclei are sufficiently heavy that, to a good approximation, they can be treated as particles with fixed positions relative to the electrons. As a result, the nuclear motion can often be described by classical equations,full quantum-mechanical treatment of the nuclei is unnecessary.

The Born–Oppenheimer approximation is valid for most systems in which

nuclear displacements are small and electronic and nuclear motions remain well separated. However, in certain systems non-adiabatic effects become important: electronic and nuclear degrees of freedom are strongly coupled, and nuclear motion can induce electronic excitations. In such cases, the Born–Oppenheimer approximation breaks down and a fully quantum-mechanical treatment of both electrons and nuclei is required.

2.3 Density Functional Theory

Density functional theory is used in almost every area of chemistry and physics due to its ability to perform calculations with many hundreds of atoms. In Density Functional Theory (DFT) we do have single-electron wavefunctions, but we don't need a full, correlated many-electron wavefunction in an attempt to solve the rather complex many-body Hamiltonian. The advantage is that we only consider a set of N equations one for each electron with 3 spatial degrees of freedom each instead of 1 equation with 3N spatial degrees of freedom. [12]

The many-electron system can be described in terms of a single scalar quantity: the electron density $\rho(r)$, which gives the probability of finding an electron at position r irrespective of the positions of the other electrons. For a closed-shell system, the corresponding density operator is defined as

$$\hat{n}(\mathbf{r}) = \sum_{i=1}^{N_e} \delta(\mathbf{r} - \mathbf{r}_i). \tag{2.6}$$

$$n(\mathbf{r}_1) = \langle \Psi | \hat{n}(\mathbf{r}_1) | \Psi \rangle = \sum_{\sigma_1 \ldots \sigma_N} \int d^3 r_2 \ldots d^3 r_N \, |\Psi(\mathbf{r}_1 \sigma_1, \ldots, \mathbf{r}_N \sigma_N)|^2 \tag{2.7}$$

The Hohenberg-Kohn (H-K) paper establishes the following proofs of the density. [13] There exists an invertible one-to-one map C which maps the ground state external potential to the wavefunction

$$C : \mathscr{V} \to \psi \tag{2.8}$$

If ψ is the set of all possible ground states $|\Phi\rangle$, there is a map which projects onto each potential V corresponding ground state. Furthermore, there is a map D that maps all ground state densities from some element belonging to ψ

$$D : \psi \to n \tag{2.9}$$

for a given wavefunction ψ direct mapping to the set of particle densities where

the exact solution to the Schrödinger equation is known

$$CD : \mathscr{V} \rightarrow n \tag{2.10}$$

The composition of both C and D are shown to be invertible and a unique one-to-one mapping exists between the potential and ground-state densities, the set of densities from the ground state is known as interacting v-representable densities.

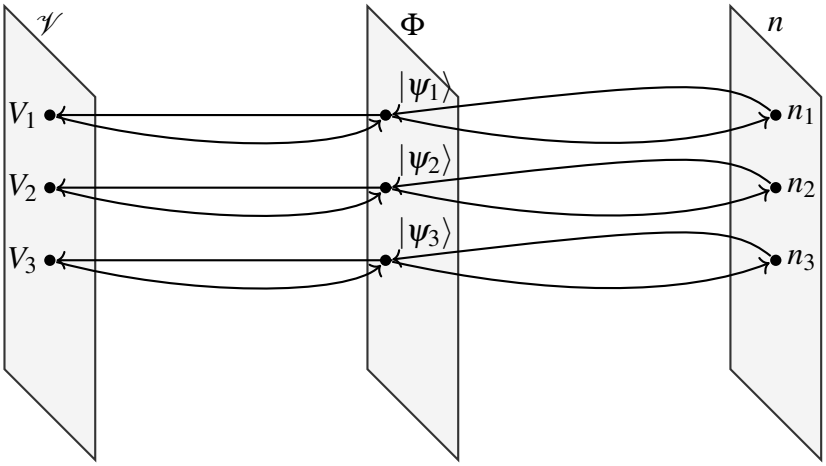

Figure 2.1: Hohenberg-Kohn mapping.

(Hohenberg-Kohn) The density n corresponding to a non-degenerate ground state specifies the external potential $\mathscr{V}$ up to a constant and the ground state wavefunction $|\Psi[n]\rangle$ up to a phase factor.

1. Any ground state expectation value corresponding to an observable $\hat{O}$ is a functional of the density according to

$$O[n] = \langle \Psi[n] | \hat{O} | \Psi[n] \rangle$$

2. The ground state energy of a system with a non-degenerate ground state and an external potential v can be obtained from

$$E[n] = \inf_{n \in \rho} \left\{ \int n(\mathbf{r}) v(\mathbf{r}) \, d\mathbf{r} + F_{\mathrm{HK}}[n] \right\}$$

The universal functional $F_{\mathrm{HK}}[n]$ includes $\hat{T}$ is the total kinetic energy operator, and $\hat{V}_{ee}$ is the electron-electron interaction operator.

$$F_{\mathrm{HK}}[n] = \langle \Psi[n] | \hat{T} + \hat{V}_{ee} | \Psi[n] \rangle.$$

Theorem 1. *(Hohenberg-Kohn) further showed that the density functional E[n] has a*

variational property where the ground state energy of the system is obtained through minimisation of the functional concerning the ground state density.

$$\min_{\rho(\boldsymbol{r})} \langle \Psi | H | \Psi \rangle = E[\tilde{n}] \geq E[\tilde{n}]$$

This scheme allows us to solve the ground state as a function of the density, knowing the external potential. For our DFT minimization with the constraint $\int \rho(\mathbf{r})\, dr = N$, where μ is simply a Lagrange multiplier we have:

$$\frac{\delta}{\delta \rho(r)} \left(E[\rho] - \mu \int \rho(r)\, dr - N \right) = 0 \tag{2.11}$$

which simplifies to:

$$\frac{\delta E[\rho]}{\delta \rho(r)} - \mu = 0 \tag{2.12}$$

Given that:

$$E[\rho] = \int \rho(r) v(r)\, dr + F[\rho]_{HK} \tag{2.13}$$

We obtain the Euler–Lagrange equation:

$$\mu = v(r) + \frac{\delta F[\rho]}{\delta \rho(r)} \tag{2.14}$$

The Hohenberg-Kohn theorems constrain the search over $n(\boldsymbol{r})$ where they are said to be v-representable. Since many different Ψ can lead to many ρ we first search over minimum such that we find $\Psi \to \rho_{min}$ and hence now we search for the lower bound ρ which minimises the HK energy functional. The Hohenberg-Kohn theorems can thus be reformulated as the minimisation of a v-representable density that minimises the energy to a set of N-representable densities.

$$E_0 = \min_{\Psi} \langle \Psi | \hat{T} + \hat{V}_{ee} + \sum_i v(r_i) | \Psi \rangle \tag{2.15}$$

$$= \min_{\rho} \left(\min_{\Psi \to \rho} \langle \Psi | \hat{T} + \hat{V}_{ee} | \Psi \rangle + \int v(r) \rho(r)\, dr \right) \tag{2.16}$$

$$= \min_{\rho} \left(F[\rho] + \int v(r) \rho(r)\, dr \right) \tag{2.17}$$

Due to the variational property of the 2nd Hohenberg-Kohn theorem, we do not know the conditions for v-representable densities; the Lieb and Levy constraints overcome this by searching over all states that are not mutually exclusive to just the v-representable density, since many wavefunctions can lead to the same

density. We only need to consider N-representable densities (i.e., those associated with an antisymmetric N-electron wavefunction Ψ). The v-representability problem is eliminated, making the formulation easier.

$$\mu = v(r) + \frac{\delta F[\rho]}{\delta \rho(r)} \tag{2.18}$$

$$= v(r) + \frac{\delta T[\rho]}{\delta \rho(r)} + \frac{\delta V_{ee}[\rho]}{\delta \rho(r)} \tag{2.19}$$

2.4 Kohn-Sham equation

The Kohn-Sham formulation of [14] introduces an auxiliary system of non-interacting electrons with a single Slater determinant that has the same electron density as the interacting case. From the H-K theorem, the ground state density will minimise the energy functional.

$$\frac{\delta}{\delta \rho(\mathbf{r})} \left(E[V_{\text{ext}}(\rho)] - \mu \int \rho(\mathbf{r})\, d\mathbf{r} \right) = 0$$

The Lagrange multiplier μ is used to constrain the density N. The total energy expression functional is separated into

$$E[V_{\text{ext}}][\rho] = T_s[\rho] + E_H[\rho] + E_{\text{XC}}[\rho] + \int \rho(\mathbf{r}) V_{\text{ext}}(\mathbf{r})\, d\mathbf{r},$$

where $E_H[\rho]$ is the Hartree energy given by

$$E_H[\rho] = \frac{1}{2} \int dr dr' \frac{\rho(\mathbf{r})\rho(\mathbf{r}')}{\mid r - r' \mid} \tag{2.20}$$

and the exchange correlation functional $E_{XC}[\rho]$

$$E_{EX}[\rho] = T[\rho] - T[\rho]_s + V_{ee}[\rho] - E_H[\rho] \tag{2.21}$$

where $T[\rho]$ is the interacting kinetic energy operator and $T[\rho]_s$ the non interacting kinetic energy operator for the electrons. Minimising the Kohn–Sham energy expression

$$E = \int \rho(\mathbf{r}) v(\mathbf{r})\, \mathrm{d}\mathbf{r} + T_s[\rho] + E_H[\rho] + E_{\text{XC}}[\rho] \tag{2.22}$$

With respect to the density $\rho(\mathbf{r})$ (subject to fixed N), it gives the Euler equation:

$$\mu = v_{\text{eff}}(\mathbf{r}) + \frac{\delta T_s[\rho]}{\delta \rho(\mathbf{r})}, \tag{2.23}$$

where

$$v_{\text{eff}}(\mathbf{r}) = v(\mathbf{r}) + \frac{\delta J[\rho]}{\delta \rho(\mathbf{r})} + \frac{\delta E_{\text{XC}}[\rho]}{\delta \rho(\mathbf{r})}. \tag{2.24}$$

where $v(r)$ is the external potential, J is coulomb term and E_{XC} is the exchange correlation functional

Equation (2.23)—which yields the exact density of the system—is just the conventional DFT Euler equation:

$$\mu = v(\mathbf{r}) + \frac{\delta T[\rho]}{\delta \rho(\mathbf{r})} + \frac{\delta V_{ee}[\rho]}{\delta \rho(\mathbf{r})}. \tag{2.25}$$

when non interacting kinetic functional $T_s[\rho] = T[\rho]$ and $V_{ee}[\rho] = 0$ we have established that $V_{KS}(\rho)$ and the density is equal $\rho_s = \rho$ as depicted in figure 2.2

Figure 2.2: Kohn-Sham picture

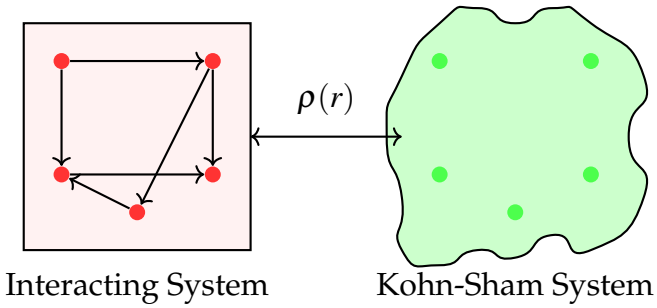

The particles are non-interacting and therefore separable; the independent N-particle Hamiltonian of the auxiliary system can be written as the sum of N single-particle Hamiltonians.

$$\left[-\frac{1}{2}\nabla^2 + v(r) + \frac{\delta J[\rho]}{\delta \rho(r)} + \frac{\delta E_{\text{XC}}[\rho]}{\delta \rho(r)}\right] \phi_i(r) = \varepsilon_i \phi_i(r), \tag{2.26}$$

where ϕ_i are single-particle wavefunctions are known as Kohn-Sham orbitals, and the density of the Kohn-Sham system is given by

$$\rho(r) = \sum_{i=1}^{X} \phi_i^*(r)\phi_i(r). \tag{2.27}$$

The kinetic energy is given by:

$$T_s[\rho(r)] = -\frac{1}{2}\sum_{i=1}^{N} \int dr\, \phi_i^*(r)\nabla^2\phi_i(r). \tag{2.28}$$

The Kohn-Sham equation forms an analogue of the one-particle Schrödinger equation, where the exact density can be found by solving the Kohn-Sham ef-

fective potential. Unfortunately, the exchange-correlation and Hartree function are dependent on $\rho(\mathbf{r})$ and the ground state density cannot be calculated with an analytic solution. A self-consistent approach is used whereby some initial guess of the density ρ^{in} is used to solve $\hat{H}_{KS}[\rho^{in}]\phi_i(r) = \varepsilon[\rho]\phi_i(r)$ until $\rho^{in} = \rho^{out}$ where ρ^{out} is self-consistent density.

2.5 Theory of Lattice Dynamics

Lattice vibrations are described using quasi-particles called phonons, which are collective oscillations at a given frequency. We define the atomic positions as displacements $\mathbf{u}$ from their equilibrium positions $\mathbf{R}_i$ at lattice vector $\boldsymbol{\tau}_i$.

$$\mathbf{r}_i = \mathbf{R}_i + \boldsymbol{\tau}_i + \mathbf{u}_i.$$

As the ions are displaced by this vibration, this will cause a change in the potential of the lattice, which can be described through a Taylor series expansion of the potential energy, U, where the derivatives Φ are taken about the equilibrium positions.

$$U(\{\mathbf{u}\}) = U_0 + \sum_i \sum_\alpha \Phi_i^\alpha u_i^\alpha + \frac{1}{2!}\sum_{ij}\sum_{\alpha\beta}\Phi_{ij}^{\alpha\beta}u_i^\alpha u_j^\beta + \frac{1}{3!}\sum_{ijk}\sum_{\alpha\beta\gamma}\Phi_{ijk}^{\alpha\beta\gamma}u_i^\alpha u_j^\beta u_k^\gamma + \dots \tag{2.29}$$

If nuclei are treated classically, the problem is reduced to a set of coupled

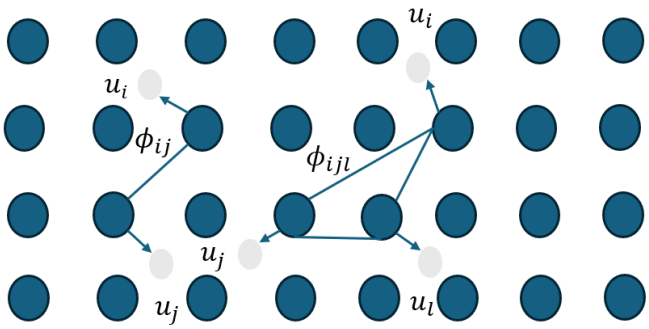

Figure 2.3: 2nd and 3rd order force constants.

equations. Which, in a more compact form, can be written as

$$\ddot{\mathbf{u}}_i m_i = -\sum_{\mathbf{R}} \Phi_{ij}(\mathbf{R})\,\mathbf{u}_j. \tag{2.30}$$

$$\mathbf{u}_i = \frac{1}{\sqrt{m_i}} \sum_{\mathbf{q}} A_{\mathbf{q}} \boldsymbol{\varepsilon}^i_{\mathbf{q}} e^{\mathrm{i}(\mathbf{q}\cdot\mathbf{R}-\omega t)}. \tag{2.31}$$

Here, the displacements are expressed as a sum of plane waves, or normal modes, each with wave vector $\mathbf{q}$ and frequency ω and ε is a polarisation vector and the normal mode amplitude $\mathbf{A_q}$. Substituting this into the eigenvalue equation using the orthogonality of plane waves gives,

$$\omega^2_{\mathbf{q}} \boldsymbol{\varepsilon}^i_{\mathbf{q}} = \Phi(\mathbf{q}) \boldsymbol{\varepsilon}^i_{\mathbf{q}} \tag{2.32}$$

The dynamical matrix is a $3N \times 3N$ block matrix consisting of 3×3 submatrices. For a supercell containing n primitive cells, the corresponding force-constant matrix (FCM) has dimensions of $3nN \times 3nN$, where N represents the number of atoms per primitive cell.

$$\Phi(q) = \begin{bmatrix} \Phi_{11}(q) & \cdots & \Phi_{1N}(q) \\ \vdots & \ddots & \vdots \\ \Phi_{N1}(q) & \cdots & \Phi_{NN}(q) \end{bmatrix} \tag{2.33}$$

More explicitly, each sub-matrix is defined as the Fourier transform of the second-order force-constant matrix:

$$\Phi_{ij}(q) = \sum_R \Phi_{ij}(R) \frac{e^{iq\cdot R}}{\sqrt{m_i m_j}} \tag{2.34}$$

It can be shown that the dynamical matrix is Hermitian, so the eigenvalues ω^2 are real, as the dynamical matrix is fully diagonalisable for any wavevector q.

The eigenvectors ($\mathbf{e}_{qj}$) and eigenvalues (ω^2_{qj}) of the dynamical matrix evaluated at a particular wavevector q then correspond to the eigenmodes of vibration of the crystal for that wavevector.

2.5.1 Harmonic approximation

Lattice dynamics derived from section 2.5 assumes the Describing the atomic motion as small oscillations near the equilibrium configuration. Writing down a second-order term representing the total potential felt by the ions is known as the harmonic approximation[15]. The first term is simply the energy when the ions are at equilibrium. The second term is the derivative with respect to atomic displacements, where, in equilibrium, the forces are zero. The third term is the second derivative with respect to atomic displacements, as given in this

equation. In most cases, the higher-order terms such as the 4th and 5th order terms are neglected, and the expansion is truncated to a quadratic 2nd-order term whose force constant matrix (FCM) expresses the constant proportionality between displacements and forces.

$$U(\{\mathbf{u}\}) = \frac{1}{2!} \sum_{ij,\alpha\beta} \Phi_{ij}^{\alpha\beta} u_i^{\alpha} u_j^{\beta} \Big|_{\text{eq}}$$

By solving the harmonic case, the solutions are easily solvable for each phonon mode, in which case there are 3N where N is number of atoms of these that can be treated as a set of harmonic oscillators. The harmonic approximation works very well, practically. The approximation is sufficient to extract the phonon dispersions from DFT calculations and quasi-harmonic properties.

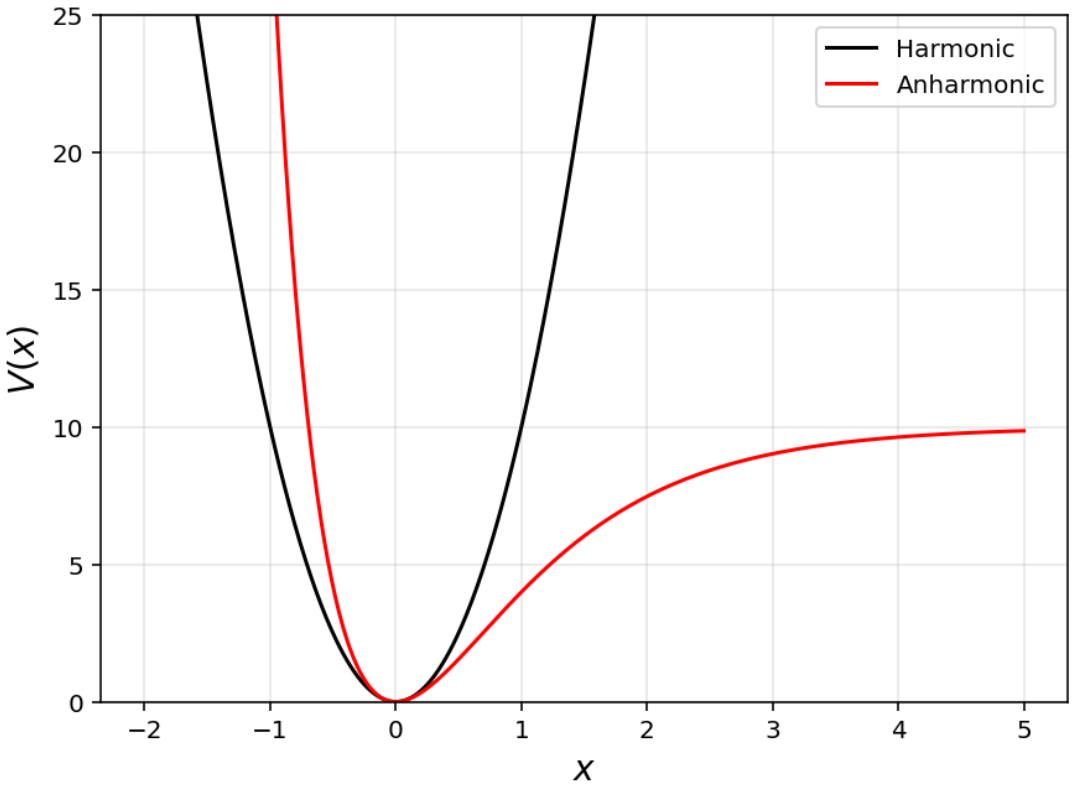

Figure 2.4: Simple case of harmonic and anharmonic potential wells where the PES has been effectively perturbed.

2.5.2 Anharmonic Phonons

Phonons within the harmonic approximation are non-interacting, leading to infinite scattering. Therefore, anharmonic phonons are a temperature dependent quantity which contributes to the true energy landscape of higher-order perturbation terms in the expansion about the Taylor series.

$$
\begin{aligned}
U(\{\mathbf{u}\}) = \frac{1}{2!}\sum_{ij,\alpha\beta}\Phi_{ij}^{\alpha\beta}u_i^{\alpha}u_j^{\beta}\Big|_{\mathrm{eq}} \\
+\frac{1}{3!}\sum_{ijk,\alpha\beta\gamma}\Phi_{ijk}^{\alpha\beta\gamma}u_i^{\alpha}u_j^{\beta}u_k^{\gamma}\Big|_{\mathrm{eq}} \\
+\frac{1}{4!}\sum_{ijkl,\alpha\beta\gamma\delta}\Phi_{ijkl}^{\alpha\beta\gamma\delta}u_i^{\alpha}u_j^{\beta}u_k^{\gamma}u_l^{\delta}\Big|_{\mathrm{eq}} \\
+\dots
\end{aligned}
$$

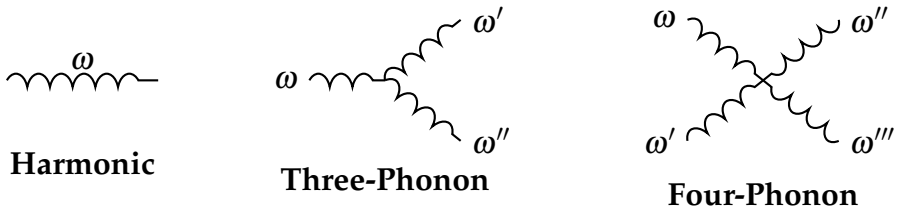

First-principles Boltzmann transport is built from a phonon scattering picture based on Fermi's golden rule.[16] In this picture, intrinsic phonon-phonon interactions are derived from perturbations of the harmonic Hamiltonian.

In a three-phonon scattering process, the phonon undergoes several annihilation and creation events, where a phonon is annihilated, and two phonons are created, the annihilation of two phonons with the creation of another and the creation of three phonons and the annihilation of three phonons. The latter two would violate momentum conservation, but are included as part of the interactions over all possible three-phonon scattering events.

$$
\begin{aligned}
H_3 = \frac{1}{3!}\sum_{q,q',q''}\sum_{j,j',j''}\frac{h^{\frac{2}{3}}}{2^{\frac{3}{2}}N^{\frac{1}{2}}}\Phi(q_j,q'_{j'},q''_{j''})\sqrt{\omega_{q_j}\omega_{q'_{j'}}\omega_{q''_{j''}}}\,\delta_{q+q'+q'',G} \\
\times(a^{\dagger}_{-q_j}+a_{q_j})(a^{\dagger}_{-q'_{j'}}+a_{q'_{j'}})(a^{\dagger}_{-q''_{j''}}+a_{q''_{j''}})
\end{aligned}
\tag{2.35}
$$

where $\Phi(q_j,q''_{j'},q''_{j''})$ is the three-phonon matrix element obtained from the cubic force constants by Fourier transform, q,q',q'' are the wave vectors of the three phonons involved in the process, and G is the reciprocal lattice vector. The δ-function guarantees momentum conservation in these processes. The last three terms of the three-phonon process represent the different processes of the creation and annihilation of the three phonons; this is just to keep track of the number of phonons during the process.

2.6 Phonons from Molecular Dynamics

Molecular Dynamics (MD) provides an alternative to extracting phonon properties from a quasi-harmonic lattice dynamics simulation. The Lennard-Jones potential (LJP) model may be used to approximate the PES in 1D. Through MD runs, we can analytically derive force constant k by taking derivatives of LJP up to third order in a simple Taylor series expansion and fitting the coefficients of ε and σ of a Lennard-Jones potential.

$$U(r) = 4\varepsilon\left[\left(\frac{\sigma}{r}\right)^{12} - \left(\frac{\sigma}{r}\right)^{6}\right] \tag{2.36}$$

where ε is the depth of the potential well, σ is the interatomic distance at which the potential is zero. Taking the nth derivative $\frac{d^n U}{dr^n}$ expressed by the Taylor series expansion of the equation above, will yield the force, and the second derivative will give us the force constant k, and the third derivative is the anharmonic component.

To determine the equilibrium separation r_0, we first find the interatomic force by differentiating the potential $V(r)$ with respect to r, yielding $F(r) = -\frac{dV(r)}{dr}$. The equilibrium condition requires the net force to be zero, $F(r_0) = 0$. Solving this equation yields the equilibrium distance $r_0 = 2^{1/6}\sigma$.

We then evaluate the Taylor expansion of the potential around this equilibrium distance. The effective force constant k is obtained from the second derivative of the potential evaluated at $r = r_0$, given by

$$k = \left.\frac{d^2V(r)}{dr^2}\right|_{r=r_0}.$$

Finally, the vibrational frequency ω is related to this force constant and the atomic mass by $\omega = \sqrt{k/m}$ where m is the atomic mass, and a is the lattice constant.

$$\omega = \sqrt{\frac{2 \times 1512\varepsilon}{m x_0^3}}\left|\sin\left(\frac{ka}{2}\right)\right| \tag{2.37}$$

To illustrate, using a simple pair potential derived from the MD data of a 1D chain H_2 dimer as the simplest working example. Numerically, this works out well since calculations performed at 0 K with DFT require perturbation corrections for volume and temperature effects, whereas the MD contains such effects that are absent in the DFT. Induced changes on the PES will result in differences in the lattice dynamics.

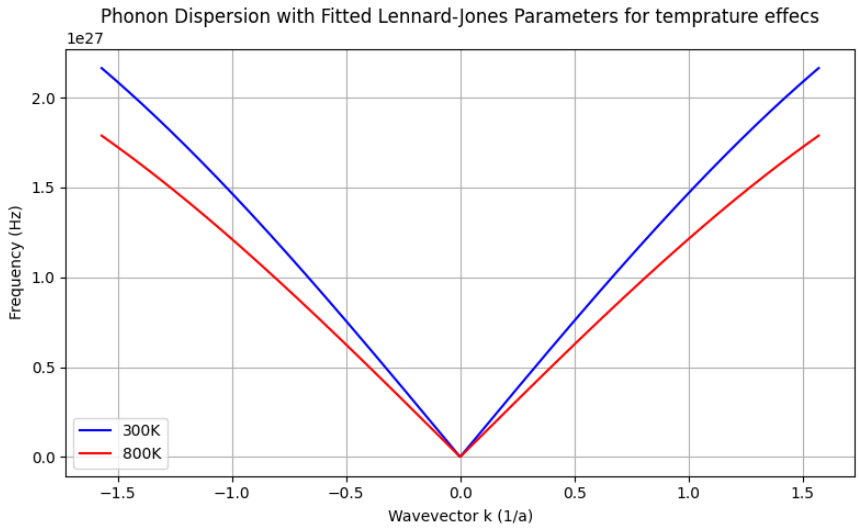

Figure 2.5: The effect of temperature is that the phonon branches have become softer.

2.6.1 The Kong Method

Any fitted interatomic potential can be used to calculate The force constant matrix, provided the correct forces and energy are properly converged for direct sampling of modes. The Kong method[17] developed and merged with the LAMMPS package[18] calculates the average displacement correlation function that is the inverse of the force constant matrix.

MD simulations incorporate thermal effects through the explicit sampling of numerous configurations of atomic vibrations in phase space. Statistical sampling over a large set of different configurations generated at each time step represents a linear combination of the phonon eigenmodes in the system.

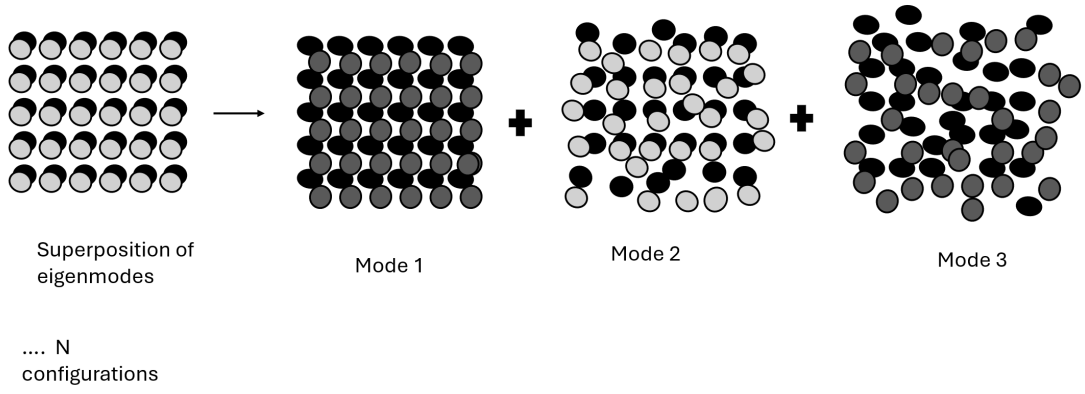

Figure 2.6: Phonon modes contained within an average of sampled configurations represent a linear combination of phonon modes.

$$G_{ig} = \beta \langle u_i u_j \rangle = [\Phi^{-1}]_{ij}, \tag{2.38}$$

where $\beta = \frac{1}{k_B T}$ and $\langle ... \rangle$ is the ensemble average.

The correlation function in thermal equilibrium over the distribution of displacements is written out fully as

$$G_{ij} = \langle u_i u_j \rangle = \frac{\int du_1 \cdots du_N \, u_i u_j e^{-\beta V}}{\int du_1 \cdots du_N \, e^{-\beta V}} = \frac{1}{Z} \int du \, u_i u_j e^{-\beta V} \tag{2.39}$$

For a harmonic potential of the form

$$V^{\text{harm}} = \frac{1}{2} \Phi_{kl} u_k u_l, \tag{2.40}$$

The partition function is

$$Z = \int du_1 \cdots du_N \exp\left(-\frac{\beta}{2} \Phi_{kl} u_k u_l \right) \tag{2.41}$$

We now compute the derivative of $\ln Z$ with respect to Φ_{ij}, knowing the relation.

$$-\frac{\partial \ln Z}{\partial \Phi_{ij}} = -\frac{1}{Z} \cdot \frac{\partial Z}{\partial \Phi_{ij}} \tag{2.42}$$

Using the standard integral solution for a Gaussian now yields the final solution

$$G_{ig} = \beta \langle u_i u_j \rangle = [\Phi^{-1}]_{ij} \tag{2.43}$$

Restating the correlation function as a function of atomic positions makes it easier to measure the atomic positions rather than the displacements, as implemented in LAMMPS.

$$\begin{aligned} \widetilde{G}_{\alpha,\beta}(\mathbf{q}) &= \langle \widetilde{u}_\alpha(\mathbf{q}) \widetilde{u}^*_\beta(\mathbf{q}) \rangle \\ &= \left\langle \left[\widetilde{R}_\alpha(\mathbf{q}) - \widetilde{R}^0_\alpha(\mathbf{q}) \right] \left[\widetilde{R}_\beta(\mathbf{q}) - \widetilde{R}^0_\beta(\mathbf{q}) \right]^* \right\rangle \end{aligned} \tag{2.44}$$

For a very strongly anharmonic force component, the third-order perturbative approach assumes that the anharmonic correction is small enough to be justified as a perturbation; however, this can be achieved through DFT with supercell perturbations These calculations are computationally expensive with the fourth-order force constants, as system size introduces practical limitations.

Whilst perturbative expansions tend to be the standard way of performing these calculations, the FCM at $T = 0$ is not a good approximation to the true

temperature effective as the force constant matrix a $T = 0$ breaks down for very anharmonic materials, leading to an overestimation of Phonon lifetime and hence thermal conductivity. Molecular dynamics benefits from having all the physical effects of temperature without having to do small perturbations to correct this.

In the phonon picture, sampling of many different displacement configurations is needed to converge the FCM; this depends on the potential used and how well the interactions are captured within the system. This may range from a few million timesteps to much more, for which a full AIMD calculation simply would not be an efficient way of producing that many timesteps needed to converge the FCM through the Kong method.

2.6.2 Symmetrization of FCM Method

The limitation of the Kong Method is the need for long trajectories and large supercells supercells. Getting the force constant matrix from DFPT or finite displacement ensures that the symmetry operation is enforced by the two sum rules discussed in the phonons section. Within any of the MD formalisms discussed, they lack the appropriate symmetry. To impose symmetry constraints on the FCM is very difficult because you are essentially random sampling displacement configurations where there is no simple physics which could enforce symmetry on totally randomised structures.

A method devised by Hellman[19] to achieve a symmetrised force constant matrix was to create a harmonic model from sampling an MD trajectory and find the best FCM that minimises the error in the MD forces and those derived from the FCM. This then means that the FCM includes the anharmonic and finite $\mp T$ effects to higher order terms in the Taylor series expansion.

With the Kong method needing many timesteps to converge the FCM correctly this method relies on direct sampling and fitting FCM via least squares approach.

By enforcing translational and rotational invariance rules back into FCM from adding symmetry back into FCM to correct this, we now gain a huge advantage because we can reduce the number of equivalent positions of ions, speeding up the time required to calculate higher-order FCM through

$$S^2 = \sum_{t,i} \frac{1}{N_t} \left| F_i^{(t)} - \tilde{F}_i^{(t)} \right|^2 \tag{2.45}$$

where $\tilde{F}_i^{(t)}$ are the forces from the optimal best fitted FCM.

$$\tilde{F}_i^{(t)} = \sum_j \phi_{ij} u_j^{(t)},$$

Calculating phonon dispersions using *ab initio* molecular dynamics (AIMD) is computationally costly. Extracting accurate phonon properties requires extensive sampling over long simulation times and large supercells to capture all vibrational modes. Because AIMD evaluates the electronic structure at every single time step, its computational cost scales $\mathcal{O}(N_{\text{elec}}^3)$ with the number of electrons.

Consequently, the simulation time is heavily reliant on the chosen system; for instance, a compound like PbTe possesses significantly more electrons than LiF, making AIMD more expensive and entirely impractical for generating the necessary trajectory lengths.

To overcome this, classical molecular dynamics forcefields are used to drastically reduce the computational cost. Therefore, Machine Learning Interatomic Potentials (MLIPs) offer an optimal compromise. By training with on-the-fly AIMD or regular AIMD data over few thousand configurations, MLIPs can reproduce very accurate *ab initio* forces and energies with suitable for studying phonon properties while evaluating at a fraction of the computational cost.

2.6.3 Phonon Dispersions of Si

A simple Tersoff potential for Si is used as an example to predict the phonon dispersion through the extraction of the force constant matrix (FCM) from molecular dynamics simulations. The direct sampling of MD trajectories, as proposed by Kong, is slower to converge the FCM but yields highly accurate results given sufficiently long MD runs. However, this approach requires extensive computational time. In contrast, the symmetrization method converges much faster, eliminating the need for long trajectory runs. However, it can be less accurate.

Because this method relies on regression to approximately fit the force constant matrix, its accuracy degrades when the system exhibits strong anharmonicity. Specifically, the harmonic regression struggles to capture the true potential energy surface when there are large fluctuations in the atomic forces, leading to significant fitting errors.

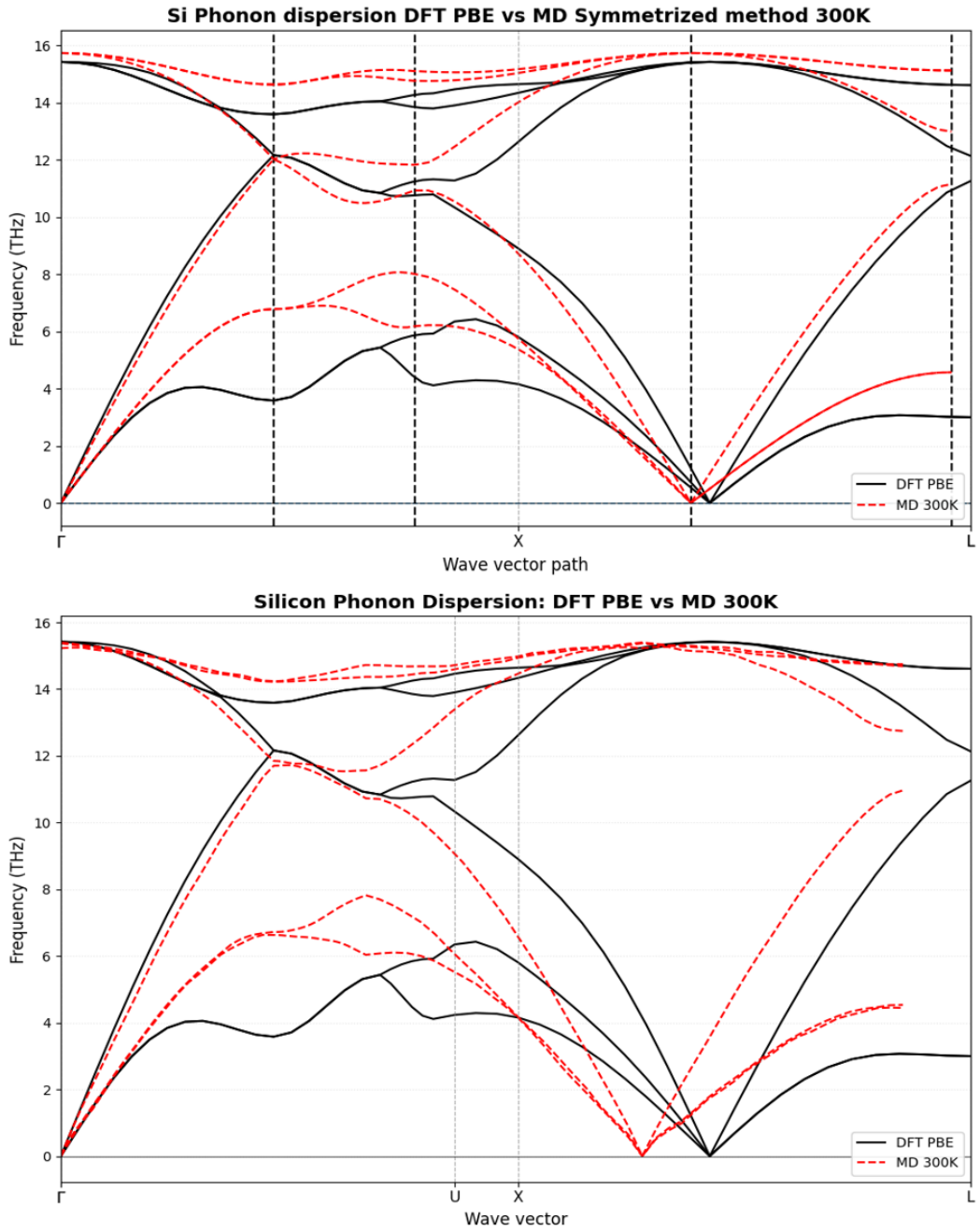

Figure 2.7: Comparison of phonon band structures calculated using DFPT and Symmetrization method/Kong where the MD uses a Tersoff potential.

2.7 Phonon Lifetimes

The phonon self-energy (Δ) $\Sigma = \Delta + i\Gamma$ consists of two parts, real (Δ) and imaginary $(i\Gamma)$ parts, where the lifetime due to phonon-phonon scattering is related to the imaginary part. The imaginary part is calculated using the Fermi golden rule, which calculates the probability of phonon-phonon scattering[20].

$$\begin{aligned}\Gamma_\lambda = \frac{\hbar\pi}{16}\sum_{\lambda'\lambda''}|\Phi_{\lambda\lambda'\lambda''}|^2\Big[&(n_{\lambda'}+n_{\lambda''}+1)\delta(\omega_\lambda-\omega_{\lambda'}-\omega_{\lambda''})\\&+2(n_{\lambda'}-n_{\lambda''})\delta(\omega_\lambda-\omega_{\lambda'}+\omega_{\lambda''})\Big]\end{aligned} \tag{2.46}$$

$\Phi_{\lambda\lambda'\lambda''}$ is the Phonon-phonon scattering matrix elements over three phonon processes as in (2.35); the terms on the RHS of this equation are to keep the number of processes conserved in the continuum of states.

The lifetime associated with this process is just equal to the reciprocal of τ

$$\frac{1}{\tau_\lambda} = 2\Gamma_\lambda, \tag{2.47}$$

The real part (Δ) is defined by the Kramers-Kronig relations and is the real energy shift.

$$\Delta = \mathscr{P}\frac{1}{\pi}\int\frac{\Gamma(\omega)}{\omega-\Omega}d\omega. \tag{2.48}$$

where we use (Ω) to distinguish this energy from the eigenvalues of the dynamical matrix, (ω). In a non-interacting harmonic system, phonons have an infinite lifetime due to the absence of phonon-phonon scattering. This results in a Dirac delta function as the broadening parameter, Γ, is zero, and there is no energy shift. In contrast, an interacting system has a finite phonon lifetime, where Γ represents the broadening of the phonon peak at a given energy. The full width at half maximum (FWHM) of this peak is directly related to the phonon lifetime.

According to Matthiessen's rule, the total phonon scattering rate is the sum of rates from different scattering mechanisms, not limited to phonon-phonon interactions. This has important implications for the reliability of calculated phonon lifetimes.

In an ideal, defect-free crystal, the absence of defect-induced scattering will impact the lifetime. However, materials at finite temperature have lattice imperfections and anharmonic effects. All of these factors affect the phonon lifetimes and frequencies, necessitating a renormalisation of phonon modes to account for temperature-induced changes.

2.8 Phonon Lifetimes through MD of Si

2.8.1 Mode Decomposition

There are also several equivalent ways in MD [21] to obtain the lifetime. The Energy correlation function $\frac{<E_q(0)E_q(t)>}{<E_q(0)E_q(0)>}$, where energy E represents the total energy of each phonon mode q, consists of KE and potential parts. Computing the exponential decay of the correlation function gives the lifetime.

$$\frac{\langle E_{\mathbf{q},\nu}(t)\, E_{\mathbf{q},\nu}(0)\rangle}{\langle E_{\mathbf{q},\nu}(0)\, E_{\mathbf{q},\nu}(0)\rangle} = \frac{\int_0^\infty E_{\mathbf{q},\nu}(t'+t)\, E_{\mathbf{q},\nu}(t')\, d\xi}{\int_0^\infty E_{\mathbf{q},\nu}(t')\, E_{\mathbf{q},\nu}(t')\, dt'} = e^{-t/\tau_{\mathbf{q},\nu}} \tag{2.49}$$

With the exponential decay from the total energy decomposition of the modal energy. Here, we have used silicon to show proof of principle.

$$E_{\mathbf{k},\nu}(t) = \frac{\omega_\nu^2 |q_\nu(t)|^2}{2} + \frac{|\dot{q}_\nu(t)|^2}{2}$$

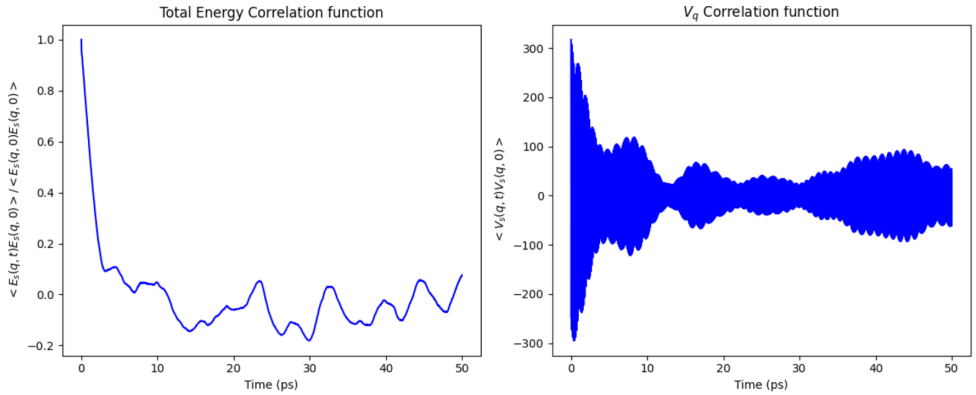

Figure 2.8: Total mode-resolved energy and velocity autocorrelation functions of Si at Γ simulated for 300ps at 300K using NVT.

Likewise The projected velocity, $< V_q(0)V_q(t) >$ autocorrelations is proportional to $A_q cos(\omega_q t)e^{(-t/2\gamma_q)}$. So, a single fit can give us both frequency, ω_q, and lifetime, γ_q. Finally, the best way to extract the information is via the power spectrum of the velocity autocorrelation function:

$$G_q(\omega) = \left| \int_0^\infty \langle V_q(0) \cdot V_q(t) \rangle\, e^{i\omega t} d\omega \right|^2 \tag{2.50}$$

While it seems easy enough to extract information from this analysis, it is actually quite difficult to get the lifetime from these calculations. Autocorrelations must go to zero; you see oscillations at the tail. This is because slower modes require longer data to show a proper decay. So, you need a different set of

data with a different Δt or *dump-interval* to sample each one of them properly. If you explore the q points and different modes, you can easily find that some correlation functions didn't converge. Because of this, other pictures are usually considered, especially those in the frequency domain. For example, the projected velocity correlation function

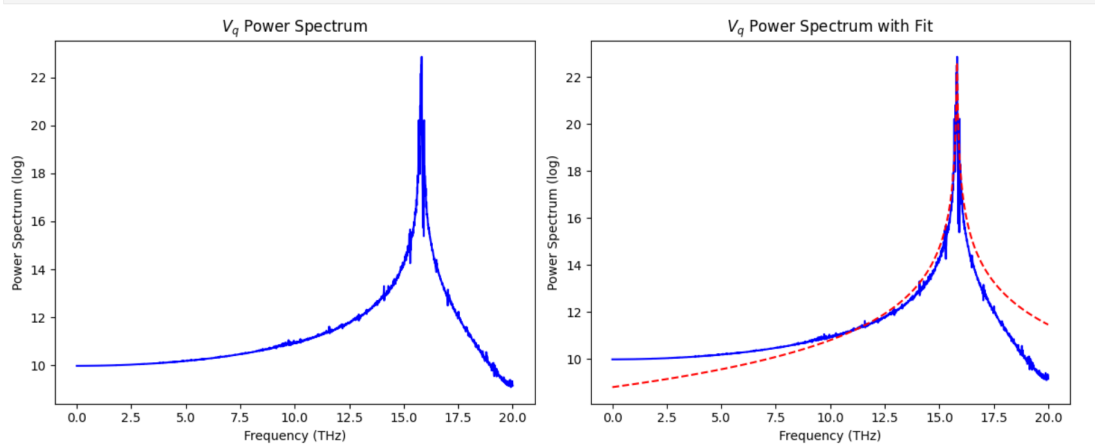

Figure 2.9: power spectrum of Si and fitting via Lorentzian function at Γ peak.

The choice of the Lorentzian function comes from time-dependent-normal mode coordinate for an anharmonic system, i.e the lowest order interacting phonon-phonon scattering which leads to a lifetime. The Fourier transform of equation 2.49 leads to a Spectral Energy Density SED of the form of a Lorentzian.[22] [23]

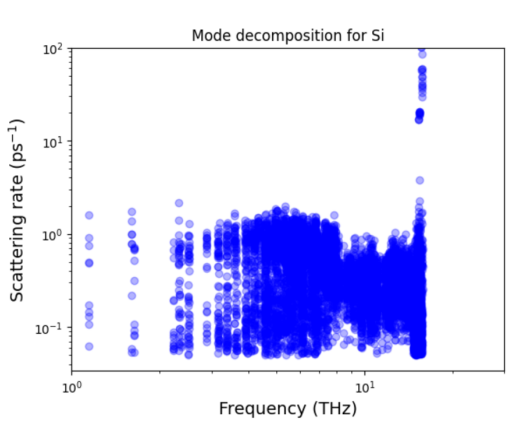

(a) Lifetime scattering points for mode decomposition for all q.

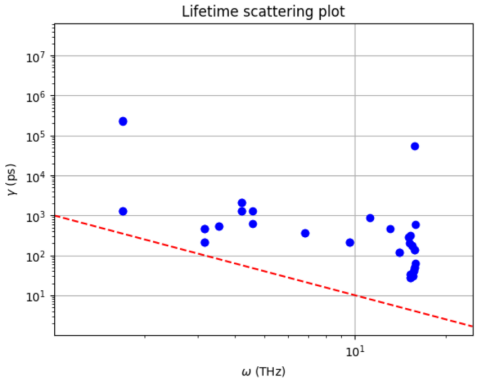

(b) Phonon lifetime scattering of Si and fitted data via Velocity Autocorrelation function at Γ.

Figure 2.10: Phonon lifetime scattering points via two different methods

Figure 2.10 illustrates the distribution of phonon lifetimes as a function of frequency for silicon at 300 K. The multiple data points observed at any given frequency are a direct consequence of the phonon dispersion relation, $\omega(\mathbf{q}, s)$. Because the frequency depends on both the wavevector $\mathbf{q}$ and the branch index

s, many distinct phonon modes can possess the same frequency ω. However, because the phonon-phonon scattering phase space depends strictly on the specific $\mathbf{q}$ and s of the mode, each of these distinct states experiences a different scattering rate, resulting in a distribution of lifetimes for a single frequency value.

The corresponding number of phonon-phonon scattering events for any given frequency is shown in Figure 2.10(b). While evaluating scattering events specifically at the Γ point is sometimes used as a simplified approximation, computing the full autocorrelation functions for all modes across the Brillouin zone is computationally expensive and can quickly exhaust available memory. To overcome this bottleneck, we employ the mode decomposition method alongside the velocity autocorrelation function to efficiently extract the mode-resolved lifetimes without requiring prohibitive computational resources.

2.8.2 Spectral Energy Density (SED)

The spectral energy density (SED) is obtained by projecting the atomic positions in a crystal onto the normal modes of vibration [22]. The contribution to the normal mode amplitude arises from the atomic displacement $u_{a,i}(t)$, which represents the displacement in the unit cell. The total SED function does not depend on the eigenvectors, which include the lifetime and frequencies directly from MD.

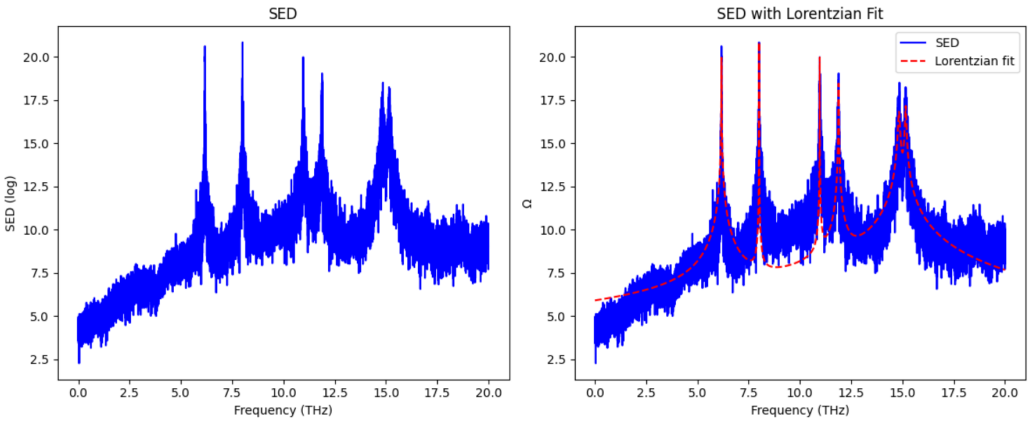

Figure 2.11: Spectral Energy Density of Si with fitting of Lorentzian function at Γ

$$\Omega(\mathbf{q},\omega) = \left| \frac{1}{4\pi t_0 N} \sum_a m_a \int_0^{t_0} \sum_i \dot{u}_{a,i}(t) e^{i\mathbf{q}\cdot\mathbf{r}_i - i\omega t}\, dt \right|^2$$

The Spectral Energy Density method offers an alternative approach that does not rely on these force constants and can extract both frequencies and lifetimes, but it also becomes less accurate at elevated temperatures. By combining both

methods into a single workflow, many of these limitations can be reduced, resulting in more reliable predictions across a wider temperature range.

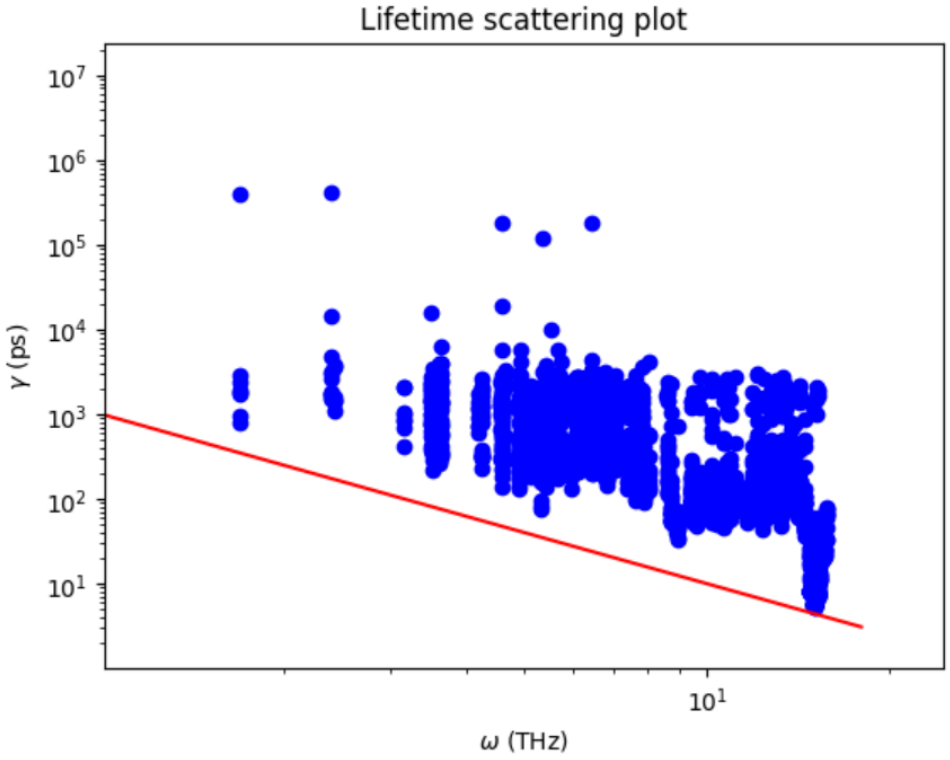

Figure 2.12: Phonon lifetime scattering points of Si.

Chapter 3

Methodology

3.1 CASTEP

3.1.1 Bloch's Theorem

Density functional theory (DFT) calculations were performed using the CASTEP program[24] (which uses a plane wave basis) to calculate the properties of materials. Several properties can be calculated using CASTEP, in particular, interest is in vibrational properties such as phonon properties and MD.

Plane-wave basis sets are chosen to best describe the wave function in the periodic cell but as Kohn-Sham theory scales as $\mathcal{O}(N^3)$ it puts a practical limit on the number of atoms in the system. CASTEP deals with periodic boundary conditions for many infinitely repeating cells, which are generally made up of a basic repeating unit cell, where even molecular systems are put in a box by representing a crystal-like system with an infinite number of translations in all directions.

Bloch's theorem allows the electron wavefunction can vary from one unit cell by a phase factor a more mathematical approach to Bloch's theorem is derived from the idea that the commutator of the Hamiltonian H and translation operator T , $[H,T] = 0$, commutes, such that both T and H share an eigenbasis of the Hamiltonian, which is proven by the set of compatible observables. This guarantees that the Hamiltonian and the electron density are guaranteed to be also periodic.

$$\psi_{bk}(r) = u_{bk}(r)e^{ik\cdot r} \tag{3.1}$$

Where the plane wave has a phase factor with wave vector k extended over the 1st Brillouin zone, and $u_{bk}(r)$describes the cell periodic function.

3.1.2 Plane Wave Basis

The cell periodic function in which we calculate the Kohn-Sham states of $u_{bk}(r)$ essentially describes the periodicity of the unit cell, where in k-space we best describe this as a Fourier transform of the potential.

~~where~~

$$u_n(\mathbf{r}) = \sum_{\mathbf{G}} c_{\mathbf{G},n} e^{i(\mathbf{k}+\mathbf{G})\cdot\mathbf{r}}$$

where$G$is a reciprocal lattice vector defined as $G \cdot L = 2\pi n$, where L is the primitive vector of the unit cell. In principle, an infinite number of$G$vectors is needed to fully express the Bloch function.

$$\psi_{b\mathbf{k}}(\mathbf{r}) = \sum_{\mathbf{G}}^{|\mathbf{k}+\mathbf{G}|\leq G_{\text{cut}}} c_{\mathbf{G}b\mathbf{k}} e^{i\mathbf{G}\cdot\mathbf{r}}.$$

Where $\psi_{b\mathbf{k}}$ is the wavefunction that describe a k point of an state b, in which a cut off is used $G_{cut} = \sqrt{2E_{\text{cut}}}$ to describe number of plane waves that with kinetic energy to sufficiently describe the system as the input is used to determine the basis set size without loss of accuracy beyond the cutoff range. The Fourier coefficients c_{Gn} become small when$G$is large, and the series can be truncated. Thus, we form a basis set with plane waves with a wavelength less than the maximum value of G.

Plane-wave basis sets are chosen to accurately describe the electronic wavefunctions within a periodic unit cell. By invoking Bloch's theorem, the infinitely repeating crystal structure can be modelled by evaluating a finite number of **k**-points within the first Brillouin zone. Within this framework, the Kohn-Sham wavefunctions are expressed as a linear combination of plane waves. Because this expansion theoretically consists of an infinite number of plane waves, it must be truncated in practice to remain computationally feasible. This truncation is controlled by a kinetic energy cut-off, E_{cut}, which restricts the basis set to plane waves with kinetic energies below E_{cut}. Consequently, the total energy of the system converges as the energy cut-off (which determines the number of plane waves) and the number of **k**-points are systematically increased.

3.1.3 Pseudopotentials

The implementation of a plane wave basis set is achieved by using pseudopotentials. The external potential which nuclei acts upon electrons is defined

as

$$\hat{V}_{ext} = -\sum_{i}^{M} \frac{Z_i}{|\mathbf{R}_N - \mathbf{r}_i|} \tag{3.2}$$

where this was previously defined at beginning of section 2.2. As $r \to 0$, the potential goes to infinity meaning a very large number of plane waves is needed to describe the innermost core electrons, which makes it impractical. Hence a weaker "pseudopotential" is introduced by including all the effects of the nucleus and the innermost core electrons into a potential which can be represented by a small number of Fourier coefficients for each ion. Both nuclei and core inner electrons are treated as static and not involved in chemical bonding, while only the nuclear effective potential in the region close to the nucleus changes for respective elements.

Within CASTEP, two different types of pseudopotential exist: ultra-soft pseudopotentials (USP), and norm-conserving pseudopotentials (NCP). CASTEP can generate also generate either form of pseudopotentials on-the-fly (OTF). There are sets of well-tested and converged pseudopotentials for the majority of elements in the periodic table from various different DFT codes, which can be found on the website which provides a ranking of updated pseudopotentials [25].

For example the figure below are of NCP for Pb showing the difference between different wavefunctions, pseudo wavefunctions and the local potential which behaves as $\frac{Z}{r}$, which is the bare nuclear potential.

Norm-conserving pseudopotentials are required to have normalization of the valence wavefunction near the nuclei or local region such that square probability amplitude of the pseudo-wavefunction is equal to the corresponding wavefunction in an all-electron calculation. This ensures the scattering of any particular state is the same in a pseudopotential calculation.

By using pseudopotentials as the external potential in the Kohn-Sham equations, we dramatically reduce the number of electron states that need to be explicitly calculated, since we only retain the outer valence electrons involved in bonding. Furthermore, the resulting pseudopotential varies smoothly near the nuclear core, requiring fewer plane waves to converge and significantly reducing the computational cost.

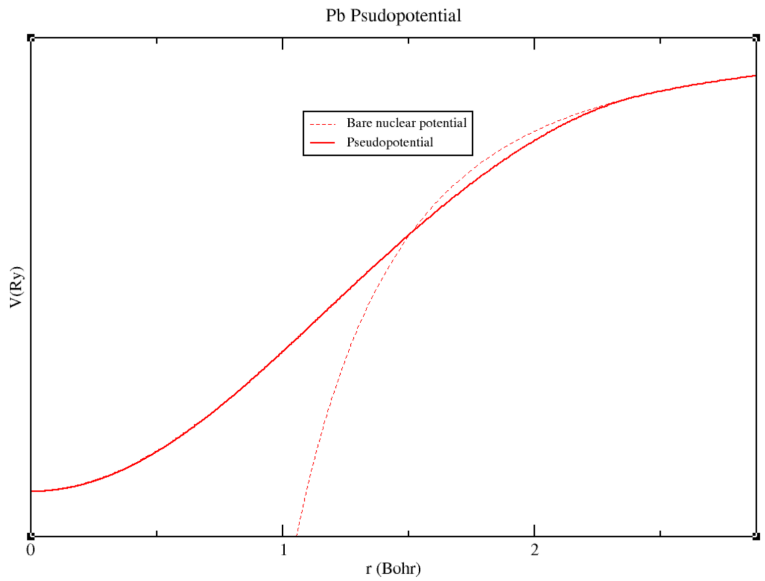

Figure 3.1: Pseudopotential vs bare nuclear potential

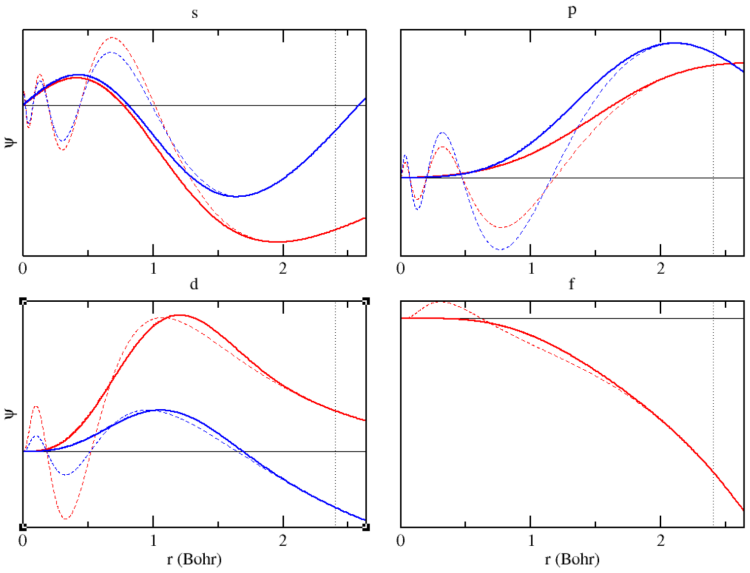

Figure 3.2: Pseudo-wavefunctions for a lead pseudopotential for different angular momentum channels. The solid lines show the pseudo-wavefunctions and the dashed lines show the all-electron wavefunctions.

3.2 Types of calculations

3.2.1 Geometry optimisation

To achieve a high level of precision required for phonon calculations, a geometry optimisation has to be carried out. The force each ion feels is minus the derivative of total energy with respect to position. Such that the forces on the ions are relaxed and are zero.

The electronic energy is minimised between self-consistent field (SCF) steps until change in energy falls below the convergence tolerance. As a general part of CASTEP, the calculation of the net force on each ion includes an adjustment such that the centre of mass force is zero. In terms of phonon calculations, structures that are not well-geometry optimised will yield imaginary frequency modes, indicating instabilities in the system.

Having a relaxed structure is important whenever the exchange correlation functional or the pseudopotentials need to be changed. For example, a non-relaxed structure from Local density approximation LDA and Perdew-Burke-Ernzerhof PBE exchange functionals has the effect of a small potential barrier.

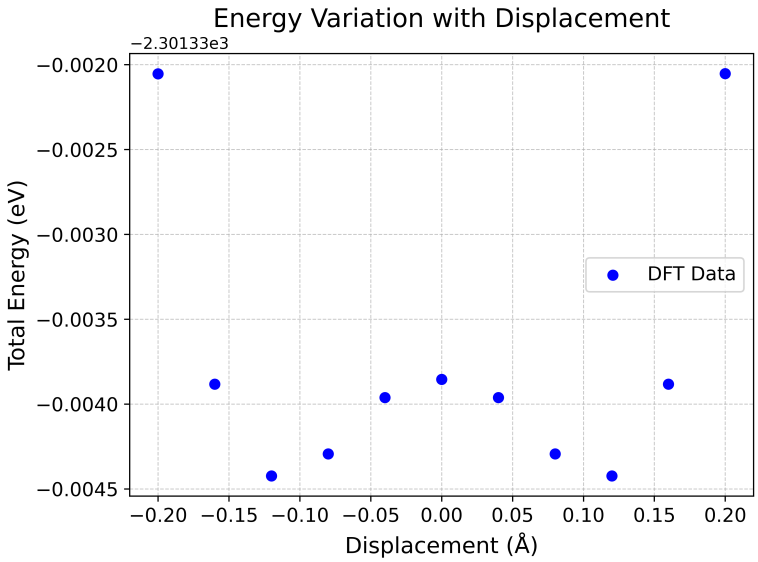

Figure 3.3: Effect of changing XC functional on a structure. The original PbTe structure was optimized using LDA, and then the effect of displacing one atom of Te and calculating the force on Pb is shown. The structure is now clearly unstable.

3.2.2 Phonons

Figure 3.1 illustrates the significance of structural relaxation within the system. It's essential to note that not all structures will necessarily have a single potential well, particularly when examining materials that undergo phase transitions at $T = 0$ when small displacements are applied. This is particularly important for phonon calculations. Negative frequencies lead to imaginary phonon modes that lower systems energy this usually indicate the structure in its ground state is unstable with respect to a phonon mode when $\boldsymbol{q} = 0$ the phonon eigenvectors should go to zero as enforced by Acoustic sum rule which is clearly moving in a direction that breaks translational symmetry.

$$-\omega_\nu(\mathbf{q}) = i|\omega_\nu(\mathbf{q})| \tag{3.3}$$

For example, SnS in the Cmcm phase is unstable and has imaginary frequency modes due to the distortion of its structure, which usually indicates a small energy barrier between the phases of its symmetry.

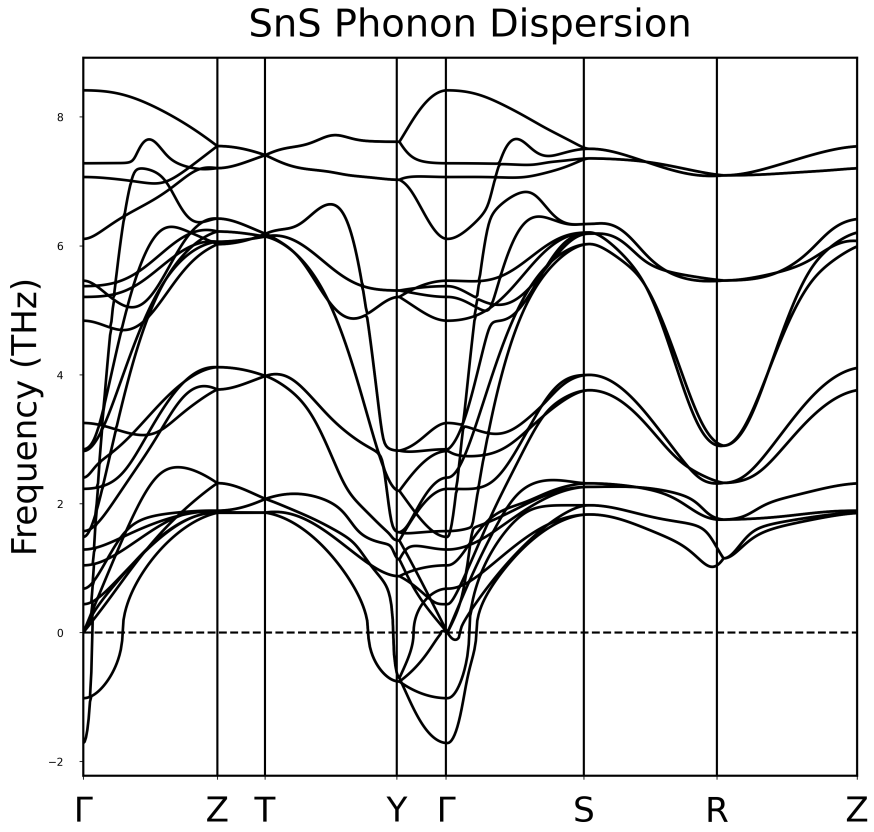

Figure 3.4: Phonon dispersion curves for the Cmcm phase of SnS calculated using the finite displacement method. The presence of imaginary frequencies (negative values) at the Γ point indicates that this phase is dynamically unstable.

CASTEP can natively do phonons either through DFPT or finite displacement.

The DFPT method relies on the key parameter $\frac{\partial n(\mathbf{r})}{\partial \lambda}$, the first-order density response. In general, the Wigner derivative follows the 2n+1 derivative of energy, which depends only on derivatives $\frac{\partial V(\mathbf{r})}{\partial \lambda}$ up to order n of the charge density[26].

$$\frac{\partial^2 E}{\partial \lambda^2} = \int \frac{\partial V(\mathbf{r})}{\partial \lambda} \frac{\partial n(\mathbf{r})}{\partial \lambda} d\mathbf{r} + \int n(\mathbf{r}) \frac{\partial^2 V(\mathbf{r})}{\partial \lambda^2} d\mathbf{r} \tag{3.4}$$

The finite displacement method is a numerical approach for calculating the Force Constant Matrix (FCM), in which an atom is displaced in both positive and negative directions, and the resulting force sets are evaluated The amplitude for a harmonic displacement is 0.01Å which can be changed depending on specific nature of the material such as those which possess strong anharmonic contribution.

$$\frac{dF_{\kappa,\alpha}}{du} \approx \frac{F^{+}_{\kappa,\alpha} - F^{-}_{\kappa,\alpha}}{2u} \tag{3.5}$$

These calculations computationally grow with system size, placing restrictions on what this method can achieve. DFPT only requires a primitive cell, whose dynamical matrix can then be interpolated onto a finer q-point grid, thereby reducing the need for large supercells for finite displacement. However, both finite displacement and DFPT phonon calculations require very fine geometry optimisations, with an approximate SCF electronic force tolerance of 0.001 eV/Å. While the finite displacement method only works at q = 0, the user has the freedom to choose which XC and pseudopotential, whereas DFPT can calculate responses to different q points $q \neq 0$. However, in CASTEP 25.11, the implementation of DFPT is for norm-conserving pseudopotentials only. The choice of the supercell size will depend on the force constant matrix, that decays with interatomic distance. The radius that encompasses the cell is chosen such that interactions are contained within a certain size supercell, given a cut-off radius, that is negligible for $r > R_c$. Interactions in the solid ultimately affect the range of FCM. Typical solids with high ionic character tend to have short-range effects, while those with low ionic character (more covalent) exhibit long-range interactions. The choice of the q-point grid needs to be sufficiently large to capture these effects in the FCM. This is handled by the fact that interatomic force constants are translated from one position to another, i.e there is no displacement or restoring force that the atoms feel. Leading to the following invariance sum rules, which apply to the force constant matrix and the Born effective charges.

$$\begin{aligned} \sum_{L,j} C_{\alpha i,\beta j}(\mathbf{R}_L) = 0 \quad \forall\, \alpha, \beta, i, \\ \sum_{j} Z^{*}_{j,\alpha\beta} = 0 \quad \forall\, \alpha, \beta. \end{aligned} \tag{3.6}$$

The first is the acoustic-sum rule, which ensures the dynamical matrix $C_{\alpha i,\beta j}(\mathbf{R}_L)$ where $\mathbf{R}_L$ is a lattice point in which translations are invariant, guaranteeing that translational symmetry is applied. The second sum rule guarantees charge neutrality, i.e the sum of the Born effective $Z^*_{j,\alpha\beta}$ charges of all atoms in one cell must vanish.

3.2.3 Molecular Dynamics

Consider a system of N interacting particles with time-dependent positions $\mathbf{r}_i(t)$ and velocities $\mathbf{v}_i(t)$. The interactions between these particles are governed by a multidimensional potential energy function, $U(\mathbf{r}_1, \mathbf{r}_2, \ldots, \mathbf{r}_N)$. Within the framework of the Born-Oppenheimer approximation, this function defines the potential energy surface (PES), which maps the total energy of the system for any given nuclear configuration. As the particles evolve dynamically and change their positions, the system moves across this surface, with the local gradients of the PES generating the forces that dictate their subsequent trajectories.

Classical Molecular Dynamics solves the classical equations of motion given by

$$\mathbf{F}_i = m\ddot{\mathbf{r}}(t) = -\nabla U(\mathbf{r}_1, \ldots, \mathbf{r}_n) \tag{3.7}$$

For a given set of coordinates evolving by discrete jumps of time where each interval δt is known as the timestep, and this represents the continuous trajectory propagating in time. Such an algorithm exists, known as the Verlet algorithm, which is widely used due to its computational efficiency in terms of memory.

$$r_i(t+\delta t) = 2r_i(t) - r_i(t-\delta t) + \frac{1}{m_i} f_i(t)\,\delta t^2 + O(\delta t^4) \tag{3.8}$$

The simplest approximation for the interatomic potential is of the form given by summation over all pairs of atoms i and j in configuration space.

$$U(r^N) = \frac{1}{2}\sum_{i=1}^{N}\sum_{j=1}^{N} U_{ij}(r_{rj}) \tag{3.9}$$

Since the exact potential energy surface (PES) is only found via direct minimization of the full quantum mechanical expectation value of electronic hamiltonian $\langle H \rangle$. We have seen that the exact form of the PES can be approximated with other force fields.

However, approximations are necessary for classical MD since it is impossible to determine the precise form of the PES in the system. To approximate the PES

one can make use of classical potentials

Which is commonly a two-body potential, which may for example be a Lennard-Jones potential. The highest cost is the evaluation of this potential, such as its derivatives $\nabla U(\mathbf{r}_1..r_n)$, to compute energy and give the forces, which are usually the largest part of the computation in an MD simulation.

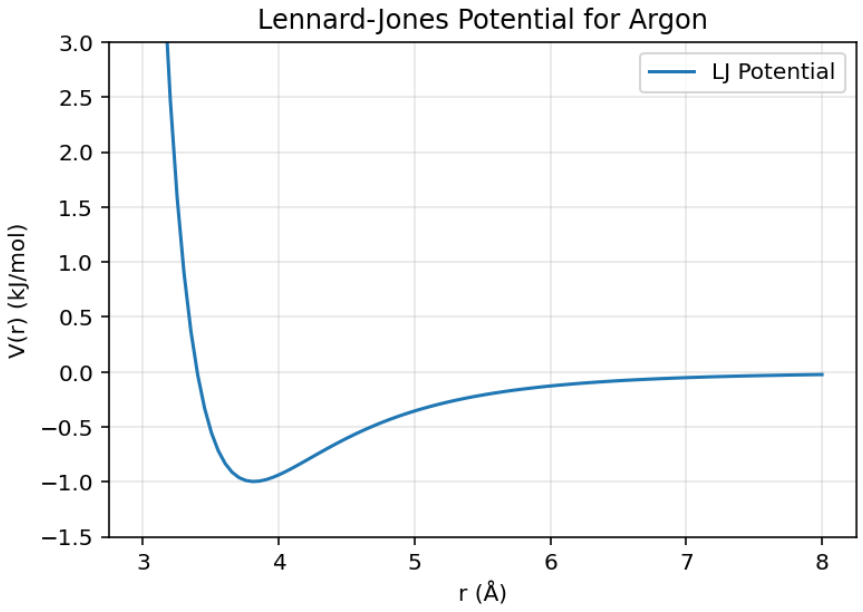

Figure 3.5: Classical 6/12 Lennard-Jones potential for argon.

Evaluating the derivatives of the potential energy to obtain the atomic forces naively requires calculating all pairwise interactions, resulting in a computational cost that scales as $\mathcal{O}(N^2)$. However, for most empirical interatomic potentials, the pairwise interactions decay rapidly and approach zero beyond a specific cut-off distance, r_{cut}. By truncating the potential at this distance, the computational cost is drastically reduced to $\mathcal{O}(N)$. This is because each atom only interacts with a finite number of neighbors defined by the cut-off distance, ensuring the number of interactions scales linearly with the total number of atoms N.

To execute these classical molecular dynamics (MD) simulations efficiently, we employ LAMMPS (Large-scale Atomic/Molecular Massively Parallel Simulator) [18]. Written in C++ and optimized for parallel computation via MPI, LAMMPS features a modular architecture that facilitates the implementation of custom potentials and features. While first-principles methods are typically restricted to systems of a few hundred to a hundred thousand atoms due to their steep computational scaling, classical MD codes like LAMMPS can easily handle systems containing billions of atoms. This linear scaling enables the study of large-scale bulk heterostructures and microstructural features, such as grains

ranging from nanometers to micrometers in size.

CASTEP supports both classical molecular dynamics (MD) and full *ab initio molecular dynamics* with Born–Oppenheimer molecular dynamics (BOMD), where the forces are calculated from the ground–state electronic configuration at each MD step. Within the CASTEP MD module, the NVE, NVT, NPH, and NPT ensembles are available. Temperature can be controlled using either a Nosé–Hoover thermostat or Langevin dynamics. If pressure effects are required, an Andersen–Hoover or Parrinello–Rahman barostat can be used. Simulations on high performance computing HPC systems are limited to $10^3 - 10^4$ atoms for most bulk systems.

3.3 TROM

Having established the workflow of obtaining phonons from a range of methods, TROM is a new Python-based code tool developed by Hossein Ehteshami at the University of York for enabling calculations of transport properties from MD via spectral energy density and mode decomposition methods to determine the phonon lifetime from MD. The theory implemented in the code has been established in chapter 2.

The workflow developed contains everything within this code; now, there are two systematic pathways a CASTEP user can take to calculate the lifetime and, hence, the thermal conductivity.

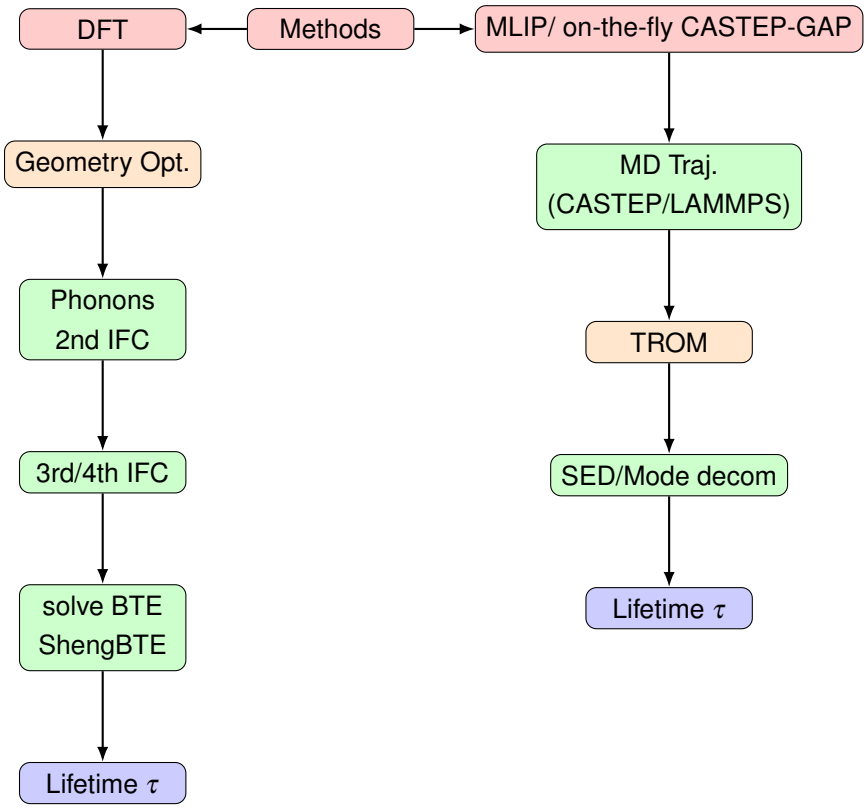

Figure 3.6: Two standard workflows for calculating phonon lifetimes using CASTEP DFT and MD with TROM.

The traditional perturbative approach requires high-order derivatives to compute the displacements from the 2nd order IFC, from which to get the third order and fourth order FCM to get three and four phonon scattering rates. It requires solving the Boltzmann transport equation for each of the probabilistic phonon-phonon scattering processes to give the lifetime. The alternative is first to find a suitable potential from GAP training and use it to accelerate the MD in CASTEP or directly in LAMMPS as a force field to compute the force constant

matrix. From this, TROM can compute the lifetime from the spectral energy density by measuring the width of the peaks or through mode decomposition.

3.4 Gaussian Approximation Potentials

GAP-based models[27] [28] [29] can offer up to a 100× speed-up over full AIMD. This substantial acceleration enables larger-scale simulations, while periodic DFT checks ensure the machine learning model remains accurate. This approach avoids a key limitation of empirical potentials, which require assumptions about the shape and form of the PES, for example, harmonic, Morse, or Lennard–Jones form. GAP can construct such a potential without having prior knowledge of the function, which is said to be unbiased.

Gaussian Approximation Potentials are the product of the application of the Gaussian process regression (GPR), where *ab initio* PES is sampled using DFT, such that GAP has some initial idea about the energy, forces and stresses.

The data are used to train the GAP model, which can be used to fit the energies and forces between the previously observed reference data points, where the resulting prediction can be used to generate MD trajectories, where the MD steps use an initial pre-trained dataset of MD–DFT configurations, with subsequent MD steps periodically validated against DFT calculations.

Gaussian process regression aims to evaluate the value of an unknown function $y(\mathbf{x})$, the value of which can be sampled at specific locations $\mathbf{x} = \{\mathbf{x}_i\}_{i=1}^{N}$, to give a set of known values $\mathbf{y} = \{y_i\}_{i=1}^{N}$ which make our training data set.

Using this training data set, Gaussian process regression aims to have a prediction of the function values $\tilde{y}(\mathbf{x}_0)$ at arbitrary points in the training space $\mathbf{x}_0$ we use the notation $\tilde{y}(\mathbf{x}_0)$ to indicate predicted values of the true function $y(\mathbf{x}_0)$).

Practically, for a system of interacting atoms, the points $\mathbf{x}$ represent the atomic configurations in phase space since the potential energy surface of an atomic system is sampled at measured function values y, which would be the total energies from a reference *ab initio* method.

In more detail, the approximate function is obtained by assuming that the target function $y(\mathbf{x})$ can be expressed as a weighted sum of M kernel (basis) functions k, each centred at a location $\mathbf{x}_m$ in the input domain:

$$\tilde{y}(\mathbf{x}) = \sum_{m=1}^{M} c_m k(\mathbf{x}, \mathbf{x}_m), \tag{3.10}$$

where $\tilde{y}(\mathbf{x})$ denotes the model prediction for the true function $y(\mathbf{x})$, and c_m are

the corresponding kernel weights.

The set of points $\{\mathbf{x}_m\}_{m=1}^{M}$ used in Eq. (3.10) does not have to coincide with the N training points $\{\mathbf{x}_n\}_{n=1}^{N}$. Typically, $M \ll N$, and this reduced collection is called the *sparse set* (or *active set / representative set*). Here, we leave the specific kernel form unspecified and instead focus on determining the unknown coefficient vector $\mathbf{c} = (c_1, c_2, \ldots, c_M)^\top$.

To evaluate how well a particular choice of $\mathbf{c}$ performs, we define a loss function l that measures the discrepancy between predicted values $\tilde{y}(\mathbf{x})$ and the corresponding reference values $y(\mathbf{x})$:

$$l = \sum_{n=1}^{N} \frac{[y_n - \tilde{y}(\mathbf{x}_n)]^2}{\sigma_n^2} + R, \tag{3.11}$$

where the positive parameters σ_n allow for different weighting of the training points. The first term enforces agreement with the training data, but if minimised without constraint, it can lead to overfitting.

To prevent overfitting and encourage smoothness, we introduce the regularisation term R:

$$R = \sum_{m,m'} c_m \, k(\mathbf{x}_m, \mathbf{x}'_{m'}) \, c_{m'}, \tag{3.12}$$

which penalises large values of $\mathbf{c}$. The parameters $\{\sigma_n\}$ can be tuned individually to prioritise fitting certain points more closely.

The loss function can be expressed compactly in matrix form:

$$l = (\mathbf{y} - K_{NM}\mathbf{c})^\top \Sigma^{-1} (\mathbf{y} - K_{NM}\mathbf{c}) + \mathbf{c}^\top K_{MM} \mathbf{c}, \tag{3.13}$$

where:

- $\mathbf{y} = (y_1, y_2, \ldots, y_N)^\top$ is the vector of training targets,
- $\mathbf{c} = (c_1, c_2, \ldots, c_M)^\top$ is the coefficient vector,
- $[K_{NM}]_{nm} = k(\mathbf{x}_n, \mathbf{x}_m)$ is the kernel matrix between training points and sparse points,
- K_{MM} is the kernel matrix among sparse points,
- Σ is a diagonal matrix with $\Sigma_{nn} = \sigma_n^2$.

Minimising l with respect to $\mathbf{c}$ gives:

$$\mathbf{c} = \left(K_{MM} + K_{MN}\Sigma^{-1}K_{NM}\right)^{-1} K_{MN}\Sigma^{-1}\mathbf{y}, \tag{3.14}$$

where symmetry of the kernel ensures $K_{NM}^{\top} = K_{MN}$.

Given the optimal weights, predictions at a new input $\mathbf{x}$ are computed as:

$$\tilde{y}(\mathbf{x}) = \mathbf{c}^{\top}\mathbf{k}(\mathbf{x}, \mathbf{x}_M), \tag{3.15}$$

where $\mathbf{k}(\mathbf{x}, \mathbf{x}_M)$ is the vector of kernel evaluations between $\mathbf{x}$ and the sparse set $\{\mathbf{x}_m\}_{m=1}^{M}$.

To provide some intuition of how the GPR processes are used to fit high-dimensional potential energy surfaces that depend on the positional coordinates of every particle in the system, consider looking at a 1D system, in this case, a cubic function.

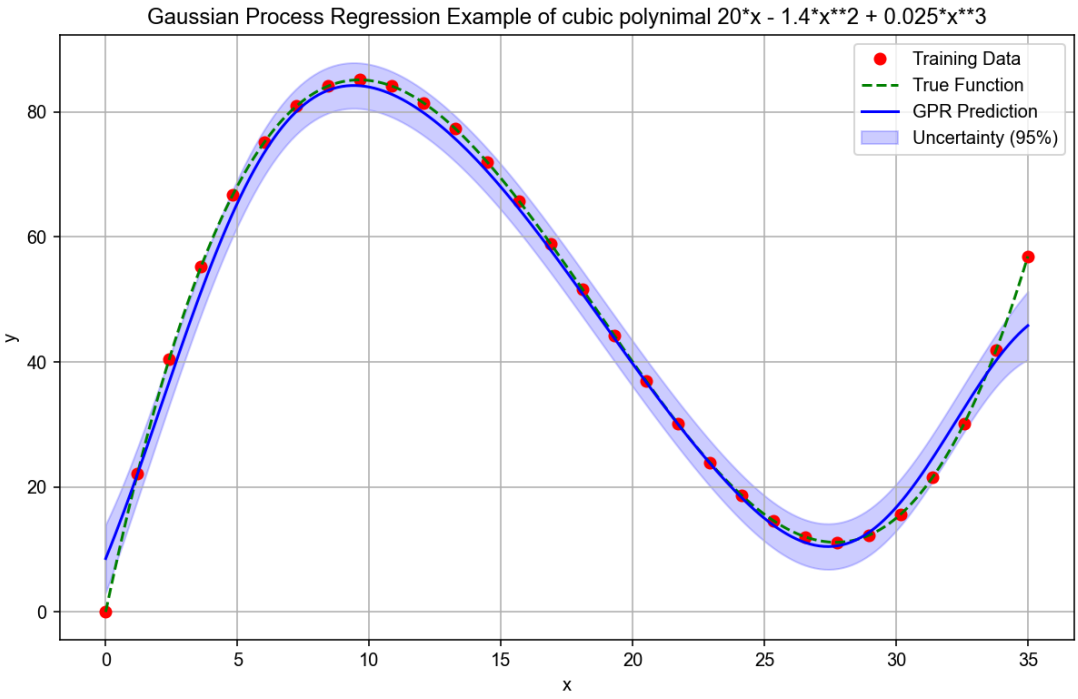

Figure 3.7: Interpolation and fitting of a cubic function through GPR process.

The data points are created using a polynomial $20x - 1.4x^2 + 0.025x^3$ and using the squared exponential kernel. This gives points with a similar value to the actual values of x, in which each point contributes a weight, and the target point will have a similar value of y to the point near it.

$$k(\mathbf{x}, \mathbf{x}_0) = \sigma_f^2 \exp\left(-\frac{(\mathbf{x} - \mathbf{x}_0)^2}{l^2}\right)$$

The function is essentially going through a regression, which repeats the process of predicting values for the target points, where interpolation of the function is performed through the least squares approach or the loss function. Here is a

sample of 100 points plotted, which is enclosed within the bounds of uncertainty error.

It's important that note that where there is are higher density of sampled points, GPR works very well; however sparser points, it tends to overshoot. The GPR process should be used as interpolation rather than extrapolation.

3.5 GAP training

Training an accurate GAP model requires optimising hyperparameters and descriptors to achieve a level of accuracy in energies and forces between the previously observed reference data points, which relies on how well the interpolation from the initial DFT to the initial fitting of points to the PES is performed.

A brief review of the most frequently used hyperparameters for fine-tuning GAP training is presented. The intricacies of all input GAP parameters can be found in detail in [30].

The first descriptor input is the interatomic distance, defined as

$$r_{ij} = |r_i - r_j| \tag{3.16}$$

Where r_j, r_i indicate the position of atoms i and j, where it simply describes the distance between atoms. Long-range interactions can create problems for ML potentials[31]; in this case, the simple descriptor takes relative particle positions into account that are within the cutoff radius known as the local environment.

Atoms outside the defined cutoff radius are neglected in the ML predictions of energy and forces. Different methods exist to try and incorporate this into ML potential. One way is to separate the many-body system interactions and the electrostatic contribution.

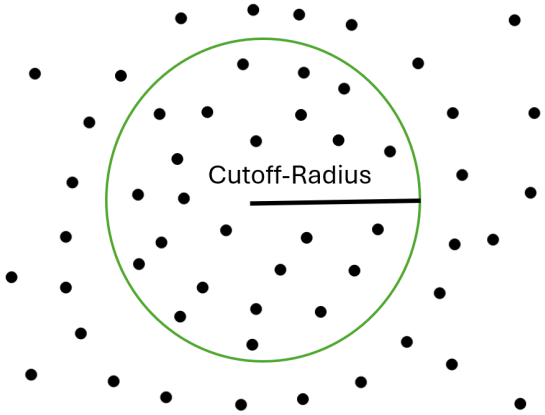

Figure 3.8: Description of cutoff radius in an atomic system.

The total energy of the system is simply represented by the sum over pairwise contributions

$$E = \sum_i \sum_{j>i} V^{(2b)}(r_{ij}) \tag{3.17}$$

where any change in the order of atoms affects just the summation, leaving the total energy unchanged. Here we have used a two-body description, which is simply the distance between two atoms. In principle, a variety of many-body ordered terms, i.e two-body (2B), three-body (3B), and higher-order (MB) terms, can be used.

While two-body (2B) descriptors effectively capture radial pairwise distances, they are rarely sufficient on their own because they lack many-body effects. Consequently, a combination of at least 2B and three-body (3B) terms is generally necessary to accurately capture most local atomic environments. Furthermore, it is important to recognize that long-range Coulombic and quantum exchange interactions cannot be fully accounted for simply by increasing the order of the many-body descriptors used in the Gaussian Approximation Potential (GAP) fit.

$$E = c^{(2b)} \sum_{i,j} V^{(2b)}\left(q_{ij}^{(2b)}\right) + c^{(3b)} \sum_{i,j,k} V^{(3b)}\left(q_{ijk}^{(3b)}\right) + c^{(MB)} \sum_{i} V^{(MB)}\left(q_{n}^{(MB)}\right). \tag{3.18}$$

The number of M representative points that make up the basis set of functions modelling the total atomic contributions from N total points. The choice of basis functions should be large enough to ensure that all of the pairwise interatomic interactions that must be represented in the training data.

An additional smooth overlap of atomic positions (SOAP) [32] descriptor is used in conjunction with the GAP descriptor, where additional hyperparameters

are worthy of discussion. Many-body interactions are described using SOAP descriptors. They are smooth overlap atomic positions, they primarily used for short and long-range electrostatics of a many-body system from a local point. For this descriptor, the radial and angular parts n_{max}, l_{max} form a basis for what is known as the neighbour density around an atom in its position i, which is constructed by a Gaussian function to describe the system. It is common to use different sizes n_{max}, l_{max} to maximise the interactions in the construction of the neighbour density. Where r_{ij} is the cutoff radius and σ is the width of the Gaussian, and f_{cut} is a function which varies smoothly to zero at the cutoff radius

$$\rho_i(\mathbf{r}) = \sum_j f_{\text{cut}}(r_{ij}) \exp\left[-\frac{\left(r_i^2 - r_{ij}^2\right)^2}{\sigma^2}\right]$$

This expansion is performed for neighbouring atoms j, with the basis truncated at integer values of n_{max} and l_{max}. This basis set becomes increasingly more complex with the addition of higher n_{max} and l_{max}, causing an increase in both the accuracy and the computational cost of the potential.

The final parameter is the exponent ζ, which is applied when computing the SOAP kernel function. A value of $\zeta = 1$ corresponds to a linear kernel; raising the SOAP dot-product kernel to higher powers increases the number of neighbouring interaction terms included. As ζ is increased, the effective body order of the interactions described by the SOAP descriptor is given by $2\zeta + 1$. Most published models use values of either $\zeta = 2$ or $\zeta = 4$; in the present LiF calculations, $\zeta = 4$ is employed.

The initial search was configured using SOAP descriptors with parameters $l_{\text{max}} = 6$, $n_{\text{max}} = 6$, $r_{\text{cut}} = 4.0$ Å, $\sigma_{\text{force}} = 0.01$ eV/Å, $\sigma_{\text{energy}} = 0.001$ eV, $\zeta = 4$, and $M = 4000$. This initial set was chosen based on trends in previous GAP training models [29], as it minimizes the error in energy and forces while balancing computational expense and accuracy.

The GAP models were trained using 2000 full AIMD timesteps from a $4 \times 4 \times 4$ supercell based on the primitive cell of two-atom LiF. The dataset was split into an 80:20 ratio for training on the GAP model and evaluating the model on a test set to predict the force, energy and virials. The same test set was evaluated with single-point DFT energy, and the RMSE was calculated.

The initial screening showed RMSE changed very little with n_{max} and l_{max}. In particular, the ~~lowest~~ initial $l_{\text{max}} = 6$, $n_{\text{max}} = 6$ was a good choice, as this also was found to be a little compromise of accuracy for computational expense. It was also found that very little change in the energy error occurred beyond

4000 sparse points, and very little gain was observed in accuracy and cost by increasing the number of sparse points beyond 4000.

When selecting sparse points via the CUR method for GAP fitting, the supercell dimensions must be large enough to fully encompass the descriptor's cutoff radius. If the cut-off is larger than the actual size of the supercell, it introduces self-mapping onto the atoms, and the errors rise dramatically.

Typically, the radius is increased to larger distances for very ionic systems than the usual radius for producing GAP models due to the need to capture long-range coulombic interactions. The primitive cell for LiF limits the number of neighbouring interactions within a given radius, therefore requires a large enough supercell from a primitive cell base than the conventional one would to overcome the long-range electrostatics.

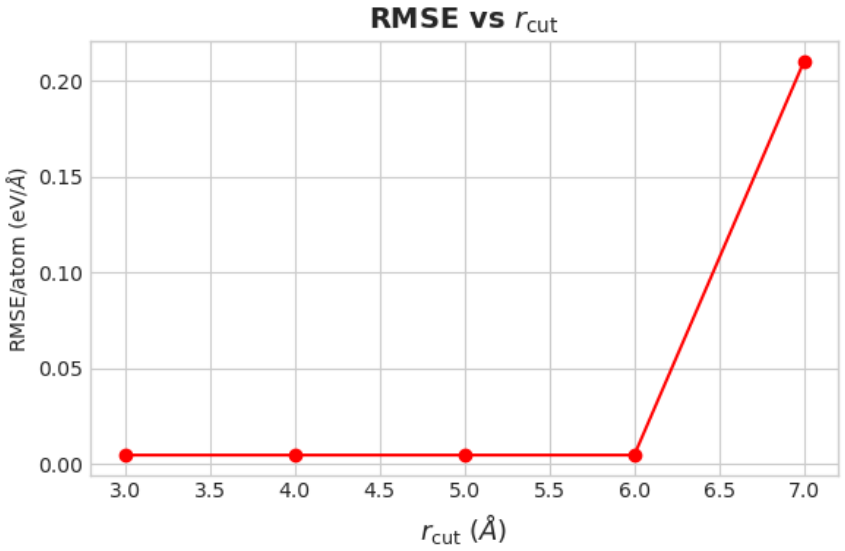

Figure 3.9: The effect of changing the cutoff radius on LiF for 4x4x4 supercell.

The computational cost of evaluating SOAP descriptors scales linearly with the total number of atoms, $\mathcal{O}(N_{\text{atoms}})$, as the descriptor relies strictly on local atomic environments within a cut-off radius r_{cut}. However, the computational cost to construct the local density expansion coefficients c_{nlm} for a single atom and the dimensionality of the final descriptor vector depend heavily on the hyperparameters n_{max} and l_{max}. Specifically, evaluating the spherical harmonics Y_{lm} required for the expansion coefficients scales as $\mathcal{O}(l_{\text{max}}^2)$, making the construction cost proportional to $\mathcal{O}(N_{\text{neigh}} n_{\text{max}} l_{\text{max}}^2)$. Furthermore, the final SOAP descriptor is represented by the power spectrum $p_{nn'l}$, whose total vector length scales as $\mathcal{O}(n_{\text{max}}^2 l_{\text{max}})$. Consequently, while SOAP evaluation remains linear with respect to overall system size, increasing the radial basis set size n_{max} rapidly inflates the dimensionality of the feature space quadratically, whereas

increasing the angular resolution l_{max} significantly raises the initial construction cost.

3.5.1 Hybrid MD

The training GAP model from MD is extremely costly in memory and puts huge limitations on what we can train on and how accurate our model is. The Hybrid-MD approach [33] combines GAP and DFT to deliver an on-the-fly GAP model and checks against DFT data, which delivers a dramatic acceleration in MD simulation time.

GAP uses the DFT forces to accelerate the MD dynamics; however, this can be affected by the number of factors. The overall speed can be strongly affected by system specifics. Anharmonic materials such as PbTe require more extensive training due to the number of electrons it must evaluate during DFT steps, which slows down the overall speed.

Whereas LiF is extremely harmonic and has fewer electrons required to evaluate at DFT steps. Although all ionic systems suffer from lack of long range Coulombic interactions. Li is fairly light and requires smaller MD time step which is more work for the MD dynamics to produce better quality GAP potential from this.

The on-the-fly GAP models with Hybrid-MD are especially valuable for systems that require many thousands of learning steps before equilibration with AIMD. Having the benefit of the acceleration as both system size and the number of time steps grow in size, the AIMD calculations grow in computational expense.

Initial DFT data is used to gain an idea of what the PES for LiF is, which GAP will use to approximate the full PES from a sampling of DFT data. The generation of each GAP potential occurs at each decision-making point after the DFT step evaluates the ML step based on how well the DFT data generalises with respect to the GAP prediction; it is either retained or needs refitting, based on tolerances set by the user.

This is very useful for both testing and time-saving because we can sample several potentials created from the run. The hope is that GAP, as it undergoes training, will improve after each step, as we would ideally like to sample potentials that model vibrational properties that are in the minima of the PES.

The table above shows how the Hybrid-MD can accelerate the MD for a large system (eg 4x4x4 supercell) with a small cluster. Typically, doing around 10 thousand time steps with 2 fs trajectory. For the given time is shown to dramatically speed up the MD on 4x4x4 supercells. Usually, with Hybrid-MD on, you

species	DFT-MD time	ML time
LiF	3 days	18hr
PbTe	$\approx$ 4 weeks	4 days

Table 3.1: Time taken with ML and without on the Viking cluster

need a few initial DFT-MD steps for training and around 10 ML steps for every DFT step (hence 10x speedup) for very loose tolerances on forces, strain and energy. Once the tolerances are made tighter, the Hybrid-MD will struggle to reach such tolerances without some additional help from the SOAP and GAP descriptors.

The Hybrid-MD trains the GAP.xml model from the last final MD configuration; there is very little computational expense compared to the full GAP training. The gain in this means typical calculations with larger SOAP and GAP are possible with the caveat that these are essentially sampled from a specific trajectory in phase space.

To develop a GAP potential for vibrational properties, the training sets consist of a large subsample of configurations developed during the Hybrid-MD runs with the lowest energy and force configurations. Plotting the DFT and predicted energy and forces shows how well the dataset we have chosen generalises, since the GAP potential for a single configuration will evidently lead to over-fitting. However, larger subsampling of diverse data helps to prevent overfitting.

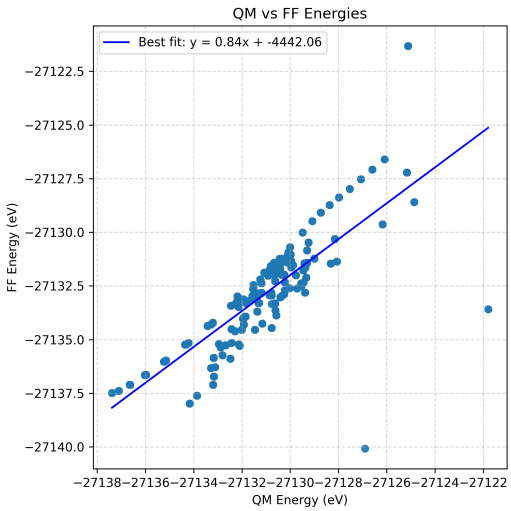

Figure 3.10: QM vs FF Energies for LiF

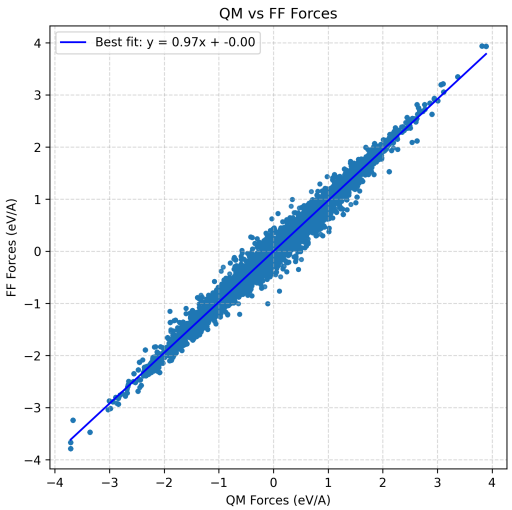

Figure 3.11: QM vs FF Forces for LiF

Table 3.2: Optimised hyperparameters used in training GAP and SOAP descriptors.

Atomic environment parameter	**SOAP**	**GAP 2B Term**
r_{cut} (Å)	4.5	4.5
d (Å)	1.0	–
σ_v^{energy} (eV/atom)	0.001	0.001
σ_v^{force}	0.1× (force on each atom)	0.1× (force on each atom)
ξ	4	–
δ (eV)	3.0	3.0
σ_{atom} (Å)	0.5	–
n_{max}	12	–
l_{max}	6	–
Representative environments	4000	30
Sparse jitter	–	1.0×10^{-8}
e_0 (reference atomic energies)	F: -644.119387 eV,	Li: -196.0751627 eV

Chapter 4

Computing Properties of PbTe and LiF

4.1 Background

Lithium fluoride adopts the rock-salt (NaCl) structure, with each Li cation octahedrally coordinated by six F anions. In the unit cell, the arbitrary positions in the cell are placed at fractional coordinates centred on Li at (0,0,0) and F at (1/2,1/2,1/2). LiF is a well-known insulator and is used in many applications. The thermal conductivity of many materials can be enhanced by adding Li to it due to the presence of Li, as at high temperature the Li ion can freely move which can enhance thermal conductivity, for example its use in nuclear fuel coolant. In PbTe, the crystal is analogous to LiF. However it is the opposite, being a semiconductor with a small band gap, having a very anharmonic ground state PES, which is thought to be the mechanism of its thermoelectric properties and makes this also a very hard but interesting case for DFT/MD methods.

4.2 Density functional theory calculations

First-principles calculations were conducted using the CASTEP 25.11 software on PbTe where The ground-state was found for PbTe using the conventional cell, see figure 4.1, using a cut-off energy of 750eV. The Brillouin zone was sampled using a Monkhorst-Pack grid with a mesh of 8 × 8 × 8 k-points with the GGA PBE exchange-correlation functional and norm-conserving pseudopotentials (NCP) were employed.

The self-consistent field (SCF) were carried out with tighter parameters to ensure ground state density used in the phonon calculations are properly converged where the geom energy and electronic energy tolerance was set to $1 \times 10^{-6} eV$ and $1 \times 10^{-10} eV$, fine grid scale to 4.

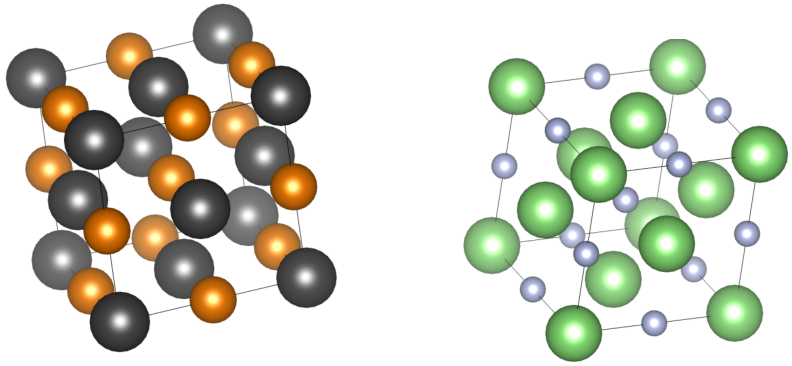

(a) PbTe (b) LiF

Figure 4.1: Comparison of structures: (a) PbTe and (b) LiF.

Spin-orbit coupling was included in the geometry optimisation for the purpose of optimizing PbTe lattice parameters and DOS and band structure dispersion but not used for the purpose getting Phonons dispersion.

Table 4.1: Lattice constant a of PbTe and LiF obtained from experiment [2], PBE calculated, and literature results [3].

Material	$a_{\mathbf{exp}}$ (Å)	$a_{\mathbf{calc}}^{\mathbf{PBE}}$ (Å)	$a_{\mathbf{lit}}^{\mathbf{PBE}}$ (Å)
PbTe	6.420	6.415	6.565
LiF	4.027	4.066	4.103

Similarly, for LiF simulations, calculations were performed using PBE with on-the-fly pseudopotentials (NCP), employing a plane-wave cutoff energy of 800 eV. The Brillouin zone was sampled with an 8x8x8 k-point grid using a Monkhorst-Pack scheme, having sufficient convergence.

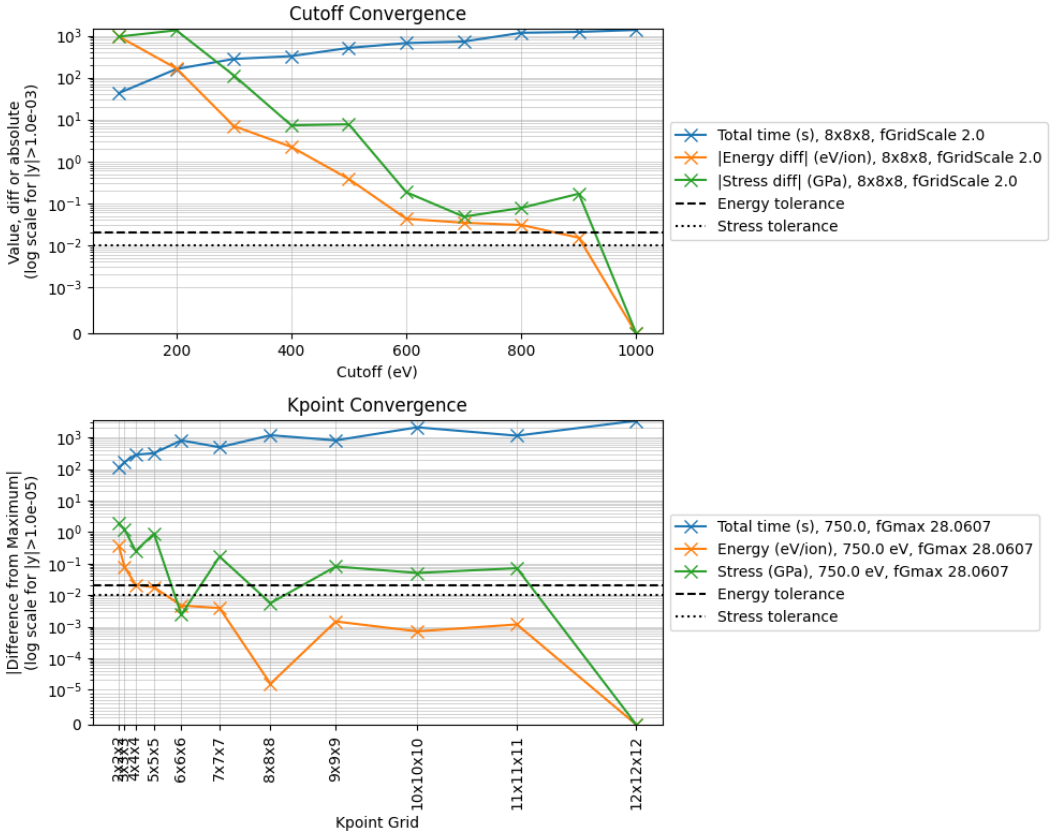

Figure 4.2: PbTe convergence tests of k-points and cutoff energy

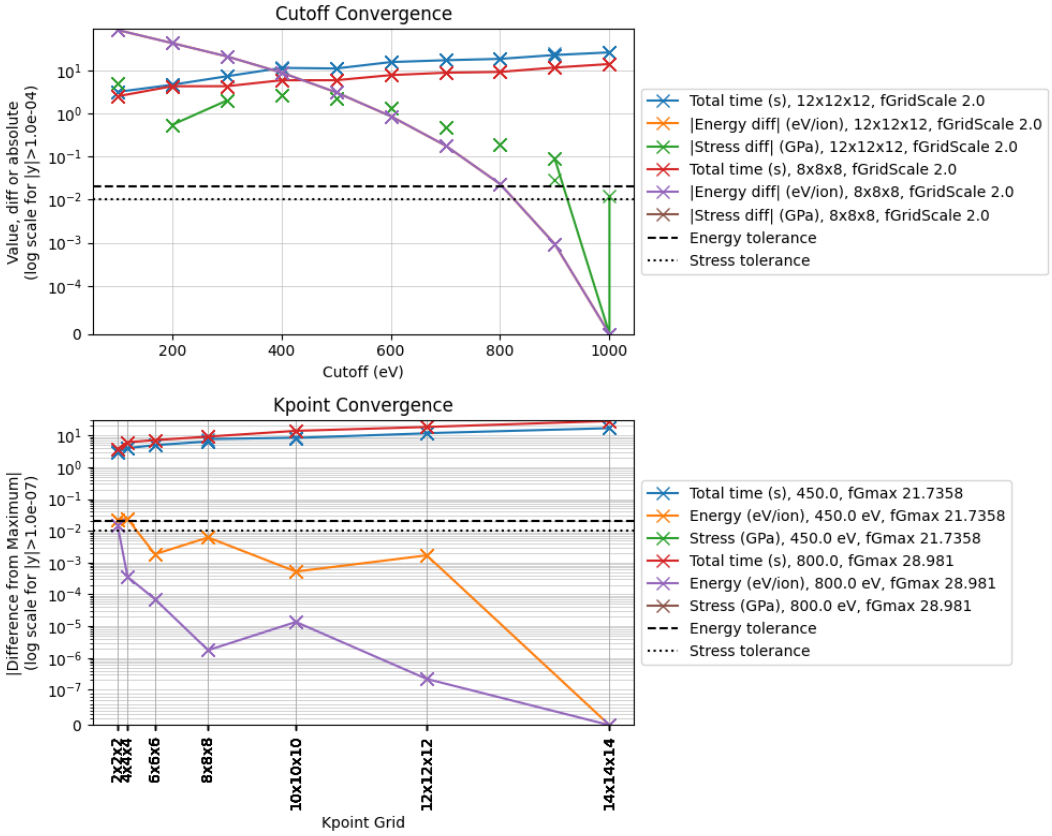

Figure 4.3: LiF convergence tests of k-points and cutoff energy

4.3 Electronic structure

Consider the Kohn-Sham single-particle equation in its most simplistic form, which consists of two parts: a kinetic and a potential energy operator multiplying the plane wave $\psi_{nk} = e^{ikx}u(\boldsymbol{r})$ and taking use of the product rule will give the following equation. The purpose of the band structure is to visualise how the Kohn-Sham eigenstates of occupied and unoccupied energy states localise across the BZ.

$$\left[-\frac{1}{2}(\nabla + ik)^2 + V_{tot}\right] u(\boldsymbol{r}) = \varepsilon u(\boldsymbol{r}) \tag{4.1}$$

By taking the two extremes, we consider either just the potential energy or just the kinetic energy. To evaluate the total energy is simply the expectation value $\langle\Psi|\hat{H}|\Psi\rangle$. In the free electron limit, you're left with $-\frac{1}{2}(\nabla + ik)^2$ with quadratic energy curved bands. Electrons bound to $V(\boldsymbol{r})$, with no kinetic energy, are bound to the potential which results in flat bands. The lowest energy states have flat bands as inner valence orbital states are bound strongly due to a greater effective nuclear charge.

Lead telluride is a narrow-gap semiconductor (bandgap 0.3 eV), where LiF has a bandgap of 8.8 eV, indicating its insulating properties.

The valence band maximum of LiF is solely occupied by F p-orbital electrons, and a clear, distinct separation of bands indicates no hybridisation between F and Li orbitals, indicating flat bands are due to its strong ionic character. The conduction band is mainly distributed with Li orbitals.

PbTe valence states belong to the 5s and 6p orbitals. In contrast, PbTe contains far more electrons with larger p and s orbitals, which have been shielded by an effective inner electron-electron screening, resulting in electrons being far more delocalized, leading to the curved bands, which have some kinetic energy. The Density of States (DOS) tells us the weighting for each energy interval E to $E + dE$

$$\rho(E) = \sum_i \int_{\mathrm{BZ}} d\mathbf{k}\, \Omega\, \delta(E - \varepsilon_{i\mathbf{k}})\,. \tag{4.2}$$

For LiF, the sharp peaks around -40 and -20 eV are due to F and Li s and p states, which are tightly bound. For LiF, the main contribution of energy around the Fermi level comes from the Li, which has p orbital character and a single small peak for the F p state. For PbTe, the peak just below -10eV corresponds to the Te s state and just before corresponds to the Pb s orbital state. Moving up in energy, the Te p states are most prominent starting from 5eV.

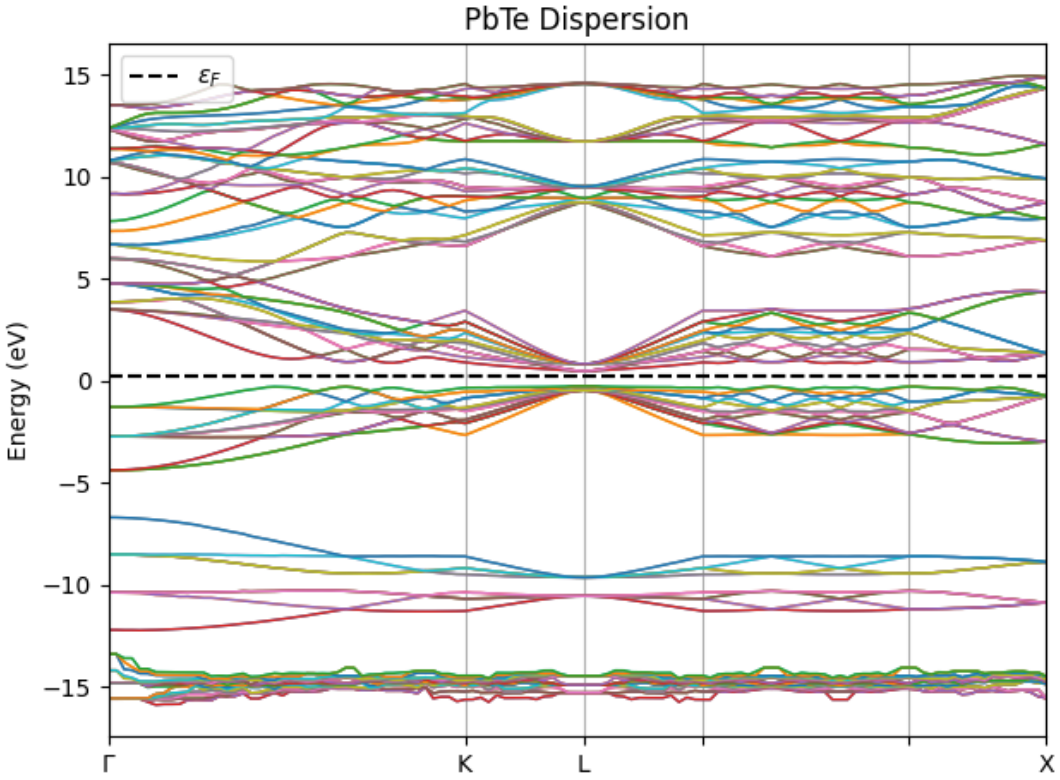

Figure 4.4: Electronic band dispersion of PbTe.

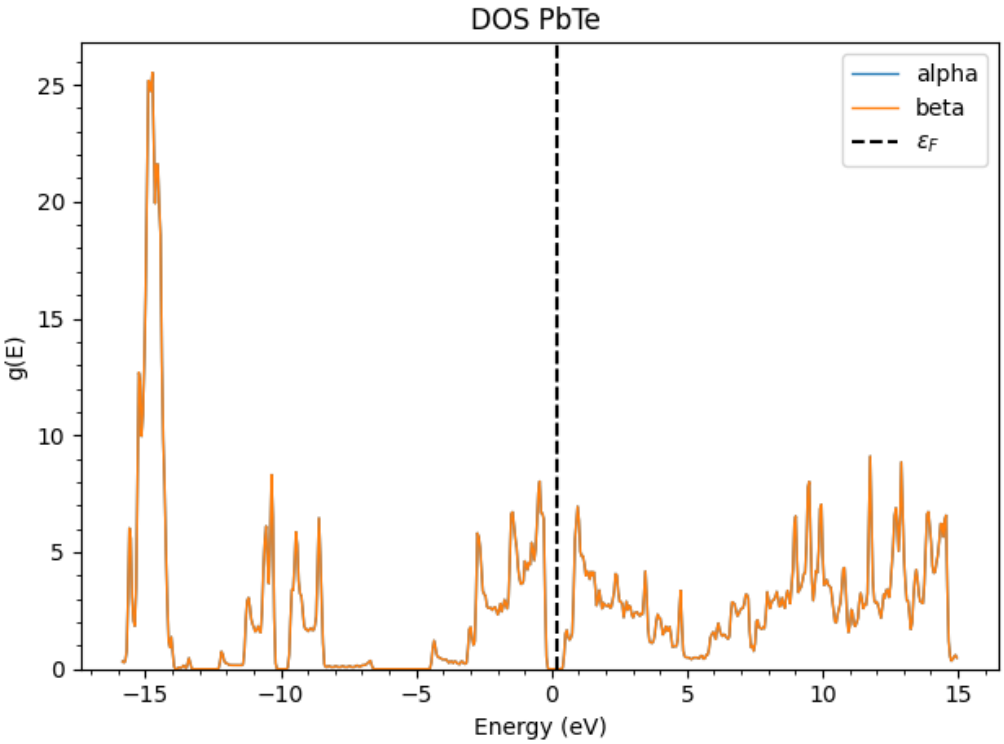

Figure 4.5: Electronic density of states (DOS) of PbTe.

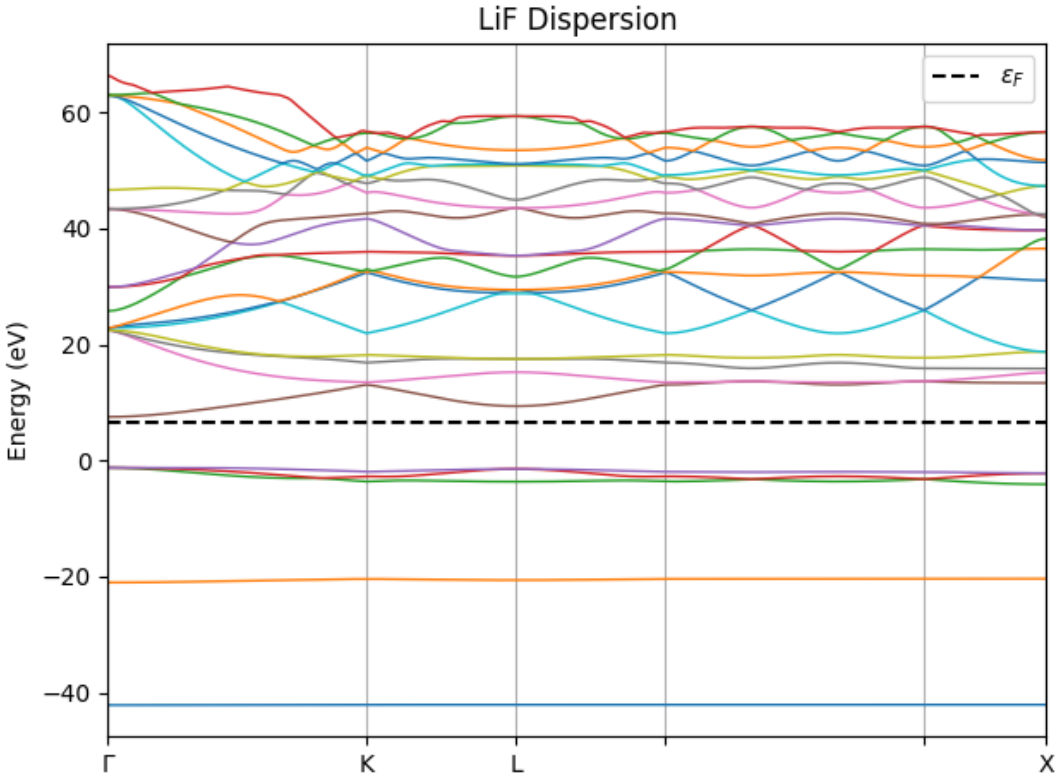

Figure 4.6: Electronic band dispersion of LiF.

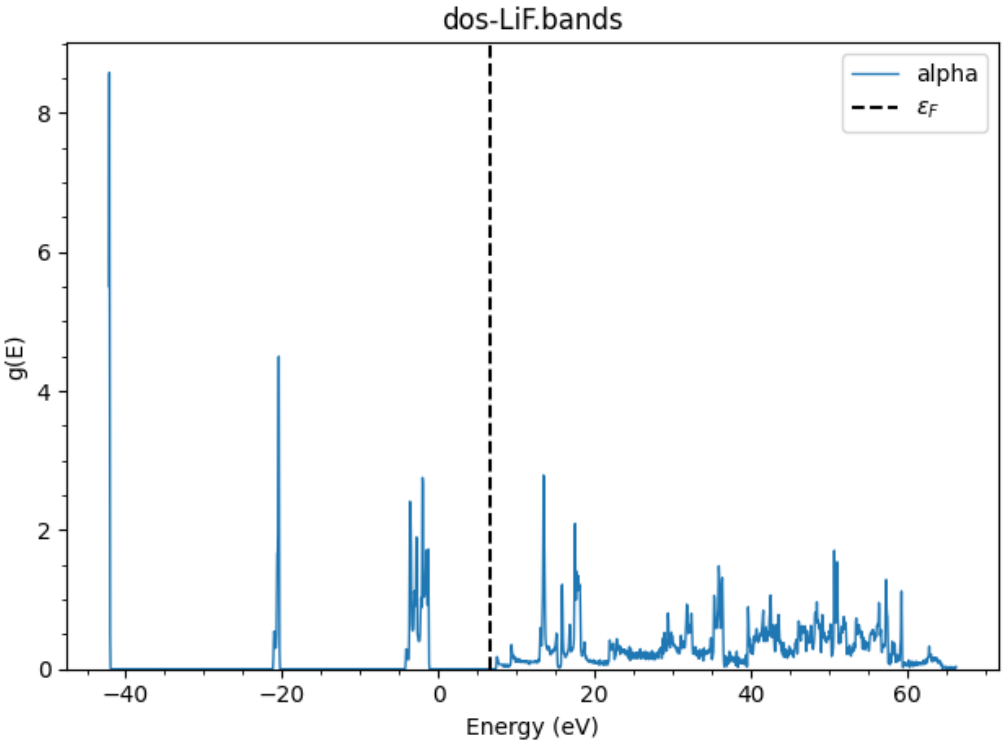

Figure 4.7: Electronic density of states (DOS) of LiF.

4.4 Phonon properties

For LiF we have used the same procedure as with the electronic band structure. Density functional perturbation theory (DFPT) is used to calculate the phonons of the LiF conventional cell over the high symmetry points in the Brillouin zone using 4x4x4 q-point mesh to sample.

LiF is a polar material and an insulator. Therefore the induced dipole moment will shift the optical phonon modes due to long-range Coulomb interactions. This polarisation effect results in an additional restoring force between the ions, yielding a higher longitudinal phonon frequency compared to the transverse optical phonon; therefore, it was essential to introduce LO/TO splitting. We choose to apply an electric field in order to calculate the Born effective charges needed for the corresponding non-analytical term in the force constant matrix.

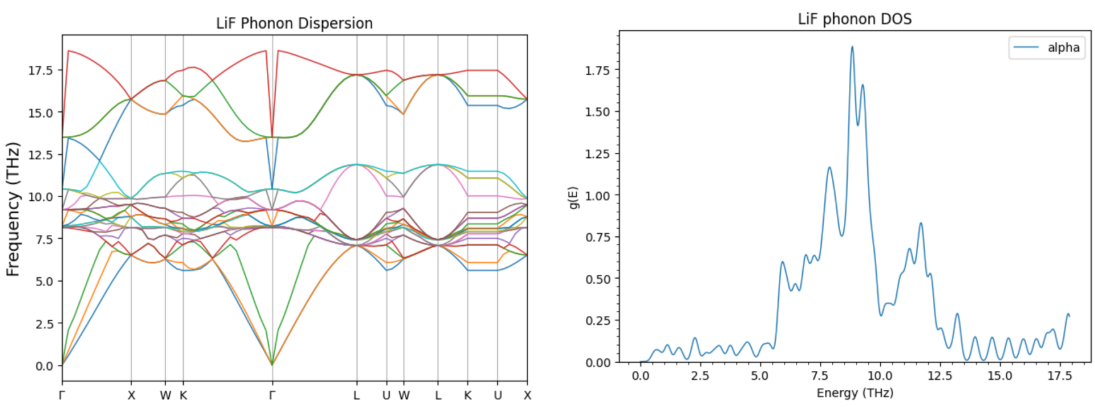

(a) Phonon dispersion (b) Phonon density of states (DOS)

Figure 4.8: Phonon properties of LiF: (a) dispersion and (b) density of states.

The conventional cell is composed of N atoms, of which there are 8, and a total of 3N phonon modes consists of three acoustic modes: one longitudinal and two transverse, and 3N-3 modes which are optical phonon modes. Hence the phonon dispersion will have 24 phonon modes in total, arising from 3 acoustic modes and 21 optical modes. The displacement vectors can be plotted to show 3N vibrational modes for solid LiF.

Here in figure 4.8 shows the acoustic and optical vibrational modes as vectors. LiF has the highest maximum phonon frequency at 17 THz as LiF possesses strong ionic short bonds, lighter atomic weight, and a more rigid lattice structure leading sharp rise of the bands from Γ.

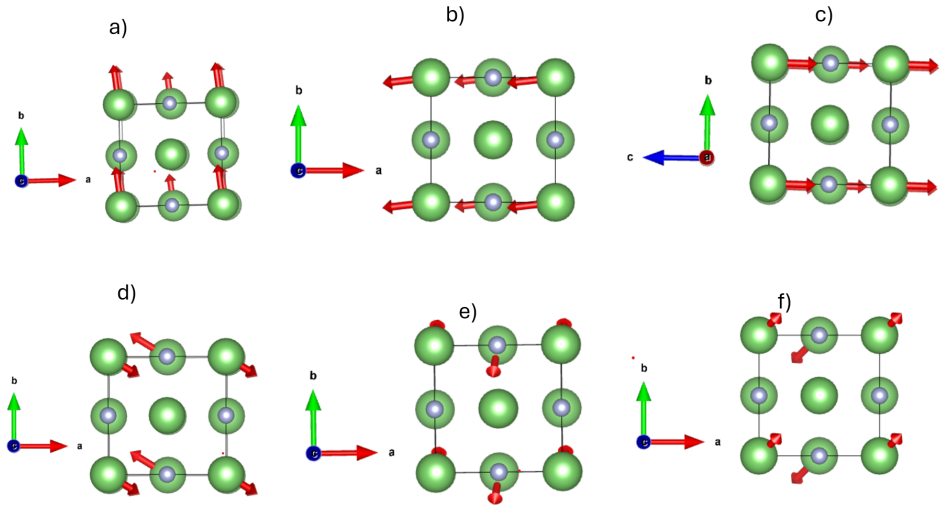

Figure 4.9: Phonon displacement vectors at Γ point.

The PES can be described by a parabola, if the system is harmonic or weakly anharmonic with small deviations about the parabola. The harmonic approximation is a good enough approximation to justify using density functional perturbation theory (DFPT) instead of finite differences as with LiF. For PbTe, extracting vibrational properties proves much more complex as the mode-dependent anharmonicity within PbTe has a very large contribution. By plotting phonon eigenvector displacement vs energy, as shown in figure 4.10 for the LO mode (which has the largest anharmonic contribution to the PES) [34] the large anharmonicity of PbTe is clearly demonstrated, and the standard harmonic approximation starts to break down. DFPT is formally limited to second-order force constants and struggles with non-perturbative, temperature-driven anharmonicity. To overcome these limitations, the forces arising from the anharmonicity are calculated best from finite displacements since the advantage of this method is to investigate phonon anharmonicity as the amplitude of the displacements is increased. For PbTe we chose a minimum displacement of 0.05 Å

The right-hand sub figure illustrates the specific mode displacement along a given phonon eigenvector; displacing the atoms along this eigenvector allows us to map the potential energy as a function of displacement amplitude.

Spin-orbit coupling was included in the geometry optimisation and spectral properties such as the DOS and band structure in PbTe, but not in any of the Phonon calculations via DFPT, due to the absence of SOC19 pseudopotentials. The lack of spin-orbit coupling. Although through finite differences, we can calculate the phonon dispersion. There is a substantial cost in doing it through

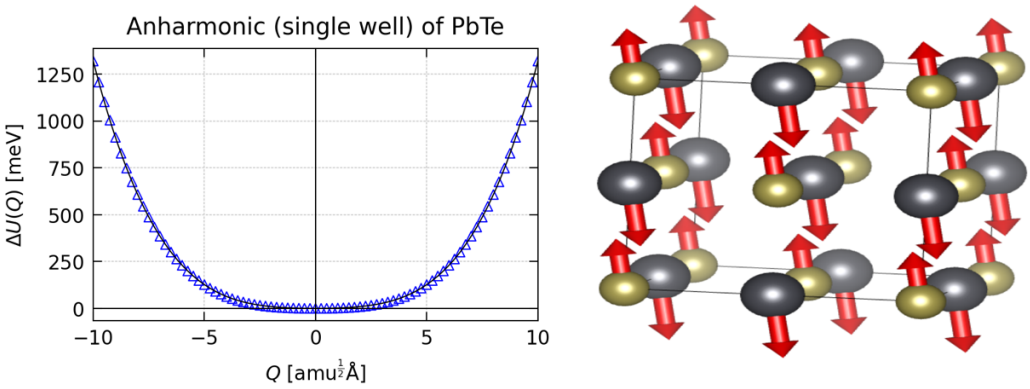

Figure 4.10: Plotting energy vs displacement along the LO mode of PbTe.

finite displacement, as an atom of Te requires 6 states, and each atom of Pb, 14 and with 4 of each in your baseline cell, which makes 80 electrons. Using a non-collinear magnetic treatment requiring 4 states per electron, so you are starting at 320 and making a 4x4x4 supercell, makes the calculation of PbTe very expensive. Although feasible with a conventional cell, the primitive cell would be a better choice if cost were the main concern. In the PbTe phonon dispersion of the conventional cell, you can see the largest spike around 3-4 THz corresponds to Pb moving down the second peak, which comes from the Te and Pb, which slightly decays corresponding to higher frequency optical modes where whereas Te has lower acoustic modes around 0-2THz

In the finite displacement method, the maximum reliable atomic displacement is limited by the force error when using finite-difference approximation. Because the extraction of accurate phonon frequencies relies entirely on the precision of the calculated interatomic forces, it is essential to employ exceptionally tight convergence criteria to minimize numerical noise in the forces.

The computational cost of these finite displacement calculations scales heavily with the number of explicit valence electrons, which is strictly dictated by the choice of pseudopotentials. Different pseudopotentials treat different electronic shells as core versus valence states. For example, using pseudopotentials that explicitly treat the core *d*-states as valence results in 14 valence electrons for Pb and 6 for Te. In an 8-atom primitive cell (4 Pb and 4 Te), this specific pseudopotential choice yields 80 explicit valence electrons.

Furthermore, the number of Kohn-Sham states (bands) required to accommodate these electrons depends heavily on spin-orbit coupling (SOC). SOC has a negligible effect on the vibrational properties of PbTe and is left out to reduce computational cost. Each band can hold two electrons, meaning the 80 electrons

require a minimum of 40 occupied bands, whereas in a non-collinear calculation (required for SOC), each band is a can only hold a maximum of one electron, thereby requiring a minimum of 80 occupied bands.

When expanded to a $4 \times 4 \times 4$ supercell (512 atoms), the system contains 5,120 valence electrons. Consequently, the calculation must solve for at least 5,120 non-collinear bands (or 2,560 collinear bands), alongside additional empty bands required for self-consistency. This results in a massive computational expense compared to standard harmonic DFPT.

This makes the calculation of PbTe expensive. Although feasible with a conventional cell, the primitive cell would be a better choice if cost were the main concern. Here, we have avoided using spin orbit coupling effects and used NCP pseudopotentials over 2x2x2 q point mesh.

In the PbTe phonon dispersion 4.11a you can see the largest spike around 3-4 THz corresponds to Pb moving down the second peak, which comes from the Te and Pb, which slightly decays corresponding to higher frequency optical modes whereas Te has lower acoustic modes around 0-2THz.

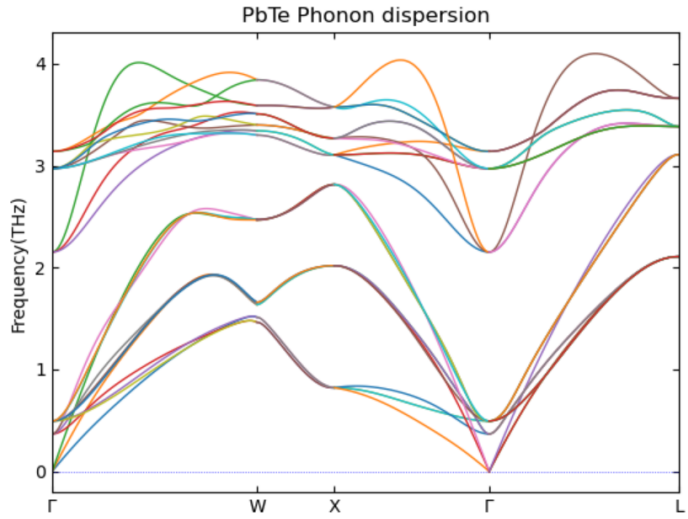

(a) Phonon dispersion

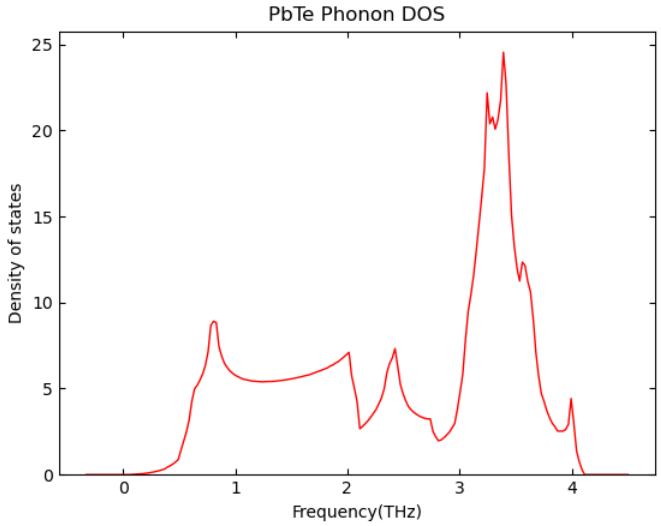

(b) Phonon DOS

Figure 4.11: Phonon properties of PbTe: (a) phonon dispersion and (b) phonon density of states (DOS).

4.5 Anharmonicity Measure

The anharmonicity is quantified using atomic forces because they provide direct insight into the local interactions experienced by individual atoms. Furthermore, from a statistical perspective, evaluating the total force vector $\boldsymbol{F}$ for a given atomic configuration $\boldsymbol{R}$ is more robust than analysing the $3N$ individual Cartesian force components, $\boldsymbol{F} = (\boldsymbol{F}_1, \ldots, \boldsymbol{F}_N)$.

The anharmonicity measure [20] is the ratio of the variance of anharmonic and harmonic force components. A larger deviation of the ratio with respect to the harmonic regime of the exact DFT PES shows a greater anharmonic contribution. The DFT forces are exact and, by construction, computing the F^{harm} is simple by taking the displacement vectors and the FCM.

$$F^{harm} = -\Phi_{\mathrm{ij}}\Delta R \tag{4.3}$$

The basic harmonic model is constructed through estimation of the $T = 0$ force constant matrix with randomly generated displacements ΔR, which are based on a population of phonon modes according to Boltzmann statistics for a given temperature.

In section 2.7 we explained that by purposely truncating to 2nd order (harmonic regime) we are assuming deviations from PES does not contribute to the lattice dynamics.

The effect of anharmonicity on the PES is better explained through Figure 4.9. fitting higher order polynomials in this case a quadratic and quartic polynomials are fitted to the exact PES from DFT data. The quartic fitting is far more agreeable than from a simple parabola (harmonic regime) fitting. The greater deviation from the harmonic picture, the larger the anharmonic contribution will be.

$$\Delta R_I^{\alpha} = \frac{1}{\sqrt{M_I}} \sum_s \zeta_s \langle A_s \rangle \, e_{sI}^{\alpha}, \tag{21}$$

where e_{sI}^{α} are the harmonic eigenvectors, $\langle A_s \rangle = \sqrt{2k_BT/\omega_s}$ is the mean mode amplitude in the classical limit and ζ_s is a normally distributed Random number. The anharmonic forces are simply equal to $F^{harm} - F^{DFT} = F^{anharmonic}$ and by taking the ratio of variance of $F^{anharm} : F^{harmonic}$

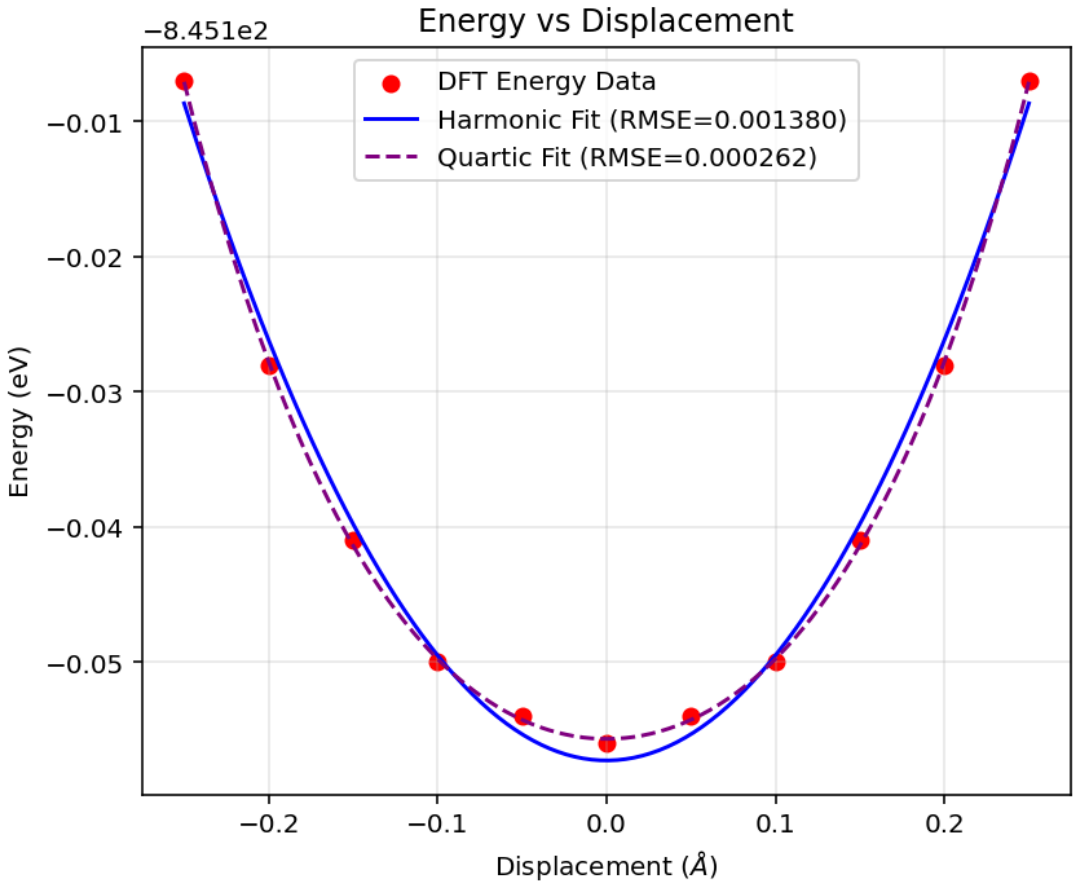

Figure 4.12: The quartic polynomial Root mean square error (RMSE) is less than the quadratic polynomial RMSE, showing that anharmonic fitting is a more suitable approximation to PES of PbTe.

$$\sigma^{\mathrm{A}}(T) \equiv \frac{\sigma\left[F^{\mathrm{A}}\right]_T}{\sigma\left[F^{\mathrm{DFT}}\right]_T} = \sqrt{\frac{\sum_{I,\alpha}\left\langle\left(F^{\mathrm{A}}_{I,\alpha}\right)^2\right\rangle_T}{\sum_{I,\alpha}\left\langle\left(F^{\mathrm{DFT}}_{I,\alpha}\right)^2\right\rangle_T}}\,, \tag{4.4}$$

Certain phonon modes will exhibit degrees of varying anharmonicity at each step. Bounded between 0 for a purely harmonic system and 1 for a fully anharmonic limit, this anharmonicity metric yields a maximum value of 0.26 for PBE-LiF at 300 K, indicating that anharmonic contributions account for approximately 26 percent of atomic forces at that timestep. The anharmonicity should be convergent as the system equilibrates. Larger spikes are due to the thermal fluctuations, creating large displacement amplitudes as the anharmonicity measure is dependent on temperature.

The anharmonicity is also dependent on temperature. We have shown that LiF is not particularly anharmonic at 300K. While most materials possess some anharmonic properties, LiF shows particular resilience to increasing temperature

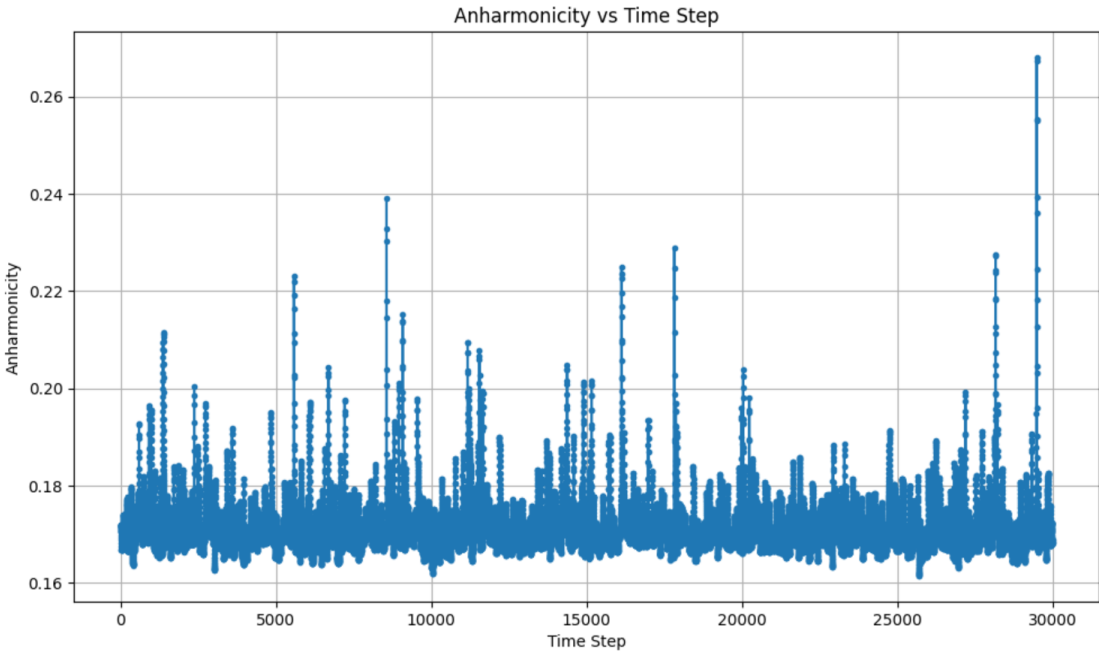

Figure 4.13: LiF is considered harmonic as the largest anharmonic spike does not go beyond 0.26; for reference, silicon has an MD maximum spike around 0.80.

and still has very low anharmonic contribution.

4.6 LiF Phonons from MD using Kong Method

4.6.1 DFT-based molecular dynamics

For the use of getting phonons from MD it is equally important to study systems of two extremes, where LiF is a polar material, and very few analytical corrections have been made to account for LO/TO splitting from MD and proves a real challenge for long-range electrostatics with MLIP. In contrast, the anharmonic interactions are strong in PbTe and in the limit of MD calculations, it's unknown how FCM will correctly contain all the correct anharmonic effects, whereas LiF has quite a weak anharmonic contribution. The relative differences in anharmonicity make these materials an ideal choice for comparative studies of phonons.

LiF MD simulations were performed on a 4x4x4 supercell made up of the primitive cell (128 atoms), and calculations were run plane wave cutoff energy of 800 eV using the PBE XC functional. An NVT ensemble was simulated with 1 fs over 30,000 timesteps to get good dynamics.

4.6.2 Finite Temperature Phonons

At finite temperature, the atoms are in motion and are displaced from their equilibrium positions. The FCM at $T = 0$ do not contract a good approximation to estimate the actual finite temperature FCM that arises from thermal fluctuations because the potential energy surface sampled at T is no longer purely harmonic.

The quasi-harmonic approximation neglects this explicit temperature dependence: the $T = 0$ force constants are retained, and at a finite temperature T it occupies the modes with a Boltzmann weight and does not change the mode frequencies. However, QHA captures thermal expansion but not phonon renormalisation.

For computing the phonons at finite temperature, the training data must contain a dense sampling of the region of phase space around the energy minimum for any crystal structures for which you would like to make a calculation.

To study phonon dynamics and their lifetimes requires a careful choice of thermostat, equilibration, number of timesteps and supercell size.

Typically, in finite-temperature properties of the system studied, the temperature must be set and controlled. The choice of NVT and NVE ensembles to thermalise and relax the structure was used to create a suitable training set. The

Nose-Hoover thermostat models the most realistic fluctuations of particles for a given temperature by effectively exchanging energy to and from the external bath coupled to it, such that the energy transferred to the system is equivalent to the average thermal energy k_BT. For the given equation of motion [35]

$$m\ddot{\mathbf{r}}(t) = -\nabla U(\mathbf{r}_1, \ldots, \mathbf{r}_i) - m\ddot{\lambda}\dot{r}_i \tag{4.5}$$

An extra term known as the coupling term controls the amount of energy exchanged with the system.

$$\dot{\lambda} = \frac{d\lambda(t)}{dt} = \frac{1}{Q}\left[\sum_{i=1}^{N}\frac{m_i v_i^2}{2} - \frac{(3N+1)}{2}k_BT\right]$$

Where $q$is the mass parameter which controls the timescale to which the exchange happens with the system with 3N+1 particles, where an extra +1 term is introduced to account for the extra degree of freedom given by the coupling term. At equilibrium, the difference in energy exchange tends towards zero.

In contrast to the Taylor series expansion defined at their equilibrium positions through DFT, MD has no well-defined initial equilibrium. Hence, the equilibration point is not known, and the equilibration period must be found initially. Unphysical phonon modes will arise for a timestep that is too large, e.g the atomic displacements are too large to get phonons accurately. In particular, the additional effect of supercell size and trajectory sampling has a great effect on the quality of phonons sampled from the trajectory.

Typical AIMD time steps are 1 - 2 fs. Due to the low mass of Li, a smaller time step of 0.5 fs was used in LiF MD simulations to stop drift in high-frequency optical phonon modes.

4.6.3 Sampling

The sampling rate must be high enough to capture the maximum frequency, The sampling rate and total run time should be initially chosen powers of two, as TROM makes use of Fast Fourier transforms. An initial guess for the frequency can also be obtained from the harmonic lattice dynamics calculations for LiF, which is around the maximum of 17THz.

Depending on the system specifics, the MD trajectory is initially correlated, and the appropriate dump interval depends on how much data is required. If the interval is too large, the slower phonon modes will not be captured; if it is too small, the trajectory will remain correlated, leading to unresolved phonon

modes. The formula used to predict what dump intervals are given by:

$$\omega = \frac{0.5}{dump\ interval \times \Delta t} \tag{4.6}$$

Where ω is the frequency range, Δt is the timestep. his formula is an estimation of the interval range, and often, setting larger dump intervals is advised since you can sample different MD trajectories, and you can also study low and high frequencies according to the phonon DOS.

For example, take the DOS of LiF in Figure 4.10 to sample high frequency modes based DFPT phonon DOS, the main phonon modes are 7.94THz as given by DOS. So, using a timestep of 0.5fs and the formula given should mean a sampling rate of around 125 MD steps should be sufficient to sample the majority of the lower frequency phonon modes.

Further sampling is required to capture enough of the higher frequencies modes, for example the maximum phonon frequency is 17THz. The period is given by $T = 1/f \approx 59$ fs, representing the shortest oscillation timescale relevant. According to the Nyquist sampling theorem, this requires a sampling interval of least two points and hence is needed $\Delta t \leq T/2$ .The longest oscillation period in LiF is 29fs. Sampling every 12 fs provides too few points per oscillation. Therefore, we combine trajectories sampled at 12 fs and every 5 steps (2.5fs, for a 0.5fs time step). This combined approach ensures adequate resolution across both low- and high-frequency modes.

This has a very direct implication on how the MD is done; clearly, to get such an MD trajectory with supercell size would be very expensive and impractical with AIMD calculations, despite the advancement of ML-MD acceleration. For a LAMMPS run, this would also require a large cluster with a sufficient IO space and computational resources.

As with Figure 4.11, the initial structure resides at equilibrium, which are high-symmetry sites in the crystal with the lowest energy configuration. Thus, atomic displacements increase the total energy. Within MD, we want to produce similar lattice dynamics displacements from equilibrium. A simple way of confirming that the MD dynamics are sufficiently equilibrated is to plot temperature and energy vs time plots. Both the dynamics for the NVT and NVE runs are well conserved, and our timesteps were well chosen to produce such well-conserved MD dynamics.

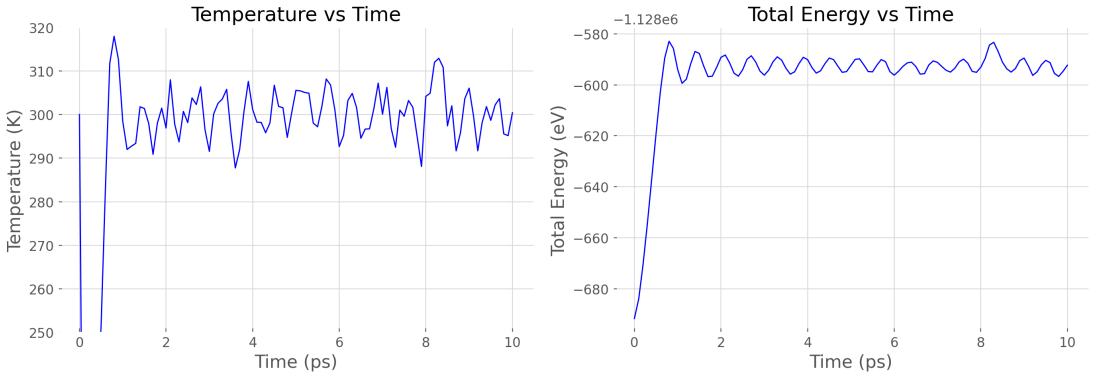

Figure 4.14: LAMMPS MD run for LiF, showing temperature vs time, and total energy vs time using NVT and NVE ensembles, respectively.

The Fourier transform of the velocity autocorrelation function (VACF) yields the phonon density of states (PDOS), making it straightforward to visualize the range of vibrational frequencies expected for LiF, as shown 4.15

$$g(\omega) = \int e^{i\omega t} \frac{\langle v(t)v(0)\rangle}{\langle v(0)v(0)\rangle} dt. \tag{4.7}$$

The supercell size, as with any MD simulation, will have a finite size effect. Since TROM in its current form does not include self-mapping to primitive and conventional cells, it means a typical suitable size of supercell is typically 5x5x5 or larger to get sufficient resolution of the peaks.

The MD phonon dispersion for LiF has three distinct $q$branches at Γ, which correspond to three TA, TO and LA modes. The higher frequency optical modes are most challenging to resolve due to the lack of a non-analytical correction term to the FCM, which usually shifts the optical modes up in frequency.

The result is that the optical $q$branches don't align with the DFT phonon dispersion, and sampling the optical modes at that frequency according to DFT is slightly shifted. The quality of the GAP potential may cause shifts in the phonon dispersion. In particular, the long-range Coulombic effects play a significant role in the optical q branch frequency due to several discontinuities and flatter dispersion lines.

The Kong method is based on statistical sampling of MD trajectories. The choice of using the primitive cell of LiF has practical implications for calculations of lattice vibrational and transport properties via MD, because they have the lowest computational cost. Since each atom contributes three degrees of freedom, a system with N atoms has a total of 3N vibrational degrees of freedom. Using a conventional cell instead of a primitive cell effectively increases the number of atoms, and therefore the degrees of freedom and hence the cost of convergence

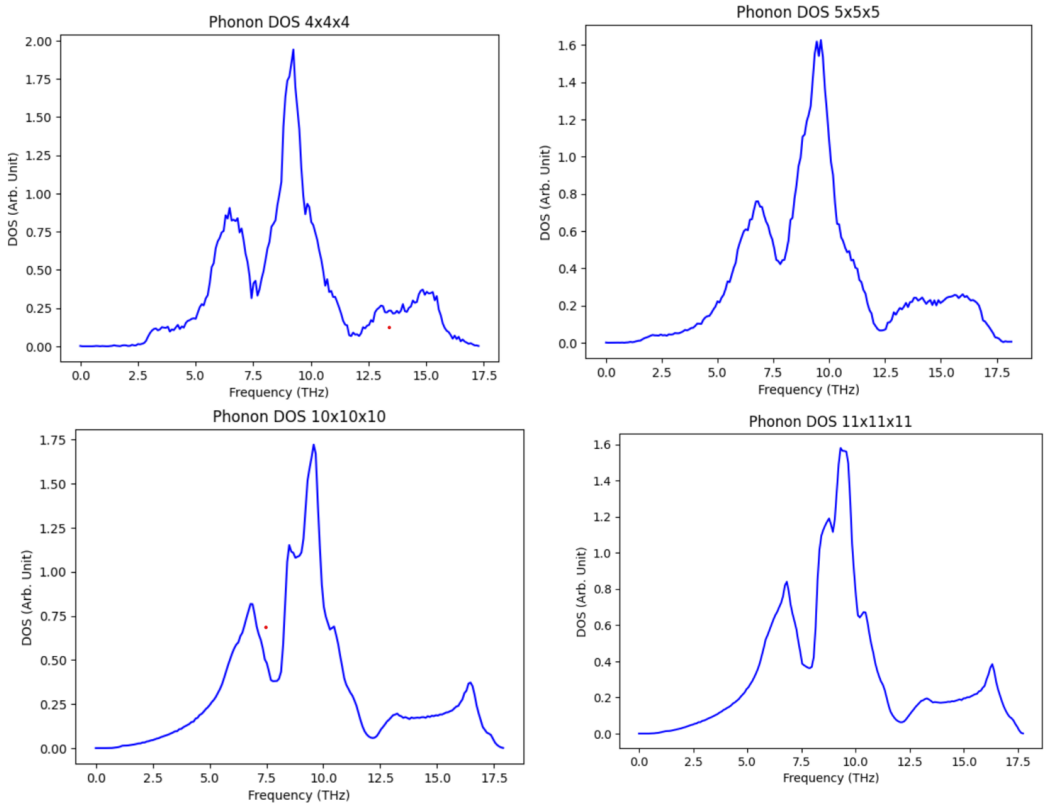

Figure 4.15: LiF phonon DOS varying supercell from auto-velocity correlation function

of FCM.

However, this means using larger supercells of the primitive cells of LiF over the conventional cells would need to converge with many fewer MD time steps and improve overall convergence of the FCM.

The larger supercells tend to require less long trajectory sampling due to large sampling of configurations in phase space, whereas smaller supercell requires much longer trajectories to get phonons out. This is primarily due to the primitive cell's lack of extra degrees of freedom, which is the current limitation of TROM, as there is no mapping between the conventional and the primitive.

The phonon modes are contained within a wave packet to build a suitable description of the phonon wave packet. It must be densely sampled from the MD trajectory to find the phonon modes to produce high-quality phonons. This trade-off between phonon q-point resolution and MD finite-size effects makes such systems particularly challenging for the training of machine-learned interatomic potentials.

Increasing the supercell also increases the resolution of the phonon dispersion. In particular, more details of what may be going on at Γ are shown for the largest supercells. The wavelength is equal to $\lambda = \frac{2\pi}{q}$ when $q = (0,0,0)$ at Γ.

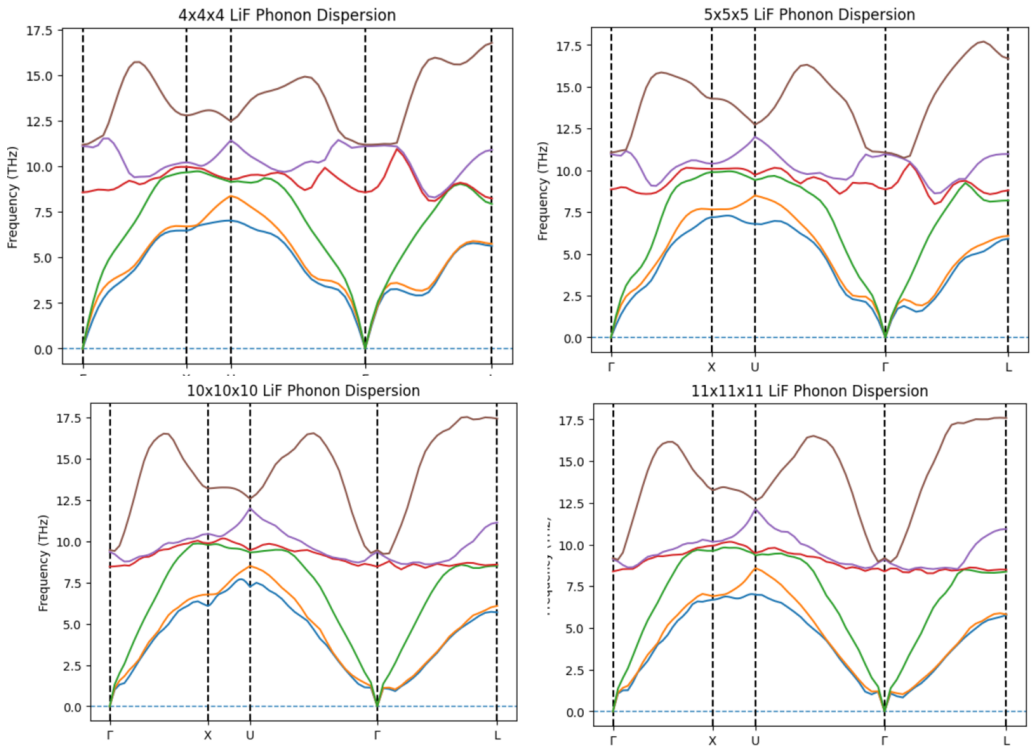

Figure 4.16: Phonon dispersions of LiF varying supercells.

You are essentially trying to capture infinity as $q \to 0$ in the long wave limit. Interpolation to $q = 0$ leads to a slight discontinuity in the $q$branch at finite q, which is a clear indication that supercells are too small to resolve such large wavelengths from the acoustic modes at the long wavelength limit, and hence struggle to resolve long wavelengths of λ and small q, as seen in figure 4.16

It is useful to study the effects of finite temperature on Phonons. In particular, anharmonicity becomes more prominent. At temperatures exceeding 600 K, there is a significant vibrational coupling between the TO and TA modes driven by anharmonic effects. We therefore expect reduced phonon lifetime because the phonon scattering mean free path is shorter.

The phonon dispersion broadening becomes more prominent as the temperature increases from 0 K to 600 K, particularly in the TA, TO, and LO phonon modes, as seen also by the phonon DOS at finite temperature. In particular, the softening of the TO mode (brown line) 4.17 intersects with the LO mode (purple line) only at 300 K. This is primarily because the GAP potential was not trained beyond the finite temperature range of 300–400 K, below it and stress testing shows that it cannot be used reliably outside the temperature range for which it was trained as shown in the phonon dispersion.

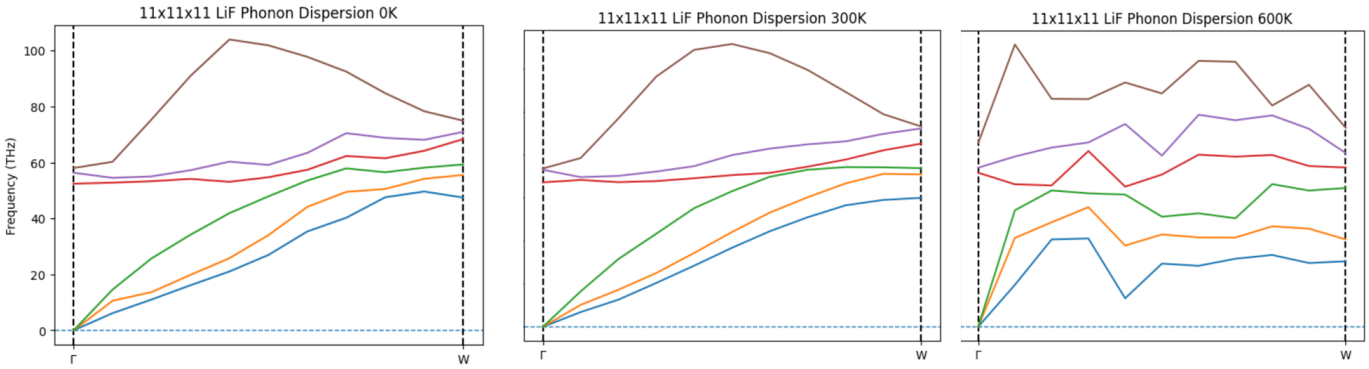

Figure 4.17: Phonon dispersions with different temperatures.

4.7 Phonon Lifetime of LiF via from Spectral Energy Density Method

At finite T , the phonon lifetime for LiF is extremely short; it's only when you reach high T that the phonon lifetimes are longer. This is because at high T, the solid LiF becomes molten, where Li has high conductivity, allowing phonon-phonon scattering to have longer lifetimes.

The lifetime can be fitted either by Gaussians or Lorentzian. Broadly speaking, these are to account for broadening mechanisms we don't include, e.g. lifetimes, instrumentation details (for comparing with experiment), thermal effects, etc. Gaussian broadening is for inhomogeneous processes, Lorentzian broadening is for homogeneous processes and is the choice for fitting the lifetime.

The range of data selected when fitting the Lorentzian functions should be large enough for the Lorentzian functions to decrease significantly from their value at half-width at half-maximum, where the line width is specified, but not too large as to pick up noise. The error in predicting the lifetime is obtained by varying the range of data used to fit the Lorentzian function.

The spectral energy density is calculated, and the peaks are fitted to a Lorentzian to extract the lifetime. Here, the SED is expected to give 6 peaks for each $q$point. At the Γ point, three acoustic phonons disappear because they have zero frequency, and three optical phonons are degenerate. This degeneracy is exactly what makes the application of this method time-consuming. The Spectral Energy Density is fitted with a Lorentzian-based function.

Here, the SED was computed for 3N modes up to a maximum sampling frequency of 50 THz (sampled every 100 steps over a 3-million-step trajectory at 0.5 fs). Since the maximum physical frequency for LiF at $T = 0$ does not exceed peaks above 30THz, the increased shift upwards in frequency is attributed to

significant numerical noise.

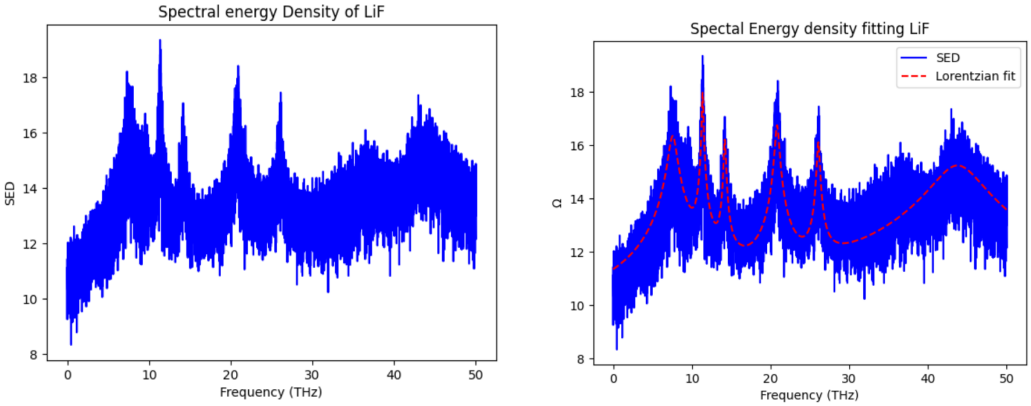

(a) SED of LiF (b) SED fitted with Lorentzian

Figure 4.18: SED and fitted SED of LiF showing 5 mode peaks.

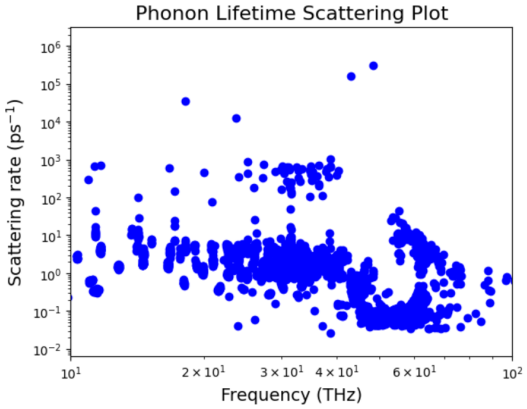

Figure 4.19: Phonon scattering modes of LiF through SED method.

The implication of this on the phonon lifetime is that, because of the numerical noise we have introduced fictitious phonon-phonon scattering, due to such a broad peak, the Lorentzian function cannot measure the half-maximum, which is why there are outliers in Figure 4.20 at 40-45THZ.The benefit of the SED is that, in principle, as it does not rely on the eigenvectors of the phonon modes, the missing interactions from the lack of LO/TO splitting means phonon lifetimes would have several missing scattering points; however, towards 6THz we begin to see some of the LO/TO scattering phonon modes starting to appear. Overfitting of the peaks is evident for this much numerical noise and longer lifetimes.

4.8 LiF Phonons from Symmetrization FCM Method

The GAP model may neglect to capture LO/TO splitting, but there are still short-range effects that are captured. It is therefore far easier to add non-analytic

corrections to DFT data than it is for the GAP/LAMMPS runs, which require extra work to correctly get the long-range effects right.

The Kong method makes any AIMD-based calculations intractable, even for accelerated hybrid-MD to get phonons out. Based on this different approach, we can create a best fit to FCM and extract higher-order terms. The phonon dispersions are sampled directly from CASTEP AIMD calculations, which makes it viable with the optional benefit of using MD acceleration to make it even quicker.

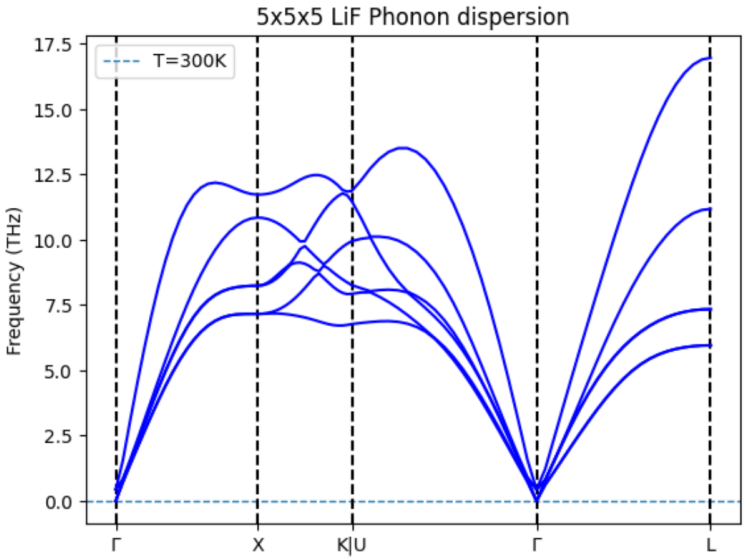

Figure 4.20: AIMD calculated phonon dispersion.

For example, 4.20 shows the phonon dispersion from LAMMPS run where here is a Hybrid-MD accelerated with 30ps of data of LiF running with NVT at 0.1fs with PBE functional with a 5x5x5 supercell at 300K Although here we have not added any LO/TO splitting corrections to phonon dispersion, and the optical modes are not as well sampled, we can see that we do have 6 dispersion bands for the LiF 2 atom primitive cell.

With analytical corrections and longer sampled runs with Hybrid-MD should get something more in tune with what we expect LiF phonon dispersion to look like. However, we have to appreciate that going from not getting anything of this supercell size and trajectory length to this shows that this method using AIMD data is advantageous.

We therefore choose a 12x12x12 supercell with a longer trajectory of 1 million time steps. For comparison, the Kong method requires anywhere from 2-3 million timesteps. Both NVE and NVT were used with 0.1fs. The same GAP potential developed for a 5x5x5 supercell in AIMD calculations was applied.

Interestingly, the symmetrisation of the phonon dispersion now has very dis-

tinct, separated optical phonon branches, with the expectation that the highest frequency mode is around 15 THz.

The GAP potential has been shown to reasonably predict the phonon dispersion trained on different supercell sizes, although the optical phonon modes are wrong because of LO/TO interactions being absent, the FCM fitting is a reasonable approximation to the actual LiF phonon dispersion. Likewise, we can use the LAMMPS trajectory in the same way by evaluating the model with the GAP potential derived from the Hybrid-MD run shown in Figure 4.21. LAMMPS scales better with larger supercells, and we can do more timesteps without the computational cost associated with AIMD or Hybrid-MD methods. Here, the symmetrisation of FCM with a different GAP potential shows some stability was achieved at 600K. The fitted FCM method works well even when the GAP potential was not trained beyond the finite temperature range because it relies on a small sample of configurations and fitting FCM according to least squares method. In this case the two methods give very different outcomes.

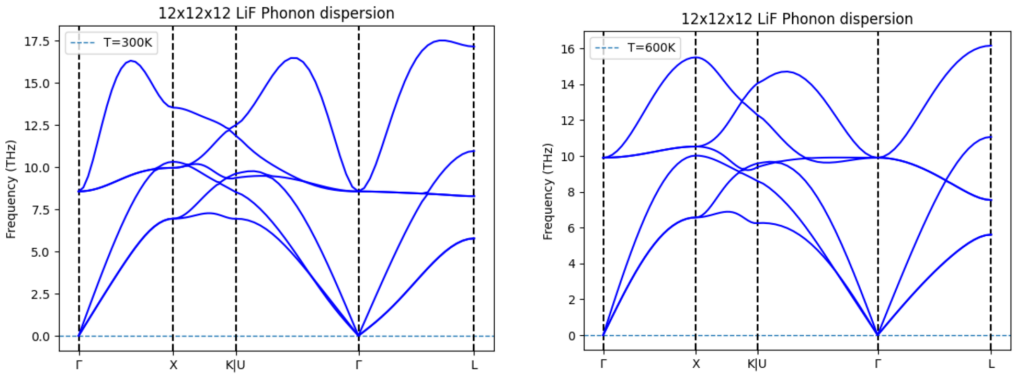

Finite-temperature phonon dispersions for LiF calculated at (a) 300 K and (b) 600 K. The two panels illustrate the temperature-dependent shifts in the phonon frequencies, highlighting the anharmonic softening of the modes as the temperature increases.

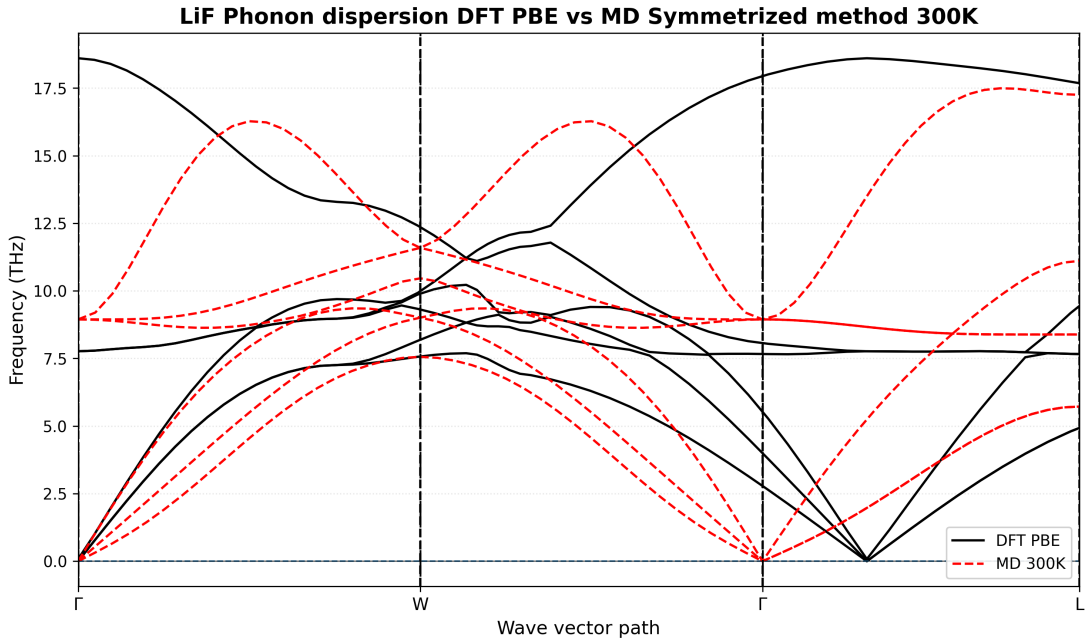

Figure 4.21: Phonon dispersion relations for LiF. The solid black lines represent the harmonic phonon frequencies calculated using $T = 0$ DFPT with the PBE functional, while the dashed red lines show the finite-temperature (300 K) GAP MLIP dispersion obtained using the MD symmetrized method.

4.8.1 Phonon Lifetime LiF via mode decomposition from symmetrised FCM

In section 4.5, we showed that LiF has a relatively small anharmonic force, which causes the phonon dispersion to shift and broaden, so that the normal-mode amplitudes q are no longer periodic in time, i.e there is a lifetime and hence a decay in total energy. If the anharmonic interaction is small, so that the lifetime of the normal-mode amplitudes can be written in perturbed form:

$$Q(t) = Q e^{-i(\omega+\Delta-i\Gamma)t} \tag{4.8}$$

where Δ is the energy shift and Γ is the broadening term. This describes an anharmonic phonon mode coordinate which has a shifted frequency and damping exponential which represent the lifetime of the anharmonic phonon mode. This is exactly the mode decomposition we have defined in sections 2.8.1 and 2.8. The scattering rates of LiF are shown for both LAMMPS and AIMD calculations. The LAMMPS scattering has a maximum frequency spectrum sample of 10THz. The choice of mode decomposition over the SED method for extracting the phonon lifetimes is that fitting the peaks can be problematic, as this is also prone to numerical background noise, selecting how to fit these peaks and how to remove numerical noise without affecting the spectral signal too much. The AIMD calculations' scattering plots have only sampled the first part of the

LAMMPS lifetimes. This is primarily due to not having a long enough trajectory to sufficiently sample the lower frequency modes, and therefore, the lifetime is missing several phonon-phonon scattering mechanisms.

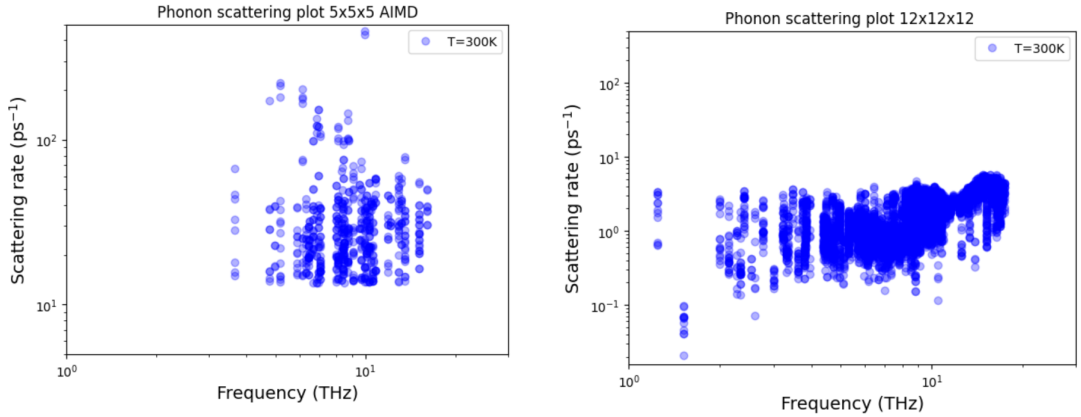

(a) AIMD lifetime scattering plot (b) LAMMPS/GAP lifetime scatterings

Figure 4.22: Lifetime scattering plots for two different approaches, AIMD and LAMMPS/GAP.

Sampling of longer trajectory runs with a mix of high and low frequency modes is therefore needed for both methods to fully sample the set of frequencies of LiF, which are evidently missing key scattering mechanisms.

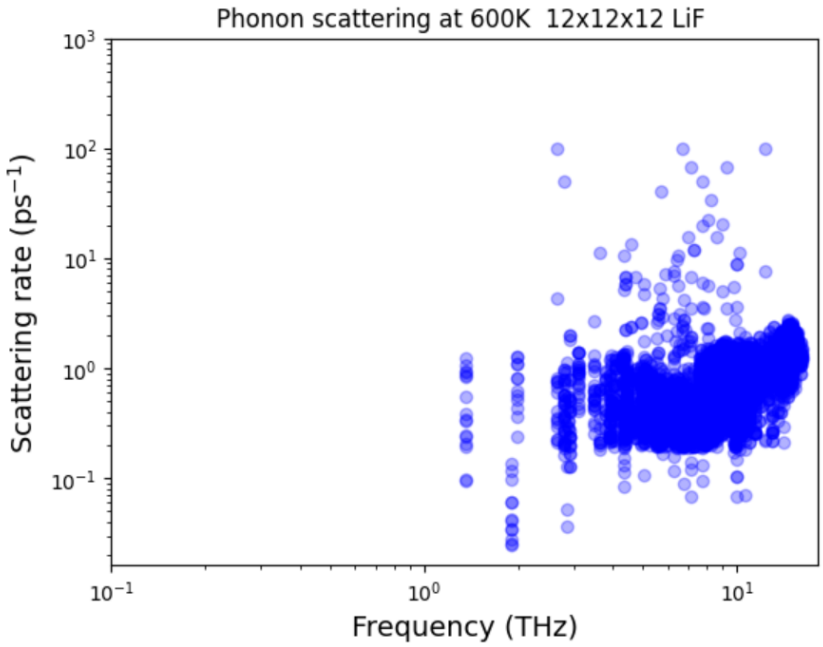

Figure 4.23: Phonon scattering lifetime at 600K.

The lifetime for LiF is very short so at 300K most of the scattering is localized where these are mainly a mixture of LA and TA phonon modes. They correspond to low frequency phonon modes as a result of not adding smaller MD sampling steps.

Although we can see more vivid image of the phonon lifetime decay, there are no higher frequency modes present that would indicate strong coupling between the phonon modes. As seen in the phonon dispersion, the bands become more disperse as a consequence of the anharmonicity causing strong phonon-phonon coupling as a function of temperature.

The mode decomposition as preferred method to study the lifetime at higher T through Kong method can become expensive for larger systems greater than 10,00 atoms as this a very costly FCM solver and Kong method will often lead to simply running out of memory for python based code. The fitted force constant matrix has a cutoff for amount of sampling it needs which is based on Monte Carlo sampling number of configurations and decides the cutoff for FCM fit. It means it will always require less data than with the Kong method making it better choice for the mode decomposition method.

4.9 Comparison to known phonon lifetimes for LiF

Both the Spectral Energy Density and the time domain total normal mode energy methods have proven to be effective ways of theoretically calculating the lifetime, such as those of silicon. LiF has proven to be quite a hard case study due to its electrostatics. LiF was also investigated by Liang [1]. This method is a good benchmark to test out LiF MD lifetime against. Since most of the literature for thermal conductivity is calculated via Boltzmann transport equations, as with the Liang paper, by computing third-order force constants with supercell perturbations.

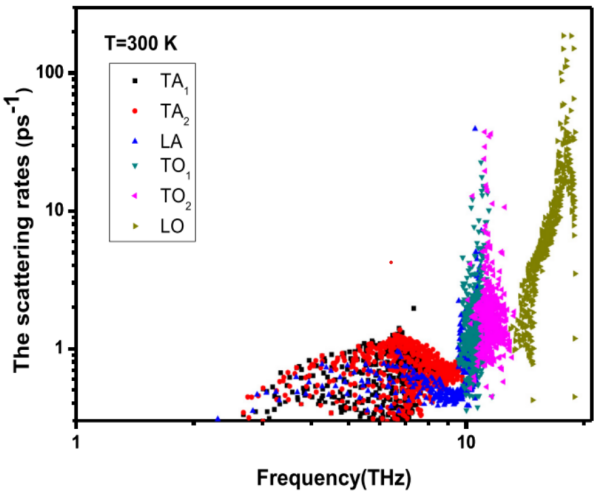

Figure 4.24: Phonon scattering lifetime of LiF taken from Liang [1].

The scatter plot of lifetimes of both methods has shown to sample mainly the

tail end of TA and LA phonon at 10THz (blue dots). The LO and TO scattering phonon mode interactions are missing in our data because long-range forces are not included in the GAP potential of LiF. Because LO/TO interaction is a key scattering mechanism, and they are not showing where we would expect them to be. Both the mode decompositions and SED methods have suffered from this. Although we have shown that AIMD data could get the phonon dispersion out, longer trajectories are needed for the lifetime which can be expensive for AIMD. Irrespective of this both methods scale differently, irrespective of how you create your data or the size of the data being trained or run. For example, the computational time required to perform normal mode decomposition depends on the number of atoms N_n in the system and the number of atoms in the primitive cell N. For the eigenvalue problem associated with Harmonic lattice dynamics, the total memory required scales with $\mathcal{O}(N^2)$ with 3N eigenvectors. This becomes poor scaling, in the limit of very large systems above 10,000 atoms. TROM is written in Python, and when using the numpy module, mapping atomic positions and velocity to kinetic and potential normal mode coordinates, can decrease the computational workload. The Hellman method for getting the FCM is based on sampling of the MD trajectory. This is useful because we don't need as much data as previously, which means the best-fitted FCM can be used with far less data to get the phonon lifetimes.

Likewise, the computational cost of SED is less than mode decomposition by a factor of 3 for bulk crystal structures. The SED requires longer trajectory runs, roughly the longest estimated lifetime should have an order of magnitude larger to try and resolve the peaks. At higher T it becomes challenging , when the phonon line-widths broaden and become comparable to the spacing between mode frequencies. The downside to the SED is the background noise, which is extremely hard to remove; fitting the peaks with multiple peaks individually is usually used to try and reduce this; however, this requires reconstruction of the Lorentzian functions which can be costly. Usually, construction happens with multiple peaks being fitted by a single function. The cost of fitting can be reduced by fitting the peaks from all allowed phonon modes in the system simultaneously, but the error and noise of the fitting and future adjustments to code will be needed to improve the background noise, as this is currently leading to overestimation of the lifetime.

LAMMPS scales with $\mathcal{O}(N_n)$ linearly with supercell size; however, the DFT PES is a complex function to fit. GAP requires high-quality data, since our method relies on a very large cut-off radius with increasing supercell to properly evaluate the long-range coulombic effects. A key limitation to using GAP is that it is very expensive for both training the GAP model and for LAMMPS

to evaluate the pair potential. If the system has many electrons or is well known to suffer from electrostatics, evaluating such systems through MLIP is a time-consuming process in itself.

The proposed methods to extract the lifetime from MD-based methods arguably could be more expensive than BTE-based methods when considering the training MLIP and data required to get the lifetime out. The workflow is reduced and made far simpler for comparative study. Fixing the long-range electrostatics in MLIPs would be a long-term fix to reduce the supercell and MD trajectories; for example, adding long-range forces in hybrid-MD with GAP could be a very useful feature in finding missing key scattering mechanisms. With the added symmetrisation of FCM, the calculations should therefore be far less computationally intensive to generate such large data sets.

Chapter 5

Conclusions and Future Work

5.1 Conclusions

The testing and development of phonon lifetimes have highlighted a few drawbacks to the initial ideas we had at the start. Although the Hybrid-MD package provides accelerated MD in its current form, it's very challenging to get it working. It means the project has GAP potentials that have been trained on a few hundred atoms rather than few thousand that is necessary for bigger LAMMPS supercell calculations that was needed to get phonons out. The GAP potential from hybrid-MD is suitable for testing, but a better potential must be developed. With the new GAP interface which is all within CASTEP v26 I am sure this would be effective for larger supercells.

The Kong method has been shown to sample long-wavelength phonons, but it requires a large amount of data to even extract any information about the phonons. Since the new developments of adding symmetry, it has been shown that the need for such long trajectories can be reduced and actually speed up the workflow. Since it is possible with the Symmetrization Method to achieve a fully finite temperature phonon dispersion from just a few thousand MD configurations which is far quicker than Kong Method when TROM is used

The lack of long-range electrostatics of LiF has proved to be a real challenge for the on-the -fly GAP training since it could never reach at higher temperature the required force and energy tolerances needed to get dynamical stable phonons out from MD. Both the Kong method and the symmetrisation of FCM need non-analytical corrections, as long-range electrostatics are clearly missing from the GAP models we produced, which are current limitations. Current MLIP have to developed in such a way that all long range electrostatics must be removed fully from the training set to create a baseline model that only captures short range effects. This can further be used with external long-range electrostatic

solvers to get the desired long range electrostatics properly. Recent developments of MLIPs, in particular based upon MACE, have developed long range electrostatics with Ewald solvers [36]. Algorithmic advancements in this area have streamlined the workflow, making it significantly more straightforward for users to train models that incorporate long-range electrostatics.

Overall, we can get a finite temperature physics in phonon dispersions, and we can see how the anharmonicity can be quantified and included in phonon dispersions. Although we can get the lifetime, it has been hard to get all the right scattering mechanisms for where we would expect them to be.

5.2 Future Work

Investigating alternative approaches to the thermal conductivity and lifetime should continue in the following areas. First is the test for a range of new MLIP, for example, MACE potentials have been considered for some time as the successor of GAP. It is yet unclear whether a computationally less expensive potential to evaluate such as SW or LJP could be used as an alternative potential to benchmark these methods on getting phonons out, which would be useful as a comparison against more advanced GAP and MACE MLIPs.

In this work, LiF proved to be far more challenging to simulate. Due to long-range electrostatic interactions and absence of any non-analytical term for LO/TO splitting, getting MD phonons of LiF took the majority of the research time. Hence it was decided that phonons from MD for PbTe was left out , considering the timescale for the project. Complex examples such as SnS $SrTiO_3$ which could be more challenging examples possessing dynamically unstable phases and particular unstable anharmonic frequency modes, would provide greater testing of TROM. Since recent developments based on TDEP [37] and FCM symmetry can be used to predict phonon dispersion to higher-order terms, this could be an interesting avenue to look at more closely for a method to extract the lifetime more accurately, without the need for the Kong method.

Since we have the lifetime, further investigation of the thermal conductivity values compared with BTE-based theories would be most essential in understanding how this method could be advantageous over other theoretical frameworks.

Another interesting area would be looking at electron-phonon coupling and how the anharmonicity is based on the measure from MD, and to measure the effect this has on anharmonicity based on most anharmonic structures on electron-phonon coupling.

Appendix A

A.1 Notebooks

The notebooks for the TROM analysis, along with the LAMMPS input files and output data https://github.com/max88lau/CASTEP_utilties are in GitHub Repository.

A.2 Snippets of the anharmonicity measure

```
import numpy as np
import matplotlib.pyplot as plt


def read_md_displacements(filename):
    """Read atomic displacements per time step."""
    displacements_per_timestep = []
    current_displacement = []

    with open(filename, 'r') as f:
        for line in f:
            line = line.strip()
            if line.startswith("Time step"):
                if current_displacement:
                    displacements_per_timestep.append(np.array(
    current_displacement).flatten())
                    current_displacement = []
            elif "Delta_R =" in line:
                parts = line.split("Delta_R =")[-1].strip().split()
                disp = [float(x) for x in parts]
                current_displacement.append(disp)

    if current_displacement:
        displacements_per_timestep.append(np.array(
    current_displacement).flatten())
```

```
24
25      return displacements_per_timestep
26
27
28  def read_forces_by_timestep(filename):
29      """Parse forces from structured force file per time step."""
30      forces = []
31      with open(filename, 'r') as f:
32          current = []
33          for line in f:
34              line = line.strip()
35              if line.startswith("Time step"):
36                  if current:
37                      forces.append(np.array(current).flatten())
38                      current = []
39              elif "Force =" in line:
40                  values = line.split("Force =")[-1].strip().split()
41                  current.append([float(v) for v in values])
42          if current:
43              forces.append(np.array(current).flatten())
44      return forces
45
46
47  def read_force_constant_matrix(filename, num_atoms=64):
48      """Read the full 3N x 3N force constant matrix from .phonon-
        style file."""
49      dim = 3 * num_atoms
50      D = np.zeros((dim, dim))
51
52      with open(filename, 'r') as f:
53          lines = f.readlines()
54
55      row_counter = 0
56      for line in lines:
57          if "Supercell" in line or "Force Constant" in line or "%" in
        line or not line.strip():
58              continue
59
60          parts = line.strip().split()
61          if len(parts) < 8 or not parts[0].isdigit():
62              continue
63
64          i_atom = int(parts[0]) - 1
65          i_dir = int(parts[1]) - 1
66          row_idx = 3 * i_atom + i_dir
67
68          # Parse 6 numbers after first 2 entries (6 per line)
69          values = list(map(float, parts[2:8]))
```

```
        col_base = (row_counter % dim) // 3 * 3

        D[row_idx, col_base:col_base+6] = values

        # When 3 components per row are collected, move to next set
        if row_idx % 3 == 2:
            row_counter += 6  # move 6 cols forward every 3 rows

    return D


def compute_forces(D, U):
    return -np.dot(D, U)


# === MAIN ===
phonon_file = "LiF.castep"
displacements_file = "displacements_output.txt"
forces_file = "LiF_2_forces.txt"

# Read input data
D = read_force_constant_matrix(phonon_file)
U_list = read_md_displacements(displacements_file)
DFT_force_blocks = read_forces_by_timestep(forces_file)

if len(U_list) != len(DFT_force_blocks):
    raise ValueError(f"Mismatch: {len(U_list)} displacements vs {len(DFT_force_blocks)} force blocks.")

# === COMPUTATION ===
anharmonic_measures = []
Fh_all = []
FA_all = []
F_DFT = []

for i, (U, F_dft_block) in enumerate(zip(U_list, DFT_force_blocks)):
    F_dft = F_dft_block.flatten()
    F_harm = compute_forces(D, U).flatten()
    F_anharm = F_dft - F_harm

    var_anharm = np.var(F_anharm, ddof=3)
    var_harm = np.var(F_harm, ddof=3)
    measure = np.sqrt(var_anharm / var_harm) if var_harm != 0 else np.nan
    anharmonic_measures.append((1 / 6) * measure)

    Fh_all.extend(F_harm)
    FA_all.extend(F_anharm)
```

```
116     F_DFT.extend(F_dft)
117
118     if True:
119         print(f"Time step {i + 1}: Anharmonic Measure = {(1 / 6) *
    measure:.6f}")
120
121
122 # === WRITE RESULTS TO FILE ===
123 output_file = "anharmonicity_measures.txt"
124
125 with open(output_file, "w") as f:
126     f.write("# TimeStep AnharmonicityMeasure\n")
127     for idx, val in enumerate(anharmonic_measures, start=1):
128         f.write(f"{idx} {val:.6e}\n")
129
130 # === PLOT ===
131 plt.figure(figsize=(10, 6))
132
133 x_values = np.array(range(1, len(anharmonic_measures)+1)) / 100
134 plt.plot(x_values, anharmonic_measures, 'o-', markersize=3)
135 plt.xlabel("Time Step")
136 plt.ylabel("Anharmonicity")
137 plt.title("Anharmonicity vs Time Step")
138
139 # Set x-axis ticks to show only 0, 5, 10, 15, 20, 25, 30
140 plt.xticks([0, 5, 10, 15, 20, 25, 30])
141
142 plt.grid(True)
143 plt.tight_layout()
144 plt.show()
```

Listing A.1: Python script for computing anharmonic force contributions from MD trajectories

Bibliography

[1] T. Liang, W. Q. Chen, C. E. Hu, X. R. Chen, and Q. F. Chen, "Lattice dynamics and thermal conductivity of lithium fluoride via first-principles calculations," *Solid State Communications*, vol. 272, pp. 28–32, 4 2018.

[2] Y. Ekinci and J. Toennies, "Thermal expansion of the LiF(001) surface," *Surface Science*, vol. 563, no. 1, pp. 127–134, 2004.

[3] L. Lindsay, "Isotope scattering and phonon thermal conductivity in light atom compounds: LiH and LiF," *Phys. Rev. B*, vol. 94, p. 174304, Nov 2016.

[4] V. Stevanović, P. Gorai, B. Ortiz, and E. S. Toberer, "Quest for New Thermoelectric Materials," in *Computational Materials Discovery* (A. R. Oganov, G. Saleh, and A. G. Kvashnin, eds.), p. 0, The Royal Society of Chemistry, 11 2018.

[5] W. Li, J. Carrete, N. A. Katcho, and N. Mingo, "ShengBTE: A solver of the Boltzmann transport equation for phonons," *Computer Physics Communications*, vol. 185, no. 6, pp. 1747–1758, 2014.

[6] F. Müller-Plathe, "A simple nonequilibrium molecular dynamics method for calculating the thermal conductivity," *The Journal of Chemical Physics*, vol. 106, pp. 6082–6085, 04 1997.

[7] Z. Fan, L. F. C. Pereira, H.-Q. Wang, J.-C. Zheng, D. Donadio, and A. Harju, "Force and heat current formulas for many-body potentials in molecular dynamics simulations with applications to thermal conductivity calculations," *Phys. Rev. B*, vol. 92, p. 094301, Sep 2015.

[8] R. Kubo, "The fluctuation-dissipation theorem," *Reports on Progress in Physics*, vol. 29, p. 255, jan 1966.

[9] L. T. Kong, "Phonon dispersion measured directly from molecular dynamics simulations," *Computer Physics Communications*, vol. 182, no. 10, pp. 2201–2207, 2011.

[10] A. A. Maradudin and S. H. Vosko, "Symmetry properties of the normal vibrations of a crystal," *Rev. Mod. Phys.*, vol. 40, pp. 1–37, Jan 1968.

[11] M. Born and R. Oppenheimer, "Zur Quantentheorie der Molekeln," *Annalen der Physik*, vol. 389, no. 20, pp. 457–484, 1927.

[12] R. Van Leeuwen, "Density functional approach to the many-body problem: key concepts and exact functionals," tech. rep.

[13] P. Hohenberg and W. Kohn, "Inhomogeneous electron gas," *Phys. Rev.*, vol. 136, pp. B864–B871, Nov 1964.

[14] W. Kohn and L. J. Sham, "Self-consistent equations including exchange and correlation effects," *Phys. Rev.*, vol. 140, pp. A1133–A1138, Nov 1965.

[15] M. Born and K. Huang, *Dynamical Theory Of Crystal Lattices*. Oxford University Press, 08 1996.

[16] B. Wei, Q. Sun, C. Li, and J. Hong, "Phonon anharmonicity: a pertinent review of recent progress and perspective," 11 2021.

[17] L. T. Kong, "Phonon dispersion measured directly from molecular dynamics simulations," *Computer Physics Communications*, vol. 182, pp. 2201–2207, 10 2011.

[18] S. Plimpton, "Fast parallel algorithms for short-range molecular dynamics," *Journal of Computational Physics*, vol. 117, no. 1, pp. 1–19, 1995.

[19] O. Hellman, I. A. Abrikosov, and S. I. Simak, "Lattice dynamics of anharmonic solids from first principles," *Phys. Rev. B*, vol. 84, p. 180301, Nov 2011.

[20] O. Hellman and D. A. Broido, "Phonon thermal transport in Bi_2Te_3 from first principles," *Phys. Rev. B*, vol. 90, p. 134309, Oct 2014.

[21] T. Feng, B. Qiu, and X. Ruan, "Anharmonicity and necessity of phonon eigenvectors in the phonon normal mode analysis," *Journal of Applied Physics*, vol. 117, p. 195102, 05 2015.

[22] J. A. Thomas, J. E. Turney, R. M. Iutzi, C. H. Amon, and A. J. H. McGaughey, "Predicting phonon dispersion relations and lifetimes from the spectral energy density," *Phys. Rev. B*, vol. 81, p. 081411, Feb 2010.

[23] J. E. Turney, E. S. Landry, A. J. McGaughey, and C. H. Amon, "Predicting phonon properties and thermal conductivity from anharmonic lattice dynamics calculations and molecular dynamics simulations," *Physical Review B - Condensed Matter and Materials Physics*, vol. 79, 2 2009.

[24] S. Clark, M. Segall, C. Pickard, P. Hasnip, M. Probert, K. Refson, and M. Payne, "First principles methods using CASTEP," *Zeitschrift für Kristallographie*, vol. 220, 05 2005.

[25] K. Lejaeghere and S. Cottenier, "Comparing Solid State DFT Codes, Basis Sets and Potentials - Delta Codes DFT." `https://molmodstatic.ugent.be/deltacodesdft/index.html`, 2014–2019. Database for comparing solid-state DFT codes using the Δ-value metric. Contact: Kurt.Lejaeghere@UGent.be or Stefaan.Cottenier@UGent.be.

[26] S. Baroni, S. de Gironcoli, A. Dal Corso, and P. Giannozzi, "Phonons and related crystal properties from density-functional perturbation theory," *Rev. Mod. Phys.*, vol. 73, pp. 515–562, Jul 2001.

[27] V. L. Deringer, A. P. Bartók, N. Bernstein, D. M. Wilkins, M. Ceriotti, and G. Csányi, "Gaussian process regression for materials and molecules," *Chemical Reviews*, vol. 121, no. 16, pp. 10073–10141, 2021. PMID: 34398616.

[28] S. Klawohn, J. P. Darby, J. R. Kermode, G. Csányi, M. A. Caro, and A. P. Bartók, "Gaussian approximation potentials: Theory, software implementation and application examples," *The Journal of Chemical Physics*, vol. 159, p. 174108, 11 2023.

[29] P. Rowe, G. Csányi, D. Alfé, and A. Michaelides, "Development of a machine learning potential for graphene," *Physical Review B*, vol. 97, p. 054303, 2017.

[30] "Gap — gaussian approximation potentials documentation." `https://libatoms.github.io/GAP/index.html`, 2025. Accessed: 2025-11-29.

[31] S. Yue, M. C. Muniz, M. F. Calegari Andrade, L. Zhang, R. Car, and A. Z. Panagiotopoulos, "When do short-range atomistic machine-learning models fall short?," *The Journal of Chemical Physics*, vol. 154, p. 034111, 01 2021.

[32] S. De, A. P. Bartók, G. Csányi, and M. Ceriotti, "Comparing molecules and solids across structural and alchemical space," *Physical Chemistry Chemical Physics*, vol. 18, pp. 13754–13769, 05 2016.

[33] T. K. Stenczel, Z. El-Machachi, G. Liepuoniute, J. D. Morrow, A. P. Bartók, M. I. J. Probert, G. Csányi, and V. L. Deringer, "Machine-learned acceleration for molecular dynamics in CASTEP," *The Journal of Chemical Physics*, vol. 159, p. 044803, 07 2023.

[34] P. T. Jochym, J. Łażewski, and W. Szuszkiewicz, "Phonon mode potential and its contribution to anharmonism," *Scientific Reports*, vol. 10, 12 2020.

[35] D. Marx and J. Hutter, *Ab Initio Molecular Dynamics: Basic Theory and Advanced Methods*. Cambridge University Press, 2009.

[36] B. Cheng, "Latent Ewald summation for machine learning of long-range interactions," 12 2024.

[37] F. Knoop, N. Shulumba, A. Castellano, J. P. A. Batista, R. Farris, M. J. Verstraete, M. Heine, D. Broido, D. S. Kim, J. Klarbring, I. A. Abrikosov, S. I. Simak, and O. Hellman, "TDEP: Temperature Dependent Effective Potentials," *Journal of Open Source Software*, vol. 9, p. 6150, 2 2024.